

Quantum Theory of Electronic and Thermal Transport through Nanostructures

Renad Khalil Almughathawi

Ph.D. Thesis in Physics

This thesis is submitted for the degree of
Doctor of Philosophy
2022

Declaration

Except where stated otherwise, I hereby declare that this thesis is a result of the author's original work and has not been submitted in whole or in part for the award of a higher degree elsewhere.

This thesis documents work carried out between October 2018 and January 2022 at Lancaster University, UK, under the supervision of Prof. Colin J. Lambert and Dr. Qingqing Wu and funded by Ministry of Higher Education and Taibah University Scholarship, Saudi Arabia.

Renad Almughathawi

January 2022

Dedication

This work is dedicated to my beloved mom and dad,

Khalil Almughathawi and Rahmah Alraddadi

for their love, endless support, encouragement and sacrifices.

Abstract

It is essential for nano- and molecular-scale applications to explore and understand the electron and phonon transport characteristics of molecular junctions consisting of a scattering region such as a molecule connected to metallic electrodes. This thesis presents a series of studies into the electronic and thermoelectric properties of molecular junctions using theoretical methods described in chapters 2 and 3. Chapter 2 presents an introduction to the density functional theory (DFT). It is followed by an outline of transport theory in chapter 3, based on a Green's function formalism.

Recent studies of molecular thermoelectrics help to understand how atomic-scale structural modifications in junctions can affect the thermopower of molecular devices. This is illustrated in chapter 4, where I investigate the connectivity dependence on the thermoelectric properties of a series of thiophenediketopyrrolopyrrole (DPP) derivative molecules. For example, I find that molecules with connectivities leading to destructive quantum interference (DQI) show significant conductance variations upon ring rotation. This DQI also leads to enhanced Seebeck coefficients, which can reach 500–700 $\mu\text{V}/\text{K}$. For the molecule with constructive quantum interference (CQI), I find that after including the contribution to the thermal conductance from phonons, the full figure of merit (ZT) for the CQI molecules could reach 1.5 at room temperature.

Based on the DPP molecules, Chapter 5 presents a collaborative study with experimentalists at Xiamen University, China, of the effect of branching alkyl chains (isopentane, 3-methylheptane, and 9-methylnonadecane) on the geometrical changes such as pi-stacked

distances and backbone dihedral angles. It is demonstrated that as the alkyl chain becomes longer the electrical conductance decreases due to an increase in the torsional angles between the aromatic rings. The relationship between the conductance and the torsion angle θ follows approximately $T(E, \theta) \propto \cos^6 \theta$. This indicates that the insulating side chain could be used to control single-molecule conductance, which is of significance for the design of future organic devices.

Acknowledgements

I would like to express my sincere and heartfelt thanks, and acknowledge my deep sense of gratitude to Professor Colin J. Lambert, who encouraged me to do my utmost, and gave me invaluable help based on his incomparable expertise. More especially, he provided me the opportunity to prepare the projects with individual conversations, thoughtful suggestions, and insight. His kindness, patience and support are prodigious to guide me during my study with an inclusive and encouraging heart. His tutorials provide me a deep understanding of molecular electronics which would be really helpful for my future study and research, I am truly grateful.

Also, I am obliged to Dr. Qingqing Wu for her continued support, encouragement, and valuable guidance and enjoyable discussion we had throughout my Ph.D. I have been extremely lucky to have a co-supervisor who cared so much about my work, and who responded to my questions and queries so promptly.

I would also like to express my grateful admiration to Dr. Iain Grace for helping me to use SIESTA DFT code, and continues support through my study. Also, many thanks to Dr. Songjun Hou whose support and encouragement has been invaluable throughout my projects.

In addition, I would like to thank all the co-supervisors in our group Dr. Sara Sangtarash, Dr. Ali Ismael, and Dr. Michel Jay for providing help and adding positive impact during my Ph.D. journey and I would like to thank all my friends and colleagues in Colin's group. I should also

appreciate the collaborating experiments from Prof. Wenjing Hong's group in Xiamen University.

My greetings thanks to the support I received during my PhD from the ministry of higher education in Saudi Arabia and Taibah University for this great opportunity to study a Ph.D. at Lancaster University, United Kingdom.

Finally, I owe thanks to my beloved parents who support me all the way to pursue my dream. The sacrifices you have made for me are beyond any description, Thank you mom and dad for everything! My gratitude to my family for all of the love, support, encouragement, and prayers they have sent my way along this journey.

List of publications

During my PhD studies I published the following journal articles:

- [1]. R. Almughathawi, S. Hou, Q. Wu, Z. Liu, W. Hong, and C. Lambert, “Conformation and Quantum-Interference-Enhanced Thermoelectric Properties of Diphenyl Diketopyrrolopyrrole Derivatives,” *ACS Sensors*, vol. 6, no. 2, pp. 470–476, 2021.
- [2]. W. Jiang *et al.*, “Single-Molecule Charge Transport Modulation Induced by Steric Effects of Side Alkyl Chains,” *ChemPhysChem*, 2021.

Contents

1. Introduction to molecular-scale electronics	1
1.1. Molecular electronics	1
1.2. Molecular Junctions	4
1.3. Quantum interference	6
1.4. Thesis Outline	7
Bibliography:	8
2. Density Functional Theory	14
2.1. Introduction	14
2.2. The Schrödinger Equation	15
2.3. Born-Oppenheimer approximation:	16
2.4. Hohenberg-Kohn theorem approximation:	17
2.5. The Kohn-Sham Approach	18
2.5.1. Exchange and correlation functional	20
2.5.1.1. Local Density Approximation (LDA)	21
2.5.1.2. Generalized Gradient Approximation (GGA)	22
2.6. SIESTA	22
2.6.1. The Pseudopotential Approximation	23
2.6.2. Calculating binding energies using the counterpoise method (CP)	24
2.7. Calculations in Practice	25
Bibliography:	28
3. Transport theory	31
3.1. Introduction:	31
3.2. The Landauer formula	32

3.3. Scattering matrix	35
3.4. Green's Function	39
3.4.1. Green's function of a doubly infinite chain	39
3.4.2. Green's function of a semi-infinite one-dimensional chain	41
3.4.3. One-dimensional scattering system	43
3.4.4. Transport through an arbitrary scattering region	45
3.5. The transmission curve features	51
3.5.1. Breit-Wigner resonance	51
3.5.2. Anti-resonances	54
3.5.3. Fano resonance	55
3.6. Magic Number theory	57
3.7. Green function and frontier molecular orbitals	61
3.8. Thermoelectricity	62
3.8.1. The sign of Seebeck coefficient (S)	63
3.8.2. Expressions for thermoelectric transport coefficients	65
Bibliography:	71
4. Conformation and Quantum-Interference-Enhanced Thermoelectric Properties of Diphenyl Diketopyrrolopyrrole Derivatives.	74
4.1. Introduction	75
4.2. Results and Discussion	77
4.3. Conclusion	96
4.4. Appendix: Supplementary calculations based on thiophene monomers and thiophene dimers	98
4.4.1. Molecular orbitals of thiophene monomer	98
4.4.2. Binding energy of thiophenes	99
4.4.3. Molecular orbitals of thiophene dimers with different connectivities	102
Bibliography	103
5. Single-Molecule Charge Transport Modulation Induced by Steric Effects of Side Alkyl Chains	107
5.1. Introduction	108

5.2. Molecular structures:	110
5.3. Results and Discussion	110
5.4. Conclusion	121
Bibliography	123
6. Conclusions and Future works	128
6.1. Conclusions	128
6.2. Future works	129
Bibliography	1322

1. Introduction to molecular-scale electronics

1.1. Molecular electronics

Molecular electronics is a field of science that aims to explore the electronic and thermal transport properties of a system containing a single molecule[1] or self-assembled monolayers (SAM)[2] connected to nanoscale electrodes (sometimes called ‘leads’) made from different materials such as metals (e.g. Au, Ag, Cu, and Ni)[3][4], semiconductors (e.g. Si)[5] or carbon (e.g. graphene [6][7], carbon nanotube[8]). In 1965, Gordon Moore noted that every 18 months the number of transistors in the chip doubles, and the size of the chip decreases by a factor of two. That is exponentially decreased with time on a logarithmic scale, which is known as Moore’s Law [52]. The exponential growth continues over half a century later, then as a component approaches the sub-10 *nm* length scale, this is approaching the limit of Moore’s Law. Therefore, the field of single-molecule electronics has the potential to offer an alternative to silicon-based devices by replacing the traditional semiconductor with a single molecule, which gives manufacturers the possibility to produce smaller, faster, and more energy-efficient devices.

Single molecules as building blocks to design and fabricate molecular electronic nanoscale devices have been explored and developed for more than 50 years[1][9][29], since Aviram and Ratner proposed the first molecular rectifier [10] as an alternative to silicon chips in the 1970s. Over the past decades, there have been numerous experimental and theoretical developments in the field of molecular electronics, which have led to multidisciplinary research involving chemistry, engineering, and physics. Fundamentally, the field has been advancing rapidly due to the following potential advantages compared to the traditional complementary metal-oxide-semiconductor (CMOS) technology. The first advantage is the potential to shrink the size of

electronics components to below the sub-10 nm scale, which could improve circuit integration and lead to energy-saving and faster performance. The second advantage is about their variety of functionalities due to quantum interference, such as conducting wires[11][12] switches[13][14][6], thermoelectric materials[15][16][17], and negative differential resistance devices[18][19][20]. The ability to use specific intermolecular interactions to assemble molecular devices is another benefit, which could result in low-cost manufacturing. As a result, single-molecule electronics have the potential to complement conventional silicon-based electronics.

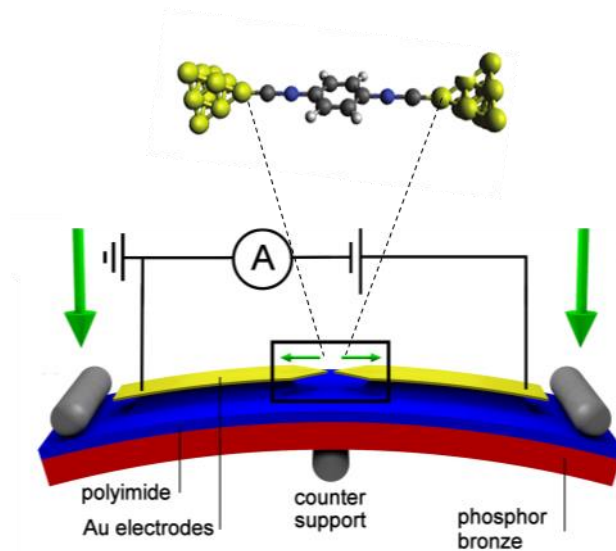


Figure 1.1.1 Schematic of mechanically controllable break junction on a bulk substrate, where the top panel shows an artist's view of the molecule located between a source and drain electrode[26].

Experimentally, one of the main challenges in designing single-molecule devices is how to fabricate a single molecule between nanoscale electrodes to study the electronic properties through systems. For that purpose, a variety of techniques have been developed to build metal-molecule-metal junction, including scanning tunneling microscope break junctions (STM-BJ)[21] [22] [23], atomic force microscopes (AFM)[29], mechanically controllable break

junctions (MCBJ, Figure 1.1.1) [24][25][26], the use of electro-migration breakdown [27] and electrochemical depositions[28, 29].

In parallel with these experimental breakthroughs, theoretical approaches have also been developed for calculating the electronic assembly of atomic structures such as density functional theory (DFT). This approach is combined with quantum transport theory for many of the calculations carried out in this thesis. SIESTA[30] is one program implementation of DFT that enables the study of finite and periodic systems[31]. By combining DFT with the Green's function formalism, the transport properties of molecular devices can be predicted. One implementation of Green's function formalism is the Gollum code[32], which is used extensively within this thesis.

Combining experimental techniques with the above theoretical framework allows researchers to construct a quantitative picture for understanding transport properties and form predictions to guide further experimental studies. Despite the fact that the development of molecular electronics has greatly accelerated experimentally, there are still some difficulties to resolve and areas to study, such as robustness, solvent effects, and electric system noise.

1.2. Molecular Junctions

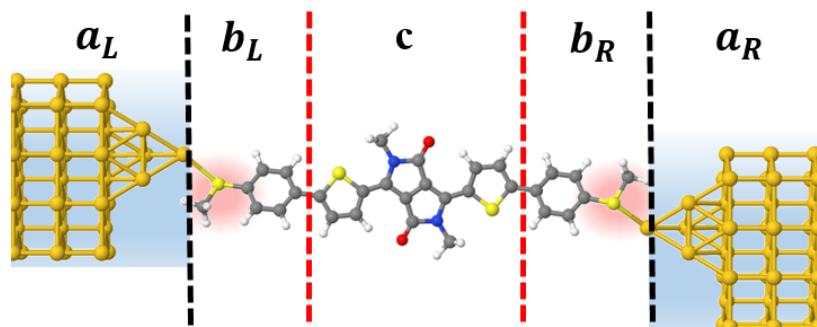


Figure 1.2.1 Schematic of a single-molecule junction: a_L and a_R are the left and right gold electrodes, b_L and b_R are left and right SMe anchor groups, which is connected to phenyl rings from both sides to the molecular backbone c , which in this example is a DPP-core.

Molecular junctions, such as that shown in Figure 1.2.1, are sensitive to very small changes in their atomic configuration. One example is that anchor groups, which are responsible for the direct contact between the metallic electrode surfaces to the molecular unit. Practically, various studies have revealed the influence of different anchor groups on molecular transport, and highlighted the importance of their mechanical stability and its electronic transparency (i.e. weak or strong coupling). The most widely used anchor group in charge transport experiments is thiol (-S)[33], due to its strong bond to gold, silver or copper electrodes[34]. Other anchor groups studied to date include amines (-NH₂), SMe, and pyridyl terminal groups, of which pyridyl has more stability and a higher probability of junction formation [35][36].

Not only anchoring groups plays an important role in molecular transport, but also the electrode material has a significant effect, which could be either metallic or non-metallic. Examples of the former include Au[37], Ag[4], Pd and Pt [38] are the most common electrodes used. To date, gold has been the electrode material mostly used, due to its noble metal character, such as good chemical stability, high conductivity, and easily prepared clean surfaces and tips. However, gold electrodes have several drawbacks, such as the mobility of surface atoms at

room temperature, which causes thermal fluctuations and instabilities[39]. For that, it is essential to find alternative materials as this might pose some advantages on how molecular electronics devices are implemented. Thus, developing other materials like the non-metallic electrodes has been attracted researchers to discover the possibility of making reliable single-molecule electrical measurements with these kinds of electrodes such as carbon-based materials[40][41], graphene[42][49] and silicon [5]. These exhibit a range of fascinating properties including electronic properties with high charge mobility, stability, mechanical strength, and flexibility of their π - conjugated structure[41][42]. Recently, the possibility of utilising superconducting electrodes has also been considered [50], which possess their interference phenomena [51], which can combine with molecular-scale CQI and DQI to yield unique interference effects.

Furthermore, molecular conformation[43] plays another crucial role in molecular transport, which has to be considered in the design of molecular junction devices due to the variety of configurations that molecules could adopt within a junction[17]. In practice, at the nanoscale device, the molecules act as an electronic circuit which is highly desirable as their small size is typically as small as one nanometer. In addition, the ability to be self-assembled onto surfaces allows the molecular units to naturally form themselves into ordered structures by non-covalent interactions. Furthermore, the length dependence of the electron transport through molecules is another important factor for defining an efficient molecular junction. The main focus of this thesis is to explore molecules with desirable properties such as aromatic organic compounds. An archetypal aromatic compound is the benzene ring, where carbon atoms are joined by alternating of double and single bonds, and the wave functions of the π system are delocalised over the whole molecule. Among different aromatic compounds, thiophene (five-membered heterocyclic ring) is considered to be an attractive ring for molecular transport (described in

chapter 4), along with related molecules containing heteroatoms (O, N, S) that are also aromatic.

In summary, anchor groups, molecular wire architectures, length dependence, and conformation variations are all key factors controlling electron transport and open up a wealth of opportunities in the chemical design of single-molecular devices. However, in electron transport experiments, the conductance of a molecular junction depends not only on the molecule itself, but also on the environment of the molecule (e.g., solvents, vacuum, or air) and on the contact geometry of the molecule with the electrodes, all of which lead to large sample-to-sample fluctuations[44].

1.3. Quantum interference

Quantum interference (QI) plays an important role in the control of quantum transport through molecular-scale structures[33][45]. This phenomenon can enhance or decrease conductance via constructive or destructive quantum interference respectively[46]. Recently, researchers have been utilising and exploring the QI concept theoretically and experimentally[33][47]. As a simple example, QI manifests itself in the conductance of benzene rings, with meta connectivity leading to DQI and low conductance, whereas para connectivity leads to CQI and high conductance.

By manipulating the connectivity of external electrodes to central rings of carbon-based molecules in single-molecule junctions, their electrical and thermoelectrical properties could be tuned. Therefore, QI provides new opportunities to construct molecular electronic devices by chemical modifications. Our focus in chapter four will be on one of these effects, namely DQI (explained in detail in chapter 4). This phenomenon greatly influences molecular

conductance, by reducing the transmission probability by orders of magnitude compared with junctions exhibiting constructive interference (CQI)[17] [31][45][46][48].

1.4. Thesis Outline

This thesis will report theoretical simulations of electron transport at the nanoscale.

Chapter 1 will give a brief discussion of molecular electronics. The development of theoretical approaches based on density functional theory (DFT), which is implemented using the SIESTA code, is discussed in chapters 2. This is combined with the Green's function formalism of transport discussed in chapter 3. Both of these methods are used extensively to study a molecules in later chapters.

Chapter 4 focuses on a theoretical study aimed at a deeper understanding of controlling QI in Diphenyl-diketopyrrolopyrrole (DPP) derivatives through manipulating the connectivity of external electrodes to their central rings, which is shown to be an effective route to tuning their electrical and thermoelectrical properties.

Chapter 5 is a collaboration with experimental colleagues, and aims to investigate the dependence of molecular conductance on the nature of branching alkyl chains (isopentane, 3-methylheptane, and 9-methylnonadecane). This confirms that the effect of insulating side chains on single-molecule conductance cannot be neglected, which is of significance for the design of future organic semiconducting materials.

Finally, chapter 6 will present conclusions and suggestions for future works.

Bibliography:

- [1] M. Kiguchi, *Single-Molecule Electronics*. Springer, 2016.
- [2] J. C. Love, L. A. Estroff, J. K. Kriebel, R. G. Nuzzo, and G. M. Whitesides, “Self-assembled monolayers of thiolates on metals as a form of nanotechnology,” *Chem. Rev.*, vol. 105, no. 4, pp. 1103–1170, 2005.
- [3] S. V Aradhya and L. Venkataraman, “Single-molecule junctions beyond electronic transport,” *Nature Nanotechnology.*, vol. 8, no. 6, pp. 399–410, 2013.
- [4] T. Kim, H. Vázquez, M. S. Hybertsen, and L. Venkataraman, “Conductance of molecular junctions formed with silver electrodes,” *Nano Lett.*, vol. 13, no. 7, pp. 3358–3364, 2013.
- [5] G. J. Ashwell *et al.*, “Molecular bridging of silicon nanogaps,” *ACS Nano*, vol. 4, no. 12, pp. 7401–7406, 2010.
- [6] Q. Wu, S. Hou, H. Sadeghi, and C. Lambert, “A single-molecule porphyrin-based switch for graphene nano-gaps,” *Nanoscale*, vol. 10, pp. 6524–6530, 2018.
- [7] Q. Wu, H. Sadeghi, V. M. García-Suárez, J. Ferrer, and C. J. Lambert, “Thermoelectricity in vertical graphene-C60-graphene architectures,” *Sci. Rep.*, vol. 7, p. 11680, 2017.
- [8] E. Penzo *et al.*, “Directed assembly of single wall carbon nanotube field effect transistors,” *ACS Nano*, vol. 10, no. 2, pp. 2975–2981, 2016.
- [9] S. J. van der Molen *et al.*, “Visions for a molecular future,” *Nat. Nanotechnol.*, vol. 8, pp. 385–389, 2013.
- [10] A. Aviram and M. A. Ratner, “Molecular rectifiers,” *Chem. Phys. Lett.*, vol. 29, no. 2,

pp. 277–283, 1974.

- [11] S. H. Choi, B. Kim, and C. D. Frisbie, “Electrical resistance of long conjugated molecular wires,” *Science* (80-.), vol. 320, no. 5882, pp. 1482–1486, 2008.
- [12] L. Lafferentz, F. Ample, H. Yu, S. Hecht, C. Joachim, and L. Grill, “Conductance of a single conjugated polymer as a continuous function of its length,” *Science* (80-.), vol. 323, no. 5918, pp. 1193–1197, 2009.
- [13] T. Sendler *et al.*, “Light-Induced Switching of Tunable Single-Molecule Junctions,” *Adv. Sci.*, vol. 2, no. 5, p. 1500017, 2015.
- [14] M. Del Valle, R. Gutiérrez, C. Tejedor, and G. Cuniberti, “Tuning the conductance of a molecular switch,” *Nat. Nanotechnol.*, vol. 2, no. 3, pp. 176–179, 2007.
- [15] M. Paulsson and S. Datta, “Thermoelectric effect in molecular electronics,” *Phys. Rev. B*, vol. 67, no. 24, p. 241403, 2003.
- [16] Q. Wu, H. Sadeghi, and C. J. Lambert, “MoS₂ nano flakes with self-adaptive contacts for efficient thermoelectric energy harvesting,” *Nanoscale*, vol. 10, no. 16, pp. 7575–7580, 2018.
- [17] R. Almughathawi, S. Hou, Q. Wu, Z. Liu, W. Hong, and C. Lambert, “Conformation and Quantum-Interference-Enhanced Thermoelectric Properties of Diphenyl Diketopyrrolopyrrole Derivatives,” *ACS Sensors*, vol. 6, no. 2, pp. 470–476, 2021.
- [18] J. Chen, W. Wang, M. A. Reed, A. M. Rawlett, D. W. Price, and J. M. Tour, “Room-temperature negative differential resistance in nanoscale molecular junctions,” *Appl. Phys. Lett.*, vol. 77, no. 8, pp. 1224–1226, 2000.
- [19] N. P. Guisinger, M. E. Greene, R. Basu, A. S. Baluch, and M. C. Hersam, “Room temperature negative differential resistance through individual organic molecules on

- silicon surfaces,” *Nano Lett.*, vol. 4, no. 1, pp. 55–59, 2004.
- [20] J. Chen, M. A. Reed, A. M. Rawlett, and J. M. Tour, “Large on-off ratios and negative differential resistance in a molecular electronic device,” *Science (80-.)*, vol. 286, no. 5444, pp. 1550–1552, 1999.
- [21] B. Xu and N. J. Tao, “Measurement of single-molecule resistance by repeated formation of molecular junctions,” *Science (80-.)*, vol. 301, no. 5637, pp. 1221–1223, 2003.
- [22] C. Li, I. Pobelov, T. Wandlowski, A. Bagrets, A. Arnold, and F. Evers, “Charge transport in single Au vertical bar alkanedithiol vertical bar Au junctions: Coordination geometries and conformational degrees of freedom,” *J. Am. Chem. Soc.*, vol. 130, no. 1, pp. 318–326, 2008.
- [23] D. Z. Manrique *et al.*, “A quantum circuit rule for interference effects in single-molecule electrical junctions,” *Nat. Commun.*, vol. 6, no. 1, pp. 1–8, 2015.
- [24] M. Teresa González, S. Wu, R. Huber, S. J. Van Der Molen, C. Schönenberger, and M. Calame, “Electrical conductance of molecular junctions by a robust statistical analysis,” *Nano Lett.*, vol. 6, no. 10, pp. 2238–2242, 2006.
- [25] M. A. Reed, C. Zhou, C. J. Muller, T. P. Burgin, and J. M. Tour, “Conductance of a molecular junction,” *Science (80-.)*, vol. 278, no. 5336, pp. 252–254, 1997.
- [26] M. L. Perrin *et al.*, “Large tunable image-charge effects in single-molecule junctions,” *Nat. Nanotechnol.*, vol. 8, no. 4, pp. 282–287, 2013.
- [27] H. Park, A. K. L. Lim, A. P. Alivisatos, J. Park, and P. L. McEuen, “Fabrication of metallic electrodes with nanometer separation by electromigration,” *Appl. Phys. Lett.*, vol. 75, no. 2, pp. 301–303, 1999.
- [28] C. Z. Li, H. X. He, and N. J. Tao, “Quantized tunneling current in the metallic nanogaps

- formed by electrodeposition and etching,” *Appl. Phys. Lett.*, vol. 77, no. 24, pp. 3995–3997, 2000.
- [29] D. Xiang, X. Wang, C. Jia, T. Lee, and X. Guo, “Molecular-Scale Electronics: From Concept to Function,” *Chem. Rev.*, vol. 116, no. 7, pp. 4318–4440, 2016.
- [30] J. M. Soler *et al.*, “The SIESTA method for ab initio order-N materials simulation,” *J. Phys. Condens. Matter*, vol. 14, no. 11, pp. 2745–2779, 2002.
- [31] C. J. Lambert, *Quantum Transport in Nanostructures and Molecules*. IOP Publishing, 2021.
- [32] J. Ferrer *et al.*, “GOLLUM: A next-generation simulation tool for electron, thermal and spin transport,” *New J. Phys.*, vol. 16, p. 093029, 2014.
- [33] C. J. Lambert, “Basic concepts of quantum interference and electron transport in single-molecule electronics,” *Chemical Society Reviews*. pp. 875–888, 2015.
- [34] N. B. Luque and E. Santos, “Ab Initio Studies of Ag–S Bond Formation during the Adsorption of l-Cysteine on Ag (111),” *Langmuir*, vol. 28, no. 31, pp. 11472–11480, 2012.
- [35] R. Frisenda *et al.*, “Electrical properties and mechanical stability of anchoring groups for single-molecule electronics,” *Beilstein J. Nanotechnol.*, vol. 6, no. 1, pp. 1558–1567, 2015.
- [36] Y. Ie *et al.*, “Nature of electron transport by pyridine-based tripodal anchors: Potential for robust and conductive single-molecule junctions with gold electrodes,” *J. Am. Chem. Soc.*, vol. 133, no. 9, pp. 3014–3022, 2011.
- [37] F. Schwarz and E. Lörtscher, “Break-junctions for investigating transport at the molecular scale,” *J. Phys. Condens. Matter*, vol. 26, no. 47, pp.1-21, 2014.

- [38] V. M. García-Suárez, A. R. Rocha, S. W. Bailey, C. J. Lambert, S. Sanvito, and J. Ferrer, “Single-channel conductance of H₂ molecules attached to platinum or palladium electrodes,” *Phys. Rev. B*, vol. 72, no. 4, p. 45437, 2005.
- [39] J. C. Cuevas and E. Scheer, *Molecular electronics: an introduction to theory and experiment*. World Scientific, 2010.
- [40] Z. Tan *et al.*, “Atomically defined angstrom-scale all-carbon junctions,” *Nat. Commun.*, vol. 10, no. 1, pp. 4–10, 2019.
- [41] X. H. Zheng, G. R. Zhang, Z. Zeng, V. M. García-Suárez, and C. J. Lambert, “Effects of antidots on the transport properties of graphene nanoribbons,” *Phys. Rev. b*, vol. 80, no. 7, p. 75413, 2009.
- [42] P. Gehring *et al.*, “Distinguishing Lead and Molecule States in Graphene-Based Single-Electron Transistors,” *ACS Nano*, vol. 11, no. 6, pp. 5325–5331, 2017.
- [43] C. M. Finch, S. Sirichantaropass, S. W. Bailey, I. M. Grace, V. M. García-Suárez, and C. J. Lambert, “Conformation dependence of molecular conductance: Chemistry versus geometry,” *J. Phys. Condens. Matter*, vol. 20, no. 2, pp. 22203, 2008.
- [44] Y. Selzer and D. L. Allara, “Single-molecule electrical junctions,” *Annu. Rev. Phys. Chem.*, vol. 57, pp. 593–623, 2006.
- [45] C. J. Lambert, H. Sadeghi, and Q. H. Al-Galiby, “Quantum-interference-enhanced thermoelectricity in single molecules and molecular films,” *Comptes Rendus Phys.*, vol. 17, no. 10, pp. 1084–1095, 2016.
- [46] J. Liu, X. Huang, F. Wang, and W. Hong, “Quantum interference effects in charge transport through single-molecule junctions: detection, manipulation, and application,” *Acc. Chem. Res.*, vol. 52, no. 1, pp. 151–160, 2018.

- [47] F. Evers, R. Korytár, S. Tewari, and J. M. Van Ruitenbeek, “Advances and challenges in single-molecule electron transport,” *Rev. Mod. Phys.*, vol. 92, no. 3, 2020.
- [48] R. Frisenda, V. A. E. C. Janssen, F. C. Grozema, H. S. J. Van Der Zant, and N. Renaud, “Mechanically controlled quantum interference in individual π -stacked dimers,” *Nat. Chem.*, vol. 8, no. 12, pp. 1099–1104, 2016.
- [49] S. Bailey, D. Visontai, C. J. Lambert, M. R. Bryce, H. Frampton, and D. Chappell, “A study of planar anchor groups for graphene-based single-molecule electronics,” *J. Chem. Phys.*, vol. 140, no. 5, 2014.
- [50] N. L. Plaszkó, P. Rakya, J. Cserti, A. Kormányos, and C. J. Lambert, “Quantum interference and nonequilibrium josephson currents in molecular andreev interferometers,” *Nanomaterials*, vol. 10, no. 6, p. 1033, 2020.
- [51] V. C. Hui and C. J. Lambert, “Andreev scattering, universal conductance fluctuations and phase periodic transport,” *Epl (Europhysics Lett.)*, vol. 23, no. 3, pp. 203–209, 1993.
- [52] G. E. Moore, *Cramming more components onto integrated circuits*. Electronics, vol. 38, no. 8, 1965.

2. Density Functional Theory

2.1. Introduction

In order to investigate the electronic properties of molecular electronic devices, theoretical tools are needed for solving the interacting electron problem. In order to solve the interacting many-body Schrödinger equation, there are several theoretical methodologies that can be used such as molecular dynamics, wavefunction methods, and Quantum Monte Carlo. Density function theory (DFT) is one of the most common methodologies used by physicists and chemists. DFT calculates the ground-state of the organic molecules based on two major theorems named: the Hohenberg-Kohn Theorem(1964) and the Kohn-Sham Formulation[1][2]which will be fully explained in this chapter.

The main aim of this chapter is to give a brief outline of DFT and the computational code ‘SIESTA’(Spanish Initiative for Electronic Simulations with Thousands of Atoms)[3], which I have used extensively throughout my Ph.D. research to optimise molecule structures, calculate charge densities, binding energies, and band structures as well as generating Hamiltonians for the next-step charge transport calculations.

The first part of this chapter is an introduction of the DFT methodologies with the main formalism as a method to find the solution of the non-relativistic many-particle, time-independent Schrödinger equation (TISE), since the properties of a many-electron system can be obtained from electron density. The second part displays a brief overview of the foundations and numerical applications of DFT to simplify the problems and perform reliable, precise calculations on molecular structures, no matter how massive scale these systems are. This has led DFT to become one of the main tools in theoretical physics.

2.2. The Schrödinger Equation

In general, the Hamiltonian for any given non-relativistic Schrödinger equation can be employed to describe all many-body systems as follows:

$$H\Psi_i(\vec{r}_1, \vec{r}_2, \dots, \vec{r}_N, \vec{R}_1, \vec{R}_2, \dots, \vec{R}_M) = E_i\Psi_i(\vec{r}_1, \vec{r}_2, \dots, \vec{r}_N, \vec{R}_1, \vec{R}_2, \dots, \vec{R}_M) \quad (2.1)$$

The variable H represents the Hamiltonian time-independent operator of a system consisting of N -electrons and M -nuclei, which describes the interaction of particles with each other, whereas ψ_i is the wavefunction of the i^{th} state of the system and E_i is the numerical value of the energy of the i^{th} state described by ψ_i . For such a system, the Hamiltonian operator can be written as [4]

$$H = \underbrace{-\frac{\hbar^2}{2m_e} \sum_{i=1}^N \nabla_i^2}_{\widehat{T}_e} - \underbrace{\frac{\hbar^2}{2m_n} \sum_n^M \nabla_n^2}_{\widehat{T}_n} + \underbrace{\frac{1}{4\pi\epsilon_0} \sum_{i=1}^N \sum_{n=1}^M \frac{Z_n e^2}{|\vec{r}_i - \vec{R}_n|}}_{\widehat{V}_{en}} \quad (2.2)$$

$$+ \underbrace{\frac{1}{4\pi\epsilon_0} \frac{1}{2} \sum_{i \neq j}^N \frac{e^2}{|\vec{r}_i - \vec{r}_j|}}_{\widehat{V}_e} + \underbrace{\frac{1}{4\pi\epsilon_0} \frac{1}{2} \sum_{n=1}^M \sum_{n \neq n'}^M \frac{Z_n Z_{n'} e^2}{|\vec{R}_n - \vec{R}_{n'}|}}_{\widehat{V}_n}$$

The Hamiltonian of the many-body system is divided into five terms: \widehat{T}_e and \widehat{T}_n represent the kinetic energy of electrons and nuclei respectively and \widehat{V}_{en} defines the attractive electrostatic interaction between electrons and nuclei. \widehat{V}_e is the electron-electron interaction and \widehat{V}_n is nucleon-nucleon interaction where they describe the repulsive part of the potential respectively. Where i and j represent the N -electrons while n and n' run over the M -nuclei in the system, m_e and m_n are the mass of electron and nucleus respectively, e and Z_n are the electrons and nuclear charge respectively. The position of the electrons and nuclei are denoted as \vec{r}_i and \vec{R}_n respectively, and ∇_i^2 is the Laplacian operator, in Cartesian coordinates ∇_i^2 is defined as:

$$\nabla_i^2 = \frac{\partial^2}{\partial x_i^2} + \frac{\partial^2}{\partial y_i^2} + \frac{\partial^2}{\partial z_i^2} \quad (2.3)$$

Solving the exact solution of the Schrödinger equation for a many-body system is quite complicated for more electrons. However, an accurate approximate solution may be found, as described below.

2.3. Born-Oppenheimer approximation:

Unlike the simple hydrogen atom problem, the Schrödinger equation (2.1) cannot be solved for more than a few electrons. For that purpose, an approach assumed to reduce this problem, due to the fact that the mass of the nucleons is bigger than the electron mass (at least three orders of magnitude larger)[5][6], this causes their velocities of motion to be much lower. Thus, the nuclei can be considered as a classical particle (i.e. their kinetic energy is neglected), which creates a fixed external potential and treat the electrons as quantum particles subject to this potential. This is the well-known as the Born-Oppenheimer approximation[5], with the assumption that the nucleon wavefunction is independent of the electron position. Approximately, the classical interaction term of nuclei \widehat{V}_n in Eq. 2.2 have no contribution to the electronic description structure. Thus, the Schrödinger equation reduces into electronic Hamiltonian parts:

$$H_e = \overbrace{-\frac{\hbar^2}{2m_e} \sum_{i=1}^N \nabla_i^2}^{T_e} - \overbrace{\frac{1}{4\pi\epsilon_0} \sum_{i=1}^N \sum_{n=1}^M \frac{Z_n e^2}{|\vec{r}_i - \vec{R}_n|}}^{V_{en}} + \overbrace{\frac{1}{4\pi\epsilon_0} \frac{1}{2} \sum_{i \neq j}^N \frac{e^2}{|\vec{r}_i - \vec{r}_j|}}^{V_e} \quad (2.4)$$

$$\text{Then } H_e \Psi_e = E_e \Psi_e$$

$$\left\{ \overbrace{-\frac{\hbar^2}{2m_e} \sum_{i=1}^N \nabla_i^2}^{T_e} - \overbrace{\sum_{i=1}^N \sum_{n=1}^M V_{ext}(r_i)}^{V_{en}} + \frac{1}{4\pi\epsilon_0} \frac{1}{2} \overbrace{\sum_{i \neq j}^N \frac{e^2}{|\vec{r}_i - \vec{r}_j|}}^{V_e} \right\} \Psi_e = E_e \Psi_e \quad (2.5)$$

where the variable $V_{ext}(r_i)$ is the external potential due to the nuclei-electron interaction. This approximation allows the electron and nucleon degrees of freedom to be decoupled. Despite the fact that the Born-Oppenheimer approximation reduces the size of the system, solving Eq. 2.5 remains challenging, even on a modern supercomputer. Nevertheless, solving this problem needs further approaches using DFT such as Hartree, Hartree-Fock, or other quantum mechanical methods. While Hartree-Fock captures the exchange energy, it ignores electron correlations, DFT theory solves this issue by expressing the physical quantities in terms of the ground-state density $\rho(\vec{r})$ [7], this was first attempted by the Hohenberg-Kohn theorem.

2.4. Hohenberg-Kohn theorem approximation:

The Hohenberg-Kohn theorem developed in 1964[1], is a fundamental building block of DFT, due to the ability to determine the properties of the ground-state density $\rho(\vec{r})$ system. This corresponds to a minimum total energy functional and can be applied to a many-electron system that interacts with an applied external potential $V_{ext}(\vec{r})$.

$$\hat{H} = \hat{T}_e + \hat{V}_e + \sum_{i=1}^N \sum_{n=1}^M V_{ext}(r_i) \quad (2.6)$$

This theorem tells us that the total energy of the many-electron system is as a function of the density $\rho(\vec{r})$, which is written as the following:

$$E_{HK}[\rho(\vec{r})] = F_{HK}[\rho(\vec{r})] + \int V_{ext}(\vec{r}) \rho(\vec{r}) d\vec{r} \quad (2.7)$$

Where

$$F_{HK} = T_{int}[\rho(\vec{r})] + \underbrace{E[\rho(\vec{r})]}_{\substack{=zero, \text{ for} \\ \text{non-interacting} \\ \text{system}}} \quad (2.8)$$

F_{HK} is the potential energies of the many-electron interaction system. This theorem relies on two powerful statements:

Statement 1: For any interacting many-particle systems in external potential $V_{ext}(\vec{r})$, the ground-state density $\rho(\vec{r})$ of the system is uniquely defined. This expression shows that there cannot be two external potentials $V_{ext}(\vec{r})_{(1)} \neq V_{ext}(\vec{r})_{(2)} + \text{constant}$, which leads to the same ground-state density distribution. [1][4][8][9]

Statement 2: In terms of the density $\rho(\vec{r})$, we can define a global function for the energy $E[\rho(\vec{r})]$. For that, the exact ground-state energy of the system in the presence of the external potential ($V_{ext}(\vec{r})$) is the global minimum value of this functional and the density $\rho(\vec{r})$ which minimizes the functional and represents the exact ground-state density $\rho_{GS}(\vec{r})$. [1][4][8][9]

2.5. The Kohn-Sham Approach

Kohn and Sham's approach[2],[10],[11] introduced a solution by using independent particle equations for the non-interacting electrons system to solve the many-body problem by Kohn and Sham in 1965. This approach generates the same ground-state density for any given system of interacting particles as a self-consistent method[2][12]. Kohn and Sham assume that it is possible to replace the original Hamiltonian of the system with an effective Hamiltonian (H_{eff}) of the non-interacting system in an effective external potential $V_{eff}(\vec{r})$, which gives rise to the same ground-state density as the initial system. Since there is no clear procedure for performing the calculation, the Kohn-Sham method is considered as an ansatz, but it is

considerably easier to solve it than the interacting problem. The Kohn-Sham approach based on the Hohenberg-Kohn universal density is:

$$F_{HK}[\rho(\vec{r})] = T_{int}[\rho(\vec{r})] + V_e[\rho(\vec{r})] \quad (2.9)$$

Based on the Hohenberg-Kohn functional for non-interacting electrons in Eq.2.7, the ground-state functional of the Kohn-Sham ansatz $F_{KS}[\rho(\vec{r})]$ can be written as

$$F_{KS}[\rho(\vec{r})] = T_{non}[\rho(\vec{r})] + E_{Hart}[n\rho(\vec{r})] + \int V_{ext}(\vec{r})\rho(\vec{r})d\vec{r} + E_{xc}[\rho(\vec{r})] \quad (2.10)$$

The variable T_{non} represents the kinetic energy of the non-interacting system which is different from T_{int} (for interaction system) in Eq.2.8, and E_{Hart} represents the classical electrostatic energy or classical self-interaction energy of the electron gas which is associated with density $\rho(\vec{r})$. The last term $E_{xc}[\rho(\vec{r})]$ is the exchange-correlation energy functional, which is the difference between the kinetic energy for the interacting and non-interacting systems and is given by:

$$E_{xc}[\rho(\vec{r})] = F_{HK}[\rho(\vec{r})] - \overbrace{\frac{1}{2} \int \frac{\rho(\vec{r}_1)\rho(\vec{r}_2)}{|\vec{r}_1 - \vec{r}_2|} d\vec{r}_1 d\vec{r}_2}^{E_{Hart}[\rho(\vec{r})]} - T_{non}[\rho(\vec{r})] \quad (2.11)$$

This variational equation is for a non-interacting electron system with the same $\rho(\vec{r})$ ground-state energy and density as the interacting electron system. In the last couple of decades, multiple efforts have been intensively explored into finding a better computation of $E_{xc}[\rho(\vec{r})]$. Currently, functional can be used to explore and predict the physical characteristics of a wide range of solid-state systems and molecules. Therefore, we take the functional derivatives to construct the effective single-particle potential $V_{eff}(\vec{r})$ for the last three terms in Eq. 2.10

$$V_{eff}(\vec{r}) = V_{ext}(\vec{r}) + \frac{\partial E_{Hart}[\rho(\vec{r})]}{\partial \rho(\vec{r})} + \frac{\partial E_{xc}[\rho(\vec{r})]}{\partial \rho(\vec{r})} \quad (2.12)$$

Significantly, the potential $V_{eff}(\vec{r})$ can be used to give the Hamiltonian of the single particle as

$$H_{KS} = T_{non} + V_{eff} \quad (2.13)$$

By applying this Hamiltonian, the Schrödinger equation becomes

$$[T_{non} + V_{eff}]\Psi_{KS} = E\Psi_{KS} \quad (2.14)$$

This expression above is named as Kohn-Sham equation. The Kohn-Sham method demonstrates that a complicated many-body interaction system can be mapped onto a set of simple non-interacting equations precisely if the exchange-correlation functional is known. However, because the exchange-correlation functional is unknown, approximations must be made.

2.5.1. Exchange and correlation functional

DFT is a very reliable and proven method used in the analysis although it is still used as an approximation for the kinetic energy functional and the exchange-correlation functional in terms of the density. Additionally, DFT has been successful to reduce the quantum mechanical ground-state many-body problems to a self-consistent one-electron problem, by the Kohn-Sham equation[8]. This method is formally accurate, while for practical calculations there is no exact form to evaluate the exchange-correlation energy E_{xc} as a function of the density. There are several proposed forms for the exchange and correlation, the local density approximation (LDA) has long been the standard choice[13]. Despite its simple nature, the predictions made using LDA give realistic descriptions of the atomic structure, elastic, and vibrational characteristics for a wide range of systems. Yet, LDA is generally not accurate enough to describe the energetics of chemical reactions (heats of reaction and activation energy

barriers), which lead to an overestimate of the binding energies of molecules and solids. As well, there are numerous examples where the LDA puts molecular conformations or crystal bulk phases in an even qualitatively wrong energetic order [14].

Currently, Generalised gradient approximations (GGA's) have overcome such deficiencies to a considerable extent[8][15], giving, for example, a more realistic description of energy barriers in the dissociative adsorption of hydrogen on metal and semiconductor surfaces[16]. Gradient corrected (GGA) functional depends on the local density and the spatial variation of the density. Therefore, the most commonly exchange-correlation functional approximations are LDA[13] and GGA, which rely on the density and the local density with a complicated technique that involves the derivatives of density respectively. To give more information about LDA and GGA, the following section will briefly explain them.

2.5.1.1. Local Density Approximation (LDA)

The LDA approximation assumes that the exchange-correlation functional depends only on the local density which was introduced by Kohn and Sham's approach[2][10], and therefore gives a good prediction for any system with slowly varying the local density. The formula of this simplest exchange-correlation approximation is

$$E_{xc}^{LDA}[\rho(\vec{r})] = \int \rho(\vec{r}) E_{xc}^{homo}[\rho(\vec{r})] d(\vec{r}) \quad (2.15)$$

The term E_{xc}^{homo} is defined as the exchange-correlation energy of the homogeneous electron gas with a density $\rho(\vec{r})$. In order to obtain this term $E_{xc}^{homo}[\rho(\vec{r})]$ it is useful to split into the sum of two contributions such as:

$$E_{xc}^{homo}[\rho(\vec{r})] = E_x^{homo}[\rho(\vec{r})] + E_c^{homo}[\rho(\vec{r})] \quad (2.16)$$

Where the first term is related to the exchange part $E_x^{homo}[\rho(\vec{r})]$ and the second t is related to the correlation energies $E_c^{homo}[\rho(\vec{r})]$. Nonetheless, LDA functional is considered accurate for

the homogenous system with (S and P) orbitals such as graphene, carbon nanotube, or where the electron density is not rapidly changing. While for atoms with (d and f) orbitals, there is an expected error as the LDA treats the homogenous system.

2.5.1.2. Generalized Gradient Approximation (GGA)

The LDA approximation is inaccurate for the real inhomogeneous system where the electron density is changing rapidly at point (\vec{r}), which means LDA is inexact for heavy atoms such as molecules. Therefore, it is necessary to find an alternative approximation that considers the gradient of the electron density to be more accurate, which is called generalized gradient approximation GGA. Therefore, the GGA approximation extends the LDA by involving the higher spatial derivatives of the total charge density ($|\nabla\rho(\vec{r})|, |\nabla^2\rho(\vec{r})|, \dots$) into the functional form of the exchange and correlation energies.

In the GGA approximation, there is no closed-form for the exchange term of the functional, but it has been calculated along with the correlation contribution by using numerical methods. Hence, several parameterizations are used in this approximation, and in this section we discuss one of them, which is introduced by Perdew Burke and Ernzerhof (PBE functional form)[15], the correlation energy is given by:

$$E_{xc}^{GGA}[\rho(\vec{r})] = \int \rho(\vec{r}) \varepsilon_{xc}^{GGA}[\rho(\vec{r}), |\nabla\rho(\vec{r})|] d(\vec{r}) \quad (2.17)$$

2.6. SIESTA

SIESTA is an acronym derived from the Spanish Initiative for Electronic Simulations with Thousands of Atoms[3]. It is a self-consistent density functional theory technique, which uses norm-conserving pseudo-potentials and a Linear Combination of Atomic Orbital Basis set (LCAOB) to perform efficient calculations. All calculation presented in this thesis has been

carried out by the implementation of DFT in the SIESTA code, this code is used to demonstrate the electronic properties of the relaxed structures for example the charge density, the binding energy, and several other features. Then, the next section will describe theoretical details about this code and provide some of SIESTA's components and how they are implemented within the code[17].

2.6.1. The Pseudopotential Approximation

Since the SIESTA code requires an approximation to make a reliable calculation, one approximation example is called a pseudo-potential or effective potential. This helps to solve the many-body Schrödinger equation by reducing the number of electrons involved in the simulation. The idea of this approximation concept is that electrons in the atom are split into two types: the first is the core electrons in which the electrons occupy the filled shells of the atomic orbitals and the second is the valence electrons that lie in the partially filled atomic shells. Therefore, the pseudopotential is constructed by attempting to replace the complicated effects of the motion of the non-valence electrons (core electrons) of an atom and the nucleus by pseudo-potential. This is based on the fact that the core electrons in most molecules do not participate in chemical bonding to the formation of the molecular orbitals. Thus, Fermi introduced this assumption in 1934[18], and there are special kinds of pseudopotentials are used in our calculation.

Since only the valence electrons play a critical role in determining the majority of chemical characteristics. The approximation is permitted to take advantage of just treating the valence electrons to eliminate the core electrons due to the fast interaction with the atomic nucleus. Generally, the valence electrons must be included because their states overlap with the other valence electron states from surrounding atoms in constructing the molecular orbital.

2.6.2. Calculating binding energies using the counterpoise method (CP)

Using the DFT approach to calculate the ground-state energy of different molecules and allows to calculate the binding energies between different parts of the system as well as optimum energy. However, these calculations are subject to errors using SIESTA code, due to localized basis sets, which are centred on the nuclei. At the point when atoms are close to each other, then their basis functions will overlap, which might cause artificial strengthening of the atomic interaction and it could give inaccurate total energy of the system. Generally, the solution of this type of error has been performed by the Basis Set Superposition Error correction (BSSE)[19] or the counterpoise correction[20].

By assuming two molecular systems, which are labelled as system **A**, and system **B**, then the interaction binding energy can be expressed as

$$\Delta E(AB) = E_{AB}^{AB} - E_A^A - E_B^B \quad (2.18)$$

Where E_{AB}^{AB} is the total energy of the supersystem, E_A^A and E_B^B are the total energies of the isolated components. In the expression above, the superscript specifies the basis set utilised in each computation, i.e. **A** represents the basis set of system **A**, **B** represents the basis set of system **B**, and **AB** represents the combined basis set of systems **A** and **B**. In order to eliminate the numerical errors, it is useful to perform the energy calculations in the same total basis set of the **AB** system. This can be achieved in SIESTA by recalculating using the mixed basis sets and introducing the ghost orbitals (basis set functions that have no electrons or protons), then subtracting the error from the uncorrected energy to calculate the binding energy by the following expression

$$\Delta E(AB) = E_{AB}^{AB} - E_A^{AB} - E_B^{AB} \quad (2.19)$$

Where E_A^{AB} and E_B^{AB} are the energies of system **A** and system **B** which are evaluated based on the supersystem. Therefore, this is a crucial concept that has been implemented in several

systems to produce reliable and realistic results[21][22]. The figure below shows the cartoon of the origin of the basis set in a counterpoise calculation.

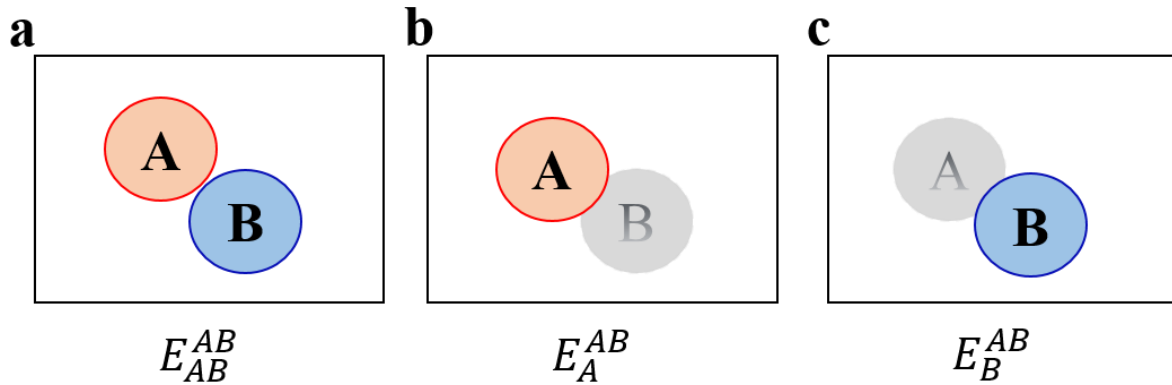


Figure 2.6.1 illustrating the method to calculate the binding energy. (a) represents basis functions for a total system **AB** where atoms are shown in red and blue circles; (b) represents a basis function for individual system **A** where system **B** is a ghost state represented by the blue dashed circle; (c) represents a basis function for individual system **B** where system **A** is a ghost state represented by the red dashed circle. In practice, the basis set in a counterpoise calculation is most easily defined by setting the nuclear charge of the corresponding system to zero.

2.7. Calculations in Practice

The SIESTA code is used in this thesis to calculate transport calculations during several steps. The first step is to construct the atomic configurations of the system, and then the appropriate pseudopotentials for each element are required, which is distinctive for each exchange-correlation functional. Computationally, precise calculations take a long time with a larger memory using, therefore it is a crucial point to choose an appropriate basis set to decrease both time and memory needed. A further point to ensure the accuracy of the calculation is to include the grid fineness and density convergence tolerances. In addition, the Pulay parameter is an example of the convergence controlling parameter, which accelerates or maintains the stability of the convergence of the charge density in SIESTA.

The next step is to generate the required initial charge density, assuming that there is no interaction between atoms. In the case that the pseudopotentials are known, the sum of charge densities is the total charge density. Figure 2.7.1 shows the self-consistent calculation, which begins by calculating the Hartree and exchange-correlation potential. Therefore, a new charge density is obtained by solving the Kohn-Sham equation, thus the next iteration is started and repeated several times until the essential convergence criteria is reached. This means that the Kohn and Sham ground-state orbitals and energy for given atomic configurations are achieved.

For the case of the structure optimisation (i.e. relaxing atomic coordinates, allowing periodic cell shapes and volumes to change), it is described in another loop, which is controlled via the conjugate gradient method[23][24]. This leads to the minimum ground-state energy of the atoms in the system and the equilibrium lattice parameters of the systems. Finally, when this method of self-consistency is implemented, the Hamiltonian and the density matrices are computed. This is important, as they are necessary for the quantum transport calculations in the next chapter.

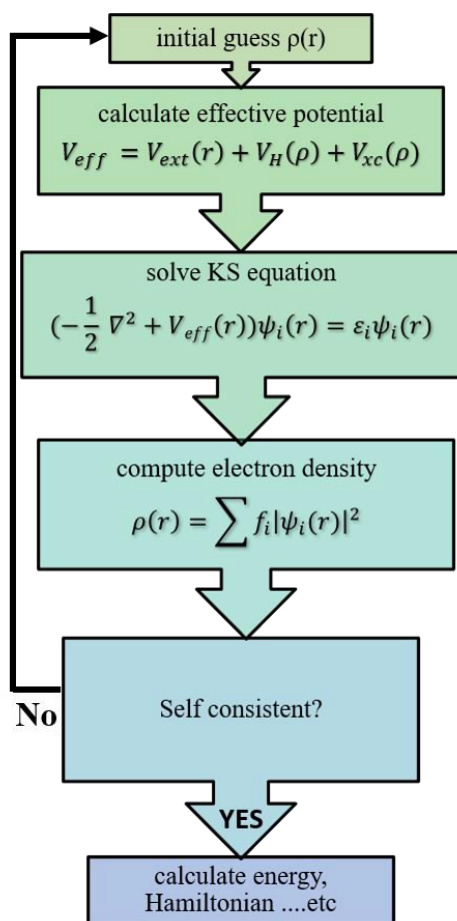


Figure 2.7.1 Schematic of the self-consistency process within SIESTA.

Bibliography:

- [1] P. Hohenberg and W. Kohn, “Inhomogeneous electron gas,” *Phys. Rev.*, vol. 136, no. 3B, p. B864, 1964.
- [2] W. Kohn and L. J. Sham, “Self-consistent equations including exchange and correlation effects,” *Phys. Rev.*, vol. 140, no. 4A, p. A1133, 1965.
- [3] J. M. Soler *et al.*, “The SIESTA method for ab initio order-N materials simulation,” *J. Phys. Condens. Matter*, vol. 14, no. 11, pp. 2745–2779, 2002.
- [4] R. M. Martin, *Electronic structure: basic theory and practical methods*. Cambridge university press, 2004.
- [5] M. Born and J. R. Oppenheimer, “On the quantum theory of molecules,” *Ann. Physik*, vol. 84, no. 20, pp. 457–484, 1927.
- [6] A. Bartók-Pirtay, *The Gaussian Approximation Potential: an interatomic potential derived from first principles quantum mechanics*. Springer Science & Business Media, 2010.
- [7] V. Sahni, “The Hohenberg-Kohn Theorems and Kohn-Sham Density Functional Theory,” in *Quantal Density Functional Theory*, Springer, 2004, pp. 99–123.
- [8] W. Kohn, A. D. Becke, and R. G. Parr, “Density functional theory of electronic structure,” *J. Phys. Chem.*, vol. 100, no. 31, pp. 12974–12980, 1996.
- [9] W. Kohn, “Nobel Lecture: Electronic structure of matter—wave functions and density functionals,” *Rev. Mod. Phys.*, vol. 71, no. 5, p. 1253, 1999.
- [10] R. M. Dreizler and E. K. U. Gross, *Density functional theory: an approach to the*

quantum many-body problem. Springer Science & Business Media, 2012.

- [11] W. Yang, “Direct calculation of electron density in density-functional theory,” *Phys. Rev. Lett.*, vol. 66, no. 11, p. 1438, 1991.
- [12] R. G. Parr, “Density functional theory of atoms and molecules,” in *Horizons of quantum chemistry*, Springer, 1980, pp. 5–15.
- [13] R. O. Jones and O. Gunnarsson, “The density functional formalism, its applications and prospects,” *Rev. Mod. Phys.*, vol. 61, no. 3, pp. 689–746, 1989.
- [14] J. C. Grossman, L. Mitas, and K. Raghavachari, “Structure and stability of molecular carbon: importance of electron correlation,” *Phys. Rev. Lett.*, vol. 75, no. 21, p. 3870, 1995.
- [15] J. P. Perdew, K. Burke, and M. Ernzerhof, “Generalized gradient approximation made simple,” *Phys. Rev. Lett.*, vol. 77, no. 18, p. 3865, 1996.
- [16] E. Penev, P. Kratzer, and M. Scheffler, “Effect of the cluster size in modeling the H₂ desorption and dissociative adsorption on Si (001),” *J. Chem. Phys.*, vol. 110, no. 8, pp. 3986–3994, 1999.
- [17] D. Sánchez-Portal, P. Ordejon, E. Artacho, and J. M. Soler, “Density-functional method for very large systems with LCAO basis sets,” *Int. J. Quantum Chem.*, vol. 65, no. 5, pp. 453–461, 1997.
- [18] E. Fermi, “Motion of neutrons in hydrogenous substances,” *Ric. Sci.*, vol. 7, no. 2, pp. 13–52, 1936.
- [19] H. B. Jansen and P. Ros, “Non-empirical molecular orbital calculations on the

- protonation of carbon monoxide,” *Chem. Phys. Lett.*, vol. 3, no. 3, pp. 140–143, 1969.
- [20] S. F. Boys and F. Bernardi, “The calculation of small molecular interactions by the differences of separate total energies. Some procedures with reduced errors,” *Mol. Phys.*, vol. 19, no. 4, pp. 553–566, 1970.
- [21] P. D. Haynes, C.-K. Skylaris, A. A. Mostofi, and M. C. Payne, “Elimination of basis set superposition error in linear-scaling density-functional calculations with local orbitals optimised in situ,” *Chem. Phys. Lett.*, vol. 422, no. 4–6, pp. 345–349, 2006.
- [22] A. D. Boese, G. Jansen, M. Torheyden, S. Höfener, and W. Klopper, “Effects of counterpoise correction and basis set extrapolation on the MP2 geometries of hydrogen bonded dimers of ammonia, water, and hydrogen fluoride,” *Phys. Chem. Chem. Phys.*, vol. 13, no. 3, pp. 1230–1238, 2011.
- [23] M. C. Payne, M. P. Teter, D. C. Allan, T. A. Arias, and J. D. Joannopoulos, “Iterative minimization techniques for ab initio total-energy calculations: molecular dynamics and conjugate gradients,” *Rev. Mod. Phys.*, vol. 64, no. 4, p. 1045, 1992.
- [24] W. H. Press *et al.*, *Numerical recipes in Pascal: the art of scientific computing*, vol. 1. Cambridge university press, 1989.

3. Transport theory

3.1. Introduction:

Molecular electronics has been the subject of intensive research, both theoretically and experimentally[1][2]. One of the fundamental challenges is to understand the electronic transport properties of nanoscale devices, where a molecule (or sufficiently small structure) is bound to electrodes so that ballistic transport can occur through its energy levels. Therefore, as mentioned in chapter 1, the contact strength between the molecule and the metallic electrodes plays a significant role in determining the transport properties, due to scattering processes within a lead|molecule|lead framework. Thus, the Green's function formalism is the most widely used theoretical method for studying the scattering process in these systems.

Section 3.2 aims to present important background information regarding Landauer formalism. Since the energy of electrons passing through a nanoscale device is conserved, the electric current flowing can be described by the Landauer formula. This provides a description of the properties of electronic transport, and how they are related to the transmission coefficient for electrons passing from one lead through the scatterer to the other lead. The main problem in scattering theory is to compute the transmission and reflection amplitudes, which are described in section 3.3, followed by the Green's function approach for different transport systems, which is presented in section 3.4 and is used to calculate the transmission coefficient $T(E)$ across the scattering region. As a simple example, the transmission coefficient $T(E)$ is derived in a molecular junction by taking a one-dimensional system where electrons with energy E pass from one electrode to another. In the final section, I will illustrate generic features of resonances in the transmission coefficient, which are derived based on a simple tight-binding model system

connected to two semi-infinite one-dimensional electrodes, like the Breit-Wigner formula for on-resonance transmission.

3.2. The Landauer formula

The Landauer formula[3][4] is the standard theoretical model to describe the transport phenomena of non-interacting electrons for a scattering region in the terms of a Fermi distribution and a transmission coefficient of the connected electrodes. It is assumed that the system consists of two ideal ballistic leads (which are connected to two electron reservoirs) and a scattering region as shown in Figure 3.2.1

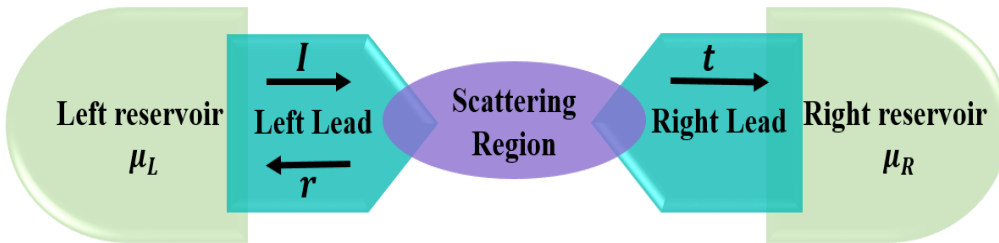


Figure 3.2.1: A generic scattering region is connected to two ballistic leads with the chemical potentials μ_L and μ_R respectively, where r is the amplitude of the reflected wave due to an incoming wave from the left and t is the amplitude of the transmitted wave.

These reservoirs supply the system with electrons and have slightly different chemical potentials ($\mu_L - \mu_R > 0$), which will drive electrons from the left to the right reservoir. When the temperature is equal to zero ($T = 0 K$), in the absence of the scattering region, the current δI in such a system due to left moving electrons in an energy interval δE is $\delta I = e v_g \delta n$, where $\delta n = \frac{\partial n}{\partial E} \delta E$ is the number of left-moving electrons per unit length in the energy interval δE and v_g is their group velocity. If left and right-moving electrons are emitted by the reservoirs, then the net current is carried by electrons in the energy range $\delta E = \mu_L - \mu_R$ and therefore

$$\delta I = e v_g \frac{\partial n}{\partial E} \delta E = e v_g \frac{\partial n}{\partial E} (\mu_L - \mu_R) \quad (3.2.1)$$

The parameters are defined as e is the electronic charge, v_g is the group velocity and $\frac{\partial n}{\partial E}$ is the density of states (*DOS*) per unit length, which is related to the group velocity by

$$\frac{\partial n}{\partial E} = \frac{\partial n}{\partial k} \frac{\partial k}{\partial E} = \frac{\partial n}{\partial k} \frac{1}{v_g \hbar} \quad (3.2.2)$$

In one-dimension, where $\frac{\partial n}{\partial k} = \frac{1}{2\pi} \times 2$ for spin, and the group velocity is $v_g = \frac{1}{\hbar} \frac{dE}{dk}$, this simplifies Eq. 3.2.2 to:

$$\frac{\partial n}{\partial E} = \frac{2}{v_g \hbar} \quad (3.2.3)$$

Substituting Eq. 3.2.3 into Eq. 3.2.1 yields

$$\delta I = \frac{2e}{\hbar} (\mu_L - \mu_R) \quad (3.2.4)$$

If δV represents the voltage corresponding to the chemical potential difference, so that $\mu_L - \mu_R = e\delta V$, one obtains

$$\delta I = \frac{2e^2}{\hbar} \delta V \quad (3.2.5)$$

Equation 3.2.5 states that the conductance for a one-dimensional lead containing one open channel in absence of scattering region given by

$$G_0 = \frac{2e^2}{\hbar} \quad (3.2.6)$$

This is roughly about $77.5 \mu S$ (or $12.9 K\Omega$ resistance). On the other hand, if the system has a scattering region, then the reflected current is $R = |r|^2$ and the transmitted current is reduced by a factor $T = |t|^2$. Thus, the current passing through the scatterer to the right lead becomes:

$$\delta I = \frac{2e^2}{\hbar} T \delta V \quad (3.2.7)$$

Taking the voltage difference to the other side yields to

$$G = \frac{\delta I}{\delta V} = \frac{2e^2}{h} T \quad (3.2.8)$$

This is the well-known Landauer formula for a one-dimensional system at zero temperature, connecting the conductance G to the transmission probability T , which is to be evaluated at the Fermi energy [16] of the reservoirs. More generally, at finite temperature, the Landauer formula gives the net current passing from the left electrode L to the right electrode R is given by:

$$I = \frac{2e}{h} \int_{-\infty}^{\infty} dE T(E) [f_L(E) - f_R(E)] \quad (3.2.9)$$

The constants coefficients of the expression above are: $e = -|e|$ is the electronic charge, h is Planck's constant, $T(E)$ is the transmission coefficient for an electron of energy E passing from one lead to the other via the molecule, and Fermi distribution function is giving by

$$f_{L,R}(E) = \frac{1}{e^{-\frac{E-\mu_{L(R)}}{k_B T}} + 1} \quad (3.2.10)$$

Where $\mu_{L,R}$ is the chemical potential of the left and the right reservoir respectively. $k_B = 8.62 \times 10^{-5} \text{eV/k}$ is Boltzmann's constant and T is the temperature. In the case where the voltage V is applied on the left and the right reservoirs symmetrically, then the chemical potentials will be $\mu_L = E_F + \frac{eV}{2}$ and $\mu_R = E_F - \frac{eV}{2}$. Thus, $I = 0$ when $f_L(E) = f_R(E)$, because only the differences in the distributions contribute to the net current.

Therefore, at zero temperature and finite voltage, the current is written by:

$$I = \left(\frac{2e}{h}\right) \int_{E_F - \frac{eV}{2}}^{E_F + \frac{eV}{2}} dE T(E) \quad (3.2.11)$$

Consequently, the conductance $G = I/V$ is calculated by averaging $T(E)$ over an energy window of width ($k_B T = 25 \text{ meV}$ at room temperature) centred on the Fermi energy.

The electrical conductance at zero voltage and the finite temperature limit is:

$$G = \frac{I}{V} = G_0 \int_{-\infty}^{\infty} dE T(E) \left(-\frac{df(E)}{dE} \right)_{\mu=E_F} \quad (3.2.12)$$

G_0 is the quantum of conductance $G_0 = \frac{2e^2}{h}$. Since the quantity $-\frac{df(E)}{dE}$ is a normalised probability distribution of width approximately equal to $k_B T$. Equation 3.2.12 is an integral of a thermal average of the $T(E)$ over an energy window of width $k_B T$.

Finally, the electrical conductance with the combination of two limits (i.e. zero voltage and zero temperature) is

$$G = G_0 T(E) \quad (3.2.13)$$

3.3. Scattering matrix

Calculating the scattering matrix is important for understanding the transmission coefficient appearing in the above formulae. This can be obtained by first examining the solution to the time-independent Schrödinger equation for an electron in the left electrode, which in one dimension takes the form

$$\psi_j = \frac{A}{\sqrt{v_l}} e^{ik_l j} + \frac{B}{\sqrt{v_l}} e^{-ik_l j} \quad (3.3.1)$$

where A and B are the amplitudes of two ingoing and outgoing waves travelling from the left to the right, and v_l is the group velocity in the left electrode. The current per unit energy that this eigenstate carries is:

$$I_{left} = |A^2| - |B^2| \quad (3.3.2)$$

For the right electrode, the solution of the Schrödinger equation system and the corresponding current per unit are given by:

$$\psi_j = \frac{C}{\sqrt{v_r}} e^{ikrj} + \frac{D}{\sqrt{v_r}} e^{-ikrj} \quad (3.3.3)$$

$$I_{right} = |C^2| - |D^2| \quad (3.3.4)$$

where C and D are the amplitudes of the two ingoing and outgoing waves travelling to the right and left, respectively. Since the currents satisfy the relation $I_l = I_r$ (This law of conservation of probability is satisfied by any eigenstate), one obtains

$$|A^2| - |B^2| = |C^2| - |D^2| \quad (3.3.5)$$

Therefore

$$|A^2| + |D^2| = |B^2| + |C^2| \quad (3.3.6)$$

In another words, the incoming current is equal to outgoing current, so the amplitudes in the following wave functions for the left and the right electrode respectively are related to each other:

$$Ae^{ikj} + Be^{-ikj} \quad (3.3.7)$$

$$Ce^{ikj} + De^{-ikj} \quad (3.3.8)$$

This means that there must exist a 2x2matrix connecting the incoming and the outgoing coefficients. This matrix is known as the scattering matrix S (with matrix elements S_{ij}) and satisfies:

$$\begin{bmatrix} B \\ C \end{bmatrix} = \begin{bmatrix} S_{11} & S_{12} \\ S_{21} & S_{22} \end{bmatrix} \begin{bmatrix} A \\ D \end{bmatrix} \quad (3.3.9)$$

i.e.

$$B = S_{11}A + S_{12}D \quad (3.3.10)$$

$$C = S_{21}A + S_{22}D \quad (3.3.11)$$

Since B and C are amplitudes of incoming waves (i.e. plane waves carrying electrons moving towards the scatterer) and A, D are amplitudes of outgoing waves, it is reasonable to write Eq. 3.3.9 in the form $|out\rangle = S|in\rangle$. Since S is independent of the amplitudes A, B, C, D , to achieve further insight into the physical meaning of the matrix elements S_{ij} , it is of interest to consider the following two cases

The first case: $A = 1$ and $D = 0$, and we shall denote the reflected and transmitted amplitudes by $B = r$ and $C = t$. Here r is the amplitude of the reflected wave due to an incoming wave from the left and t is the amplitude of the transmitted wave, then we have

$$\begin{bmatrix} B \\ C \end{bmatrix} = \begin{bmatrix} S_{11} \\ S_{21} \end{bmatrix} \quad (3.3.12)$$

The physical meanings of the symbols S_{11} and S_{21} are therefore the reflection (r) and the transmission (t) respectively, associated with an incident wave from the left.

The second case: $A = 0$ and $D = 1$, then the new matrix is given by

$$\begin{bmatrix} B \\ C \end{bmatrix} = \begin{bmatrix} S_{12} \\ S_{22} \end{bmatrix} \quad (3.3.13)$$

Hence the physical meaning of the symbols S_{12} and S_{22} is the transmission (t') and the reflection (r') amplitudes respectively, associated with an incident wave from the right. In summary, scattering matrix S is represented by the transmission and reflection coefficients as follows.

$$S = \begin{pmatrix} S_{11} & S_{12} \\ S_{21} & S_{22} \end{pmatrix} = \begin{pmatrix} r & t' \\ t & r' \end{pmatrix} \quad (3.3.14)$$

From Eq. 3.3.6,

$$A^*A + D^*D = B^*B + C^*C \quad (3.3.15)$$

Therefore

$$(A^* \ D^*) \begin{pmatrix} A \\ D \end{pmatrix} = (B^* \ C^*) \begin{pmatrix} B \\ C \end{pmatrix} \quad (3.3.16)$$

Then, by substituting Eq. 3.3.16 into 3.3.14, this expressed as

$$(A^* \ D^*) \begin{pmatrix} A \\ D \end{pmatrix} = (A^* \ D^*) S^\dagger S \begin{pmatrix} A \\ D \end{pmatrix} \quad (3.3.17)$$

Since this is satisfied for any A, D , $S^\dagger S$ is the unit matrix and we can write

$$\begin{pmatrix} r^* & t^* \\ t'^* & r'^* \end{pmatrix} \begin{pmatrix} r & t' \\ t & r' \end{pmatrix} = \begin{pmatrix} 1 & 0 \\ 0 & 1 \end{pmatrix} \quad (3.3.18)$$

In terms of scattering theory the important transport properties are obtained as:

$$|r^2| + |t^2| = 1 \Rightarrow R + T = 1 \quad (3.3.19)$$

$$|r'^2| + |t'^2| = 1 \Rightarrow R' + T' = 1 \quad (3.3.20)$$

where the parameters T and R represent the transmission and the reflection coefficients.

3.4. Green's Function

This section presents an attempt to obtain the Green's function of a system, which is an essential tool for reflection and transmission coefficients of different nanoscale structures. This will give a clear outline of the methodology used starting with Green's functions for different nanoscale systems. First, I will discuss the form of the Green's function for a simple one-dimensional discretised lattice (section 3.4.1 and 3.4.2). In the next step, I shall use Dyson's equation to demonstrate how to connect Green's functions of these separable lattices to construct the Green's function of the entire system (section 3.4.3 and 3.4.4).

3.4.1. Green's function of a doubly infinite chain

In this section, I will illustrate the form of the Green's function of the doubly infinite chains with on-site energies (ϵ_0) and hopping parameters ($-\gamma$) as shown in Figure 3.4.1. These chains are described a perfect crystalline chain, which is periodic in the horizontal direction of transport.

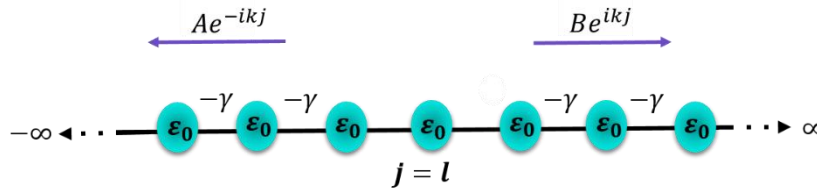


Figure 3.4.1: A simple-tight binding model of a one-dimensional periodic lattice with on-site energies ϵ_0 and couplings $-\gamma$.

The time-independent Schrödinger equation describing the system's wavefunction is:

$$(E - H)|\psi\rangle = 0 \quad (3.4.1)$$

whereas the Green's function of a system described by a Hamiltonian (H) is the solution of:

$$(E - H)G = I \quad (3.4.2)$$

For a finite system, where H is a finite matrix, the formal solution to this equation is given by:

$$G = (E - H)^{-1} \quad (3.4.3)$$

Physically, the term G is the retarded Green's function (g_{jl}), which describes the system response at point j to source l

$$(E - H)g_{jl} = \delta_{jl} \quad (3.4.4)$$

δ_{jl} is named Kronecker delta, which is equal to 1 if $j = l$ and zero otherwise. The Green's function for a doubly infinite system can be written as

$$\varepsilon_0 g_{jl} - \gamma g_{j+1,l} - \gamma g_{j-1,l} + \delta_{jl} = E g_{jl} \quad (3.4.5)$$

The solution can be presented simply as:

$$g_{jl} = \begin{cases} Ae^{ikj} & j \geq l \\ Be^{-ikj} & j \leq l \end{cases} \quad (3.4.6)$$

The parameters A and B are arbitrary constants and represent the amplitudes of the two waves coming from the left and right respectively. This solution satisfies Eq. 3.4.5 at the point $j = l$, and then the Green's function must be continuous at the same point.

$$g_{jl}|_{j=l} = \begin{cases} Ae^{ikj} & A = \alpha e^{-ikl} \\ Be^{-ikj} & B = \alpha e^{ikl} \end{cases} \quad (3.4.7)$$

Therefore, substituting Eq. 3.4.7 to Eq. 3.4.5 yields:

$$(\varepsilon_0 - E)\alpha - \gamma\alpha e^{ik} - \gamma\alpha e^{ik} = -1 \quad (3.4.8)$$

$$\gamma\alpha(2\cos k - 2e^{ik}) = -1 \quad (3.4.9)$$

$$\alpha = \frac{1}{2i\gamma\sin k} \quad (3.4.10)$$

$$\alpha = \frac{1}{i\hbar v} \quad (3.4.11)$$

where v is the group velocity and $\hbar v(E) = 2\gamma \sin k(E)$. Now I combine both results from Eq. 3.4.11 and Eq. 3.4.7 to get the Green's function for the double infinite chain[5][6]

$$g_{jl}^{\infty} = \frac{e^{ik|l-j|}}{i\hbar v} \quad (3.4.12)$$

Here, g_{jl}^{∞} represents the retarded Green's function, which describes the two outgoing waves from the source $j=l$, as shown in Figure 3.4.1.

3.4.2. Green's function of a semi-infinite one-dimensional chain

In this section, the aim is to derive the Green's function of a semi-infinite chain, by considering the problem of a doubly infinite chain, and introducing an appropriate boundary condition in order to obtain the Green's function for the semi-infinite chain as shown in Figure 3.4.2

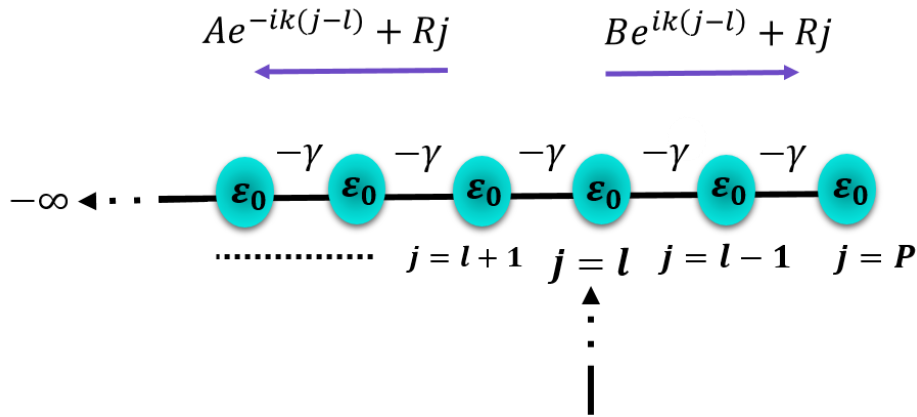


Figure 3.4.2: A semi-infinite linear chain with on-site energies ϵ_0 and couplings $-\gamma$, which terminates at site P .

This infinite chain must terminate at a given site P , which means the Green's function is eliminated at the site $P+1$ and all points $P+1 \geq P$ are missing lead to the boundary condition $\psi_{P+1}^l = 0$. This is achieved by adding a wavefunction to the Green's function of the

doubly infinite Green's function. R_j is the reflected wave $R_j = Ae^{-ikj}$. Consequently, the general Green's function at G_{P+1} is written as:

$$G_{P+1} = \frac{e^{ik(P+1-l)}}{i\hbar v} + Ae^{-ik(P+1)} = 0 \quad (3.4.13)$$

This yields:

$$A = -e^{ik[2(P+1)-l]} \quad (3.4.14)$$

Hence the general retarded Green's function of the semi-infinite linear chain is

$$g_{jl} = \frac{e^{ik|j-l|} - e^{-ikj(j+l)}e^{ik(2(P+1))}}{i\hbar v} \quad (3.4.15)$$

This satisfies $\psi_{P+1}^l = 0$ and $\psi_j^{P+1} = 0$.

$g_{P+1,l} = \frac{e^{ik|(P+1)-l} - e^{-ikj(P+1)}e^{-ikl}}{i\hbar v} = 0$, because the absolute value will vanish as the Green's function is vanished at site P .

The Green's function terminated at point (P) due to source at (l) is:

$$g_{jl} = \frac{e^{ik|j-l|} - e^{-ikj(j+l)}e^{ik(2(P+1))}}{i\hbar v} \quad (3.4.16)$$

From the boundary condition where $l = P$ therefore:

$$g_{PP} = \frac{1 - e^{2ik}}{i2\gamma \sin k} = \frac{e^{ik}(e^{-ik} - e^{ik})}{i2\gamma \sin k} \quad (3.4.17)$$

where $(e^{-ik} - e^{ik}) = i2\sin k$ will cancel with the dominator. This shows that the Green's function on terminal site P is

$$g_{p,p} = -\frac{e^{ik}}{\gamma} \quad (3.4.18)$$

which is known as the 'surface Green's function' of a semi-infinite chain.

3.4.3. One-dimensional scattering system

In this section, the aim is to obtain the entire Green's function for a system which includes two one-dimensional tight binding semi-infinite leads connected by a coupling element ($-\alpha$). Both leads have equal on-site energy (ε_0) and hopping elements ($-\gamma$), as shown in Figure 3.4.3.

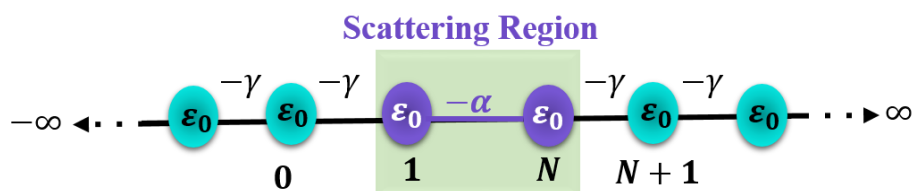


Figure 3.4.3: A simple tight-binding model of a one-dimensional scattering region attached to one-dimensional leads.

The Hamiltonian of this infinite system takes the form of an infinite matrix as:

$$\begin{pmatrix} \ddots & -\gamma & 0 & 0 & 0 & 0 \\ -\gamma & \varepsilon_0 & -\gamma & 0 & 0 & 0 \\ 0 & -\gamma & \varepsilon_0 & \alpha & 0 & 0 \\ 0 & 0 & \alpha & \varepsilon_0 & -\gamma & 0 \\ 0 & 0 & 0 & -\gamma & \varepsilon_0 & -\gamma \\ 0 & 0 & 0 & 0 & -\gamma & \ddots \end{pmatrix} = \begin{pmatrix} H_L & V_c \\ V_c^\dagger & H_R \end{pmatrix} \quad (3.4.19)$$

In this matrix, H_L and H_R are the Hamiltonians for the left lead and right leads, and V_c is the coupling to connect these leads. Therefore, to calculate the Green's function of this problem, we cannot solve the following equation directly

$$G = (E - H)^{-1} \quad (3.4.20)$$

However in the case of two decoupled leads ($\alpha = 0$), the Green's function on the terminal sites of the two semi-infinite leads will simply be given by the decoupled Green's function g

$$g = \begin{pmatrix} \frac{-e^{ik}}{\gamma} & 0 \\ 0 & \frac{-e^{ik}}{\gamma} \end{pmatrix} = \begin{pmatrix} g_L & 0 \\ 0 & g_R \end{pmatrix} \quad (3.4.21)$$

If we now switch on the interaction, the Green's function for the coupled leads of this system can be obtained using Dyson's equation, which is written as:

$$G = (g^{-1} - V)^{-1} \quad (3.4.22)$$

Clearly, the operator V describing the interaction connecting the two leads will have the form:

$$V = \begin{pmatrix} 0 & \alpha \\ \alpha & 0 \end{pmatrix} \quad (3.4.23)$$

Then, the solution of the Green's function of this system is given by solving Dyson's equation

$$G = \frac{1}{\gamma^2 e^{-2ik} - \alpha^2} \begin{pmatrix} \gamma e^{-ik} & -\alpha \\ -\alpha & \gamma e^{-ik} \end{pmatrix} \quad (3.4.24)$$

After finding Green's function for this system, the only remaining step is to calculate the transmission (\vec{t}) and reflection (\vec{r}) amplitudes, which can be obtained by using the Fisher-Lee relation. This relates the scattering amplitudes of a scattering problem to Green's function of the problem. The Fisher-Lee relations is given by:

$$r = i\hbar v G_{0,0} - 1 \quad (3.4.25)$$

$$t = i\hbar v G_{0,N+1} e^{ik} \quad (3.4.26)$$

These coefficients amplitudes correspond to particles incident from the left, and the same procedure could be used in order to compute these coefficients for the particles are travelling from the right. Based on these coefficients the probability is defined as:

The solution to the Schrodinger equation for $j = N + 1, N + 2, \dots, \infty$, will be labelled ϕ_j and the eigenstate in the right chain is:

$$\phi_j = \frac{1}{\sqrt{v_R}} [te^{ik_R j}] \quad (3.4.30)$$

The parameters in Eq. 3.4.29 and 3.4.30 r and t are the reflection and transmission amplitudes, where v_L and v_R are the group velocity of the left and right leads respectively. The scattering region is labelled as f_j where $j = 1, 2, \dots, N$. Using these notations, the Schrödinger equation in these regions takes the form as

For $j = -1, -2, \dots, -\infty$:

$$\varepsilon_L \psi_j - \gamma_L \psi_{j-1} - \gamma_L \psi_{j+1} = E \psi_j \quad (3.4.31)$$

For $j = 0$

$$\varepsilon_L \psi_0 - \gamma_L \psi_{-1} - \alpha f_1 = E \psi_0 \quad (3.4.32)$$

For scattering region: for $j = 1$

$$\sum_{l=1}^N H_{1l} f_l - \alpha \psi_0 = E f_1 \quad (3.4.33)$$

For $j = 2, 3, \dots, N - 1$

$$\sum_{l=1}^N H_{jl} - f_l = E f_j \quad (3.4.34)$$

For $j = N$

$$\sum_{l=1}^N H_{Nl} - \beta \phi_{N+1} = E f_N \quad (3.4.35)$$

Here, H_{NI} is a matrix element for Hamiltonian describing the scattering region shown in Figure 3.4.4.

The case of the right lead for $j = N + 1$

$$\varepsilon_R \phi_{N+1} - \beta f_N - \gamma_R \phi_{N+2} = E \phi_{N+1} \quad (3.4.36)$$

For $j \geq N + 2, \dots, \infty$

$$\varepsilon_R \phi_j - \gamma_R \phi_{j-1} - \gamma_R \phi_{j+1} = E \phi_j \quad (3.4.37)$$

Substituting Eq. 3.4.29 into Eq. 3.4.31 and Eq. 3.4.32 yields (the dispersion relation in the left lead)

$$E(k) = \varepsilon_L - 2\gamma_L \cos k_L$$

and (3.4.38)

$$\alpha f_1 = \gamma_L \psi_1$$

Similarly, substituting Eq. 3.4.37 into Eq. 3.4.34 and Eq. 3.4.35 yields (the dispersion relation in the right lead)

$$E(k) = \varepsilon_R - 2\gamma_R \cos k_R$$

and (3.4.39)

$$\beta f_N = \gamma_R \phi_N$$

The key parameters in Eq. 3.4.38 and Eq. 3.4.39 are $E(k)$ tells that the eigenstates in the left and right leads are not equal (i.e. non-symmetric junction), where f_1 and f_N represent the relation between the wave function on the inside of the scattering region to the wave function on the outside (i.e. ψ_1 and ϕ_N). γ_L and γ_R are the hopping elements for the left and right electrodes respectively. Note that Eq. 3.4.33 and Eq. 3.4.35 can be written as the

form $(E - h) |f\rangle = |S\rangle$, where h is the $N \times N$ Hamiltonian of the scattering region and $|f\rangle, |S\rangle$ will take the form

$$|f\rangle = \begin{bmatrix} f_1 \\ \vdots \\ f_j \\ \vdots \\ f_N \end{bmatrix}, \quad |S\rangle = \begin{bmatrix} -\alpha\psi_0 \\ 0 \\ \vdots \\ 0 \\ -\beta\phi_{N+1} \end{bmatrix}, \quad h = \begin{bmatrix} h_{11} & \cdots & h_{1N} \\ \vdots & \ddots & \vdots \\ h_{N1} & \cdots & h_{NN} \end{bmatrix}$$

Then multiplying $(E - h) |f\rangle = |S\rangle$ by the inverse matrix $(E - h)^{-1}$ yields $|f\rangle = g|S\rangle$, and takes the form

$$\begin{aligned} \begin{bmatrix} f_1 \\ \vdots \\ f_j \\ \vdots \\ f_N \end{bmatrix} &= \begin{bmatrix} g_{11} & \cdots & g_{1N} \\ \vdots & \ddots & \vdots \\ g_{N1} & \cdots & g_{NN} \end{bmatrix} \begin{bmatrix} -\alpha\psi_0 \\ 0 \\ \vdots \\ 0 \\ -\beta\phi_{N+1} \end{bmatrix} \\ \Rightarrow \begin{pmatrix} f_1 \\ f_N \end{pmatrix} &= \begin{pmatrix} g_{11} & g_{1N} \\ g_{N1} & g_{NN} \end{pmatrix} \begin{pmatrix} -\alpha\psi_0 \\ -\beta\phi_{N+1} \end{pmatrix} \\ \Rightarrow \begin{pmatrix} f_1 \\ f_N \end{pmatrix} &= \tilde{g} \begin{pmatrix} -\alpha\psi_0 \\ -\beta\phi_{N+1} \end{pmatrix} \end{aligned} \tag{3.4.40}$$

This yields,

$$[\tilde{g}]^{-1} \begin{pmatrix} f_1 \\ f_N \end{pmatrix} = \begin{pmatrix} -\alpha\psi_0 \\ -\beta\phi_{N+1} \end{pmatrix} \tag{3.4.41}$$

where $[\tilde{g}]^{-1}$ the inverse of the 2×2 sub matrix of the Green's function is

$$[\tilde{g}]^{-1} = \begin{pmatrix} g_{11} & g_{1N} \\ g_{N1} & g_{NN} \end{pmatrix}^{-1} = \frac{1}{d} \begin{pmatrix} g_{NN} & -g_{1N} \\ -g_{N1} & g_{11} \end{pmatrix} \tag{3.4.42}$$

where $d = \det \tilde{g} = g_{11}g_{22} - g_{1N}g_{NN}$. It is worth mentioning that, Eq. 3.4.38 and Eq. 3.4.39 relate the inside f_1 and f_N to the outside ψ_1 and ϕ_N , this yields $\psi_1 = \frac{\alpha}{\gamma_L} f_1$ and $\phi_N = \frac{\beta}{\gamma_R} f_1$. Our task is to solve these for $\begin{pmatrix} f_1 \\ f_N \end{pmatrix}$ and $\begin{pmatrix} \psi_1 \\ \phi_N \end{pmatrix}$. To achieve this we need ψ_1 to ψ_0 and ϕ_N to ϕ_{N+1} . Therefore, it takes the following form

$$\psi_1 = \frac{1}{\sqrt{v_L}} [2i \sin k_L] + \psi_0 e^{-ik_L} \quad (3.4.43)$$

$$\phi_N = \phi_{N+1} e^{-ik_R}$$

Hence

$$\begin{pmatrix} -\alpha\psi_0 \\ -\beta\phi_{N+1} \end{pmatrix} = \begin{pmatrix} \Sigma_L & 0 \\ 0 & \Sigma_R \end{pmatrix} \begin{pmatrix} f_1 \\ f_N \end{pmatrix} + \begin{pmatrix} \frac{\alpha e^{ik_L} [2i \sin k_L]}{\sqrt{v_L}} \\ 0 \end{pmatrix} \quad (3.4.44)$$

$$\Rightarrow \begin{pmatrix} -\alpha\psi_0 \\ -\beta\phi_{N+1} \end{pmatrix} = \begin{pmatrix} \Sigma_L f_1 \\ \Sigma_R f_N \end{pmatrix} + \begin{pmatrix} \frac{\alpha e^{ik_L} [2i \sin k_L]}{\sqrt{v_L}} \\ 0 \end{pmatrix}$$

Where the self-energies to the left and right leads are $\Sigma_L = \frac{-\alpha^2 e^{ik_L}}{\sqrt{v_L}}$ and $\Sigma_R = \frac{-\beta^2 e^{ik_R}}{\sqrt{v_R}}$, respectively. Then, substituting the self-energies into 3.4.41, this yields

$$([\tilde{g}]^{-1} - \Sigma) \begin{pmatrix} f_1 \\ f_N \end{pmatrix} = \begin{pmatrix} \frac{\alpha e^{ik_L} [2i \sin k_L]}{\sqrt{v_L}} \\ 0 \end{pmatrix} \quad (3.4.45)$$

$$\Rightarrow \Sigma = \begin{pmatrix} \Sigma_L & 0 \\ 0 & \Sigma_R \end{pmatrix}$$

Where Σ is 2×2 matrix of the self-energies to the left and right leads.

$$\begin{pmatrix} f_1 \\ f_N \end{pmatrix} = G \begin{pmatrix} \frac{\alpha e^{ik_L} [2i \sin k_L]}{\sqrt{v_L}} \\ 0 \end{pmatrix}; G = ([\tilde{g}]^{-1} - \Sigma)^{-1}; G = \begin{pmatrix} G_{11} & G_{1N} \\ G_{N1} & G_{NN} \end{pmatrix} \quad (3.4.46)$$

Hence

$$f_N = G_{N1} \frac{\alpha e^{ik_L} [2i \sin k_L]}{\sqrt{v_L}} \quad (3.4.47)$$

$$\phi_N = \frac{\beta}{\gamma_R} f_1 = G_{N1} \frac{\alpha \beta e^{ik_L} [2i \sin k_L]}{\gamma_R \sqrt{v_L}}$$

Since $\phi_N = \frac{1}{\sqrt{v_R}} [t e^{ik_{RN}}]$, then the transmission (t) could be obtained as:

$$t = G_{N1} \frac{\alpha\beta e^{ik_L} [2i \sin k_L]}{\gamma_R \sqrt{v_L}} \times \sqrt{v_R} e^{-ik_R N} \quad (3.4.48)$$

Since $\hbar v_R = 2\gamma_R \sin k_R$ and $\hbar v_L = 2\gamma_L \sin k_L$, this yields

$$t = iG_{N1} \alpha\beta e^{ik_L} \sqrt{\frac{2\sin k_L}{\gamma_L}} \sqrt{\frac{2\sin k_R}{\gamma_R}} e^{-ik_R N} \quad (3.4.49)$$

The transmission probability is $T(E) = |t|^2$ which could be written as:

$$T = |t|^2 = 4 \left[\frac{\alpha^2 \sin k_L}{\gamma_L} \right] \left[\frac{\beta^2 \sin k_R}{\gamma_R} \right] |G_{N1}|^2 \quad (3.4.50)$$

Equivalently in term of g

$$T = |t|^2 = 4 \underbrace{\left[\frac{\alpha^2 \sin k_L}{\gamma_L} \right]}_{\Gamma_L} \underbrace{\left[\frac{g_{N1}}{\Delta} \right]^2}_{ML} \underbrace{\left[\frac{\beta^2 \sin k_R}{\gamma_R} \right]}_{\Gamma_R} \quad (3.4.51)$$

The term Δ is giving by:

$$\Delta = 1 - g_{11}\Sigma_L - g_{NN}\Sigma_R + \Sigma_L\Sigma_R(g_{11}g_{NN} - g_{1N}g_{N1})$$

The expression above is the most general solution to calculate the transmission probability for any scattering region connected to identical electrodes. Γ_L is a property of the left lead; Γ_R is a property of the right lead; ML is determined by both the molecule and the electrodes. The completely general technique for calculating Green's function and a scattering S matrix and transport coefficient of a finite superlattice connected to crystalline semi-infinite leads can be found in [16]

3.5. The transmission curve features

The main feature of electron transport through single molecules is quantum interference, which is a fundamental quantum phenomenon. Multiple paths for transferring electrons across the junction exist in certain molecules, and these channels can lead to a few key features we might expect to see in the more complicated transport curves of real systems such as resonances or anti-resonances. Thus, a deep understanding of the transmission can be achieved by looking at the properties of these resonances. This section aims to briefly discuss different kinds of resonances, for instance: Breit-Wigner resonances[7], anti-resonances [8][9], and Fano resonances due to quantum interference [10].

3.5.1. Breit-Wigner resonance

The Breit-Wigner formula is the simplest feature to understand the behaviour of resonance in the transmission coefficient $T(E)$, which is named a Lorentzian peak. This occurs when the energy of the incident electron resonates with an energy level of the isolated system. For isolated system contains N sites as shown in Figure 3.5.1, the Schrödinger equation is $H|\psi_n\rangle = E_n|\psi_n\rangle$, where the eigenstates $|\psi_n\rangle$ satisfy such properties: the completeness condition $\sum_{n=1}^N |\psi_n\rangle\langle\psi_n| = I$ and $\langle\psi_n|\psi_m\rangle = \delta_{nm}$.

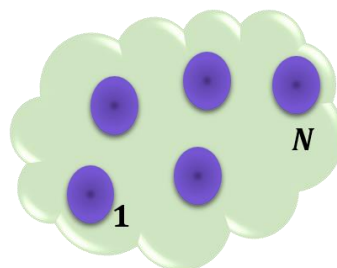


Figure 3.5.1: A simple model of an arbitrarily scattering region of System N sites.

To perform such an equation of Green's function, it was necessary to start from Eq. 3.4.20 using the completeness condition as follows

$$g = (E - H)^{-1} = \sum_{n=1}^N (E - H)^{-1} |\psi_n\rangle\langle\psi_n| \quad (3.5.1)$$

Then, using the fact that the function of H acting on an eigenvector yields the same function of the corresponding eigenvalue, thus Eq. 3.5.1 becomes

$$g = (E - H)^{-1} = \sum_{n=1}^N \frac{|\psi_n\rangle\langle\psi_n|}{E - E_n} \quad (3.5.2)$$

If $E \approx \lambda$, where λ is a nondegenerate eigenvalue of the Hamiltonian, the Green's function is approximately

$$g(E) = \frac{|\psi_\lambda\rangle\langle\psi_\lambda|}{E - \lambda} = \begin{pmatrix} g_{11} & \cdots & g_{1N} \\ \vdots & \vdots & \vdots \\ g_{N1} & \cdots & g_{NN} \end{pmatrix} \quad (3.5.3)$$

where $|\psi_\lambda\rangle$ is the corresponding eigenstates written as

$$|\psi_\lambda\rangle = \begin{pmatrix} \psi_1^\lambda \\ \psi_2^\lambda \\ \vdots \\ \psi_N^\lambda \end{pmatrix} \quad (3.5.4)$$

Then we can obtain the elements of Green's function as below

$$\begin{aligned} g_{11} &= \frac{|\psi_1^\lambda|^2}{E - \lambda} ; g_{NN} = \frac{|\psi_N^\lambda|^2}{E - \lambda} \\ g_{1N} &= \frac{\psi_1^\lambda \psi_N^*}{E - \lambda} ; g_{N1} = \frac{\psi_N^\lambda \psi_1^*}{E - \lambda} \end{aligned} \quad (3.5.5)$$

Form Eq. 3.4.51 the term Δ is $\Delta = 1 - g_{11}\Sigma_L - g_{NN}\Sigma_R + \Sigma_L\Sigma_R(g_{11}g_{NN} - g_{1N}g_{N1})$. So, we have $g_{11}g_{NN} = g_{1N}g_{N1}$, this leads to $\Delta = 1 - g_{11}\Sigma_L - g_{NN}\Sigma_R$. Therefore, it is assumed that $g_{11}\Sigma_L - g_{NN}\Sigma_R = \frac{\psi_1^2\Sigma_L - \psi_N^2\Sigma_R}{E - \lambda}$ thus

$$\Delta = 1 - \frac{\psi_1^2\Sigma_L}{E - \lambda} - \frac{\psi_N^2\Sigma_R}{E - \lambda} \quad (3.5.6)$$

By substituting Eq. 3.5.6 in terms in Eq. 3.4.51 yields

$$T = 4\Gamma_L\Gamma_R \left[\frac{\psi_1^2\psi_N^2}{(E - \lambda)^2} \right] \frac{1}{\left| 1 - \frac{\psi_1^2\Sigma_L}{E - \lambda} - \frac{\psi_N^2\Sigma_R}{E - \lambda} \right|^2}$$

$$T = \frac{4(\Gamma_L\psi_1^2)(\Gamma_R\psi_N^2)}{|(E - \lambda) - \psi_1^2\Sigma_L - \psi_N^2\Sigma_R|^2} \quad (3.5.7)$$

$$T = \frac{4\Gamma_L\Gamma_R}{(E - \lambda - \sigma_L - \sigma_R)^2 + (\Gamma_L + \Gamma_R)^2}$$

Where Γ_L and Γ_R correspond to the real and imaginary parts of the self-energy $\Sigma_L = \sigma_L - i\Gamma_L$; $\Sigma_R = \sigma_R - i\Gamma_R$, and the key parameters in Eq.3.5.7 are giving by

- Γ_L is related to the left lead

$$\Gamma_L = \frac{\alpha^2}{\gamma_L} \sin k_L |\psi_1|^2, \quad \sigma_L = -\frac{\alpha^2}{\gamma_L} \cos k_L |\psi_1|^2$$
- Γ_R is related to the right lead

$$\Gamma_R = \frac{\beta^2}{\gamma_R} \sin k_R |\psi_1|^2, \quad \sigma_R = -\frac{\beta^2}{\gamma_R} \cos k_R |\psi_N|^2$$

Therefore, the transmission coefficient is given by

$$T(E) = \frac{4\Gamma_L\Gamma_R}{(E - \varepsilon_n)^2 + (\Gamma_L + \Gamma_R)^2} \quad (3.5.8)$$

where Γ_L and Γ_R represent the coupling of the molecular orbital to the electrode, E represents the energy of an electron passing through the molecular system. The term ε_n is given by ($\varepsilon_n =$

$\lambda - \sigma$) where λ is defined by the eigen-energy of the molecular orbital shifted slightly by the real part of the self-energy ($\sigma = \sigma_L - \sigma_R$) which is the coupling of the orbitals to the electrodes.

A number of factors in this formula influence the transmission coefficient as the following:

1. If $\Gamma_L = \Gamma_R$ then $T(E) = 1$ on-resonance will be at the maximum 1.
2. If $\Gamma = \Gamma_L + \Gamma_R$ this width of the resonances is much less than the level spacing of the isolated molecule then the Breit-Wigner formula is valid.
3. If $\Gamma_L \ll \Gamma_R$ then the transmission coefficient on-resonance is approximately equal to $(4\Gamma_L)/\Gamma_R$, that leads to $T(E) \ll 1$.

3.5.2. Anti-resonances

An anti-resonance is another important feature in the transmission probability. It appears when the energy of the incident electron E coincides with the eigenenergy E_n of one of the two electrodes as a simple example shown in Figure 3.5.2. The destructive interference occurs between propagating waves at the nodal point.

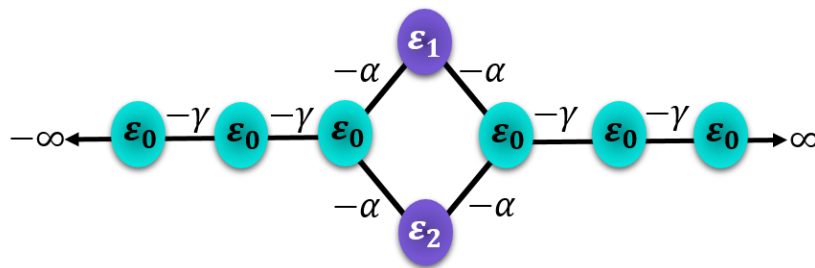


Figure 3.5.2: A simple tight-binding model of anti-resonance, when two semi-finite one-dimensional chains are coupled to the scattering region.

Two one-dimensional semi-infinite crystalline chains with site energies ϵ_0 and hopping elements $-\gamma$ are coupled to two non-interacting scattering regions with site energies ϵ_1 and ϵ_2 by the hopping parameter $-\alpha$. The curve in the Figure 3.5.3 shows the analytical transmission probability for this system.

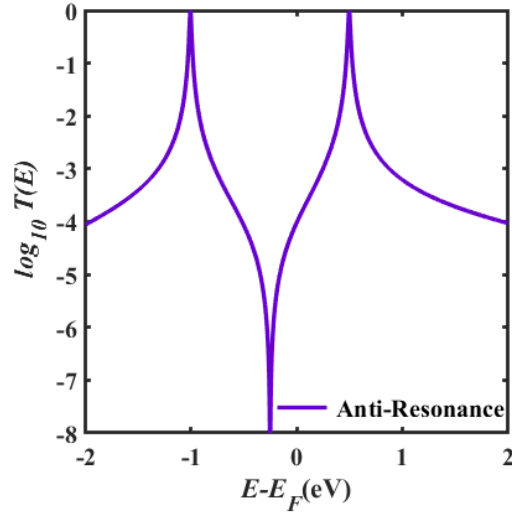


Figure 3.5.3: **Transmission coefficient for the system described in Figure 3.5.2**, ($\varepsilon_0 = 0$, $\varepsilon_{1,2} = -0.5$, $\gamma = -2$ and $\alpha = -0.1$).

3.5.3. Fano resonance

Fano-resonance is a type of resonant scattering phenomenon, due to the interference between scattering with a discrete state (i.e. a side group), which is weakly coupled within a continuum state, and this produces an asymmetric peak. This Fano-resonance feature occurs when a side group is connected to the central backbone by a weak coupling (α), which is considered to be weaker than the coupling to the open system Γ_L and Γ_R as shown in Figure 3.5.4. It is worth remembering that, the width of a Fano-resonance becomes narrow by varying the (α) coupling.

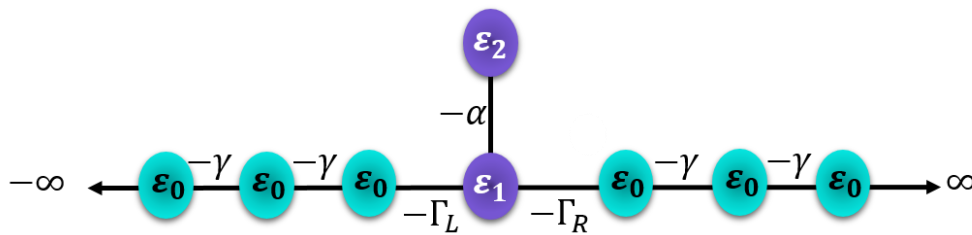


Figure 3.5.4: **A simple tight-binding model of Fano-resonance**, when two semi-finite one-dimensional chains are coupled to the scattering region of site energy ε_1 by hopping bond Γ_L and Γ_R . Then the scattering region is coupled to the extra energy level ε_2 by the hopping bond $-\alpha$.

Thereafter, the transmission coefficient can be calculated by using the following formula

$$T(E) = \frac{4\Gamma_L\Gamma_R}{(E - \varepsilon_n)^2 + (\Gamma_L + \Gamma_R)^2} \quad (3.5.9)$$

Here $\varepsilon_n = \varepsilon_1 + \frac{\alpha^2}{E - \varepsilon_2}$, from the dominator, if $E - \varepsilon_n = 0$, then there are two solutions: the first is when $E = \varepsilon_1$, then the Breit-Wigner occurs. The second one is when $E = \varepsilon_2$, the ε_n in Eq.3.5.9 diverges and the electron transmission will be destroyed, this produces an anti-resonance as shown in Figure 3.5.5, which by the superposition of quantum mechanics if there are two states combined then a Fano resonance curve will occur[11][12]. Fano resonances have been demonstrated to be tuneable via the molecular side groups[10], gate voltages[13] and to give interesting thermoelectric properties[14].

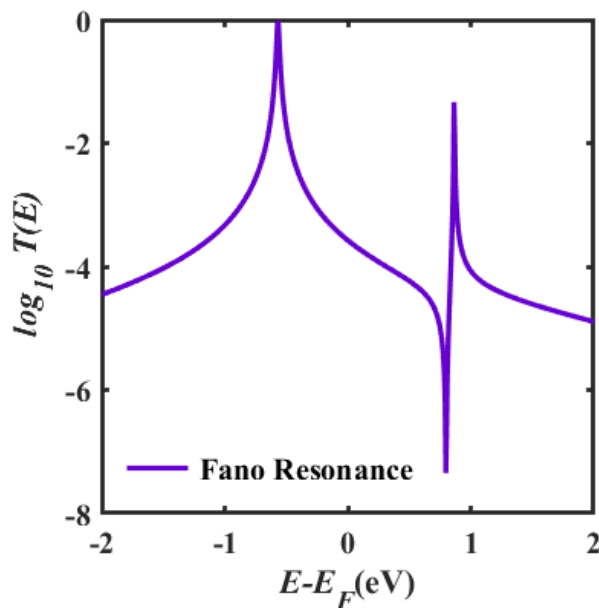


Figure 3.5.5: **Transmission coefficient for the system describes in Figure 3.5.4**, ($\varepsilon_0 = 0$, $\varepsilon_1 = -0.5$, $\varepsilon_2 = 0.8$, $\gamma = -2$, $\Gamma_{L,R} = -0.1$, and $\alpha = -0.3$).

3.6. Magic Number theory

In molecular electronic transport, theoretical analysis plays a significant role in understanding their generic behaviour, which is potentially common to all molecules. An example in section 3.5 is on-resonance constructive interference which is captured by the Breit-Wigner formula, which occurs when the energy E of an electron passing through a molecule is close to an energy level of the molecule. At voltages and temperatures encountered in real experiments, E is close to the Fermi energy E_F of the electrodes. Typically, E_F is usually located within the HOMO-LUMO (H-L) gap, where the Breit-Wigner formula is not valid. Instead, transport takes place via off-resonance, phase-coherent co-tunnelling. In this case, there is a useful conceptual approach which is recently developed in ref [16] known as mid-gap theory or alternatively magic number theory (because this theory is simple and seems like magic which can predict the conductance ratio). This leads to a magic ratio rule (MRR), which is an exact formula for conductance ratios of tight-binding representations of molecules that are weakly coupled to electrodes when the Fermi energy E_F of electrodes is located at the centre of the H-L gap [16]. I shall demonstrate the MRR for graphene-like aromatic molecules such as Benzene, which has 6-membered atoms. This means that E_F of the gold electrode lies between the H-L gap, in this case, x can be neglected and Δ is equal to 1 in Eq. 3.4.50, Then the transmission is $T = 4\Gamma_L\Gamma_R|g_{N1}|^2$. Considering $\Gamma_L\Gamma_R$ to be random variable labelled as R, then the electrical conductance G_{ij} of molecule A with connectivity i, j can be written as:

$$G_{ij} = R[g_{ij}(E_F)]^2 \quad (3.6.1)$$

where $g_{ij}(E_F)$ is the Green's function of the isolated central region. All information on the electrode shape and the coupling between the anchor and the gold electrodes are ignored since our focus here is to find the Green's function of the core. By taking the logarithm of Eq. 3.6.1, this yields

$$\log G_{ij} = \log R + \log [g_{ij}(E_F)]^2 \quad (3.6.2)$$

The equation above shows the most probable value of logarithmic conductance from the probability distribution is the most probable value of the constant random value $\log R$ plus the non-random of $[g_{ij}(E_F)]^2$. According to several random measurements the statistical properties of R do not depend on connectivity, then the electrical conductance $G_{i'j'}$ of a molecule B with connectivity i', j' is

$$\log G_{i'j'} = \log R + \log [g_{i'j'}(E_F)]^2 \quad (3.6.3)$$

Subtracting equations 3.6.2 and 3.6.3, the most-probable conductance yields

$$\log G_{ij} - \log G_{i'j'} = \log [g_{ij}(E_F)]^2 - \log [g_{i'j'}(E_F)]^2 \quad (3.6.4)$$

Using the fact that $\log G_{ij} - \log G_{i'j'} = \log \frac{G_{ij}}{G_{i'j'}}$. Consequently, the most probable conductance of molecule core corresponding to different connectivity to the electrode given by

$$\frac{G_{ij}}{G_{i'j'}} = \frac{[g_{ij}(E_F)]^2}{[g_{i'j'}(E_F)]^2} \quad (3.6.5)$$

This universal concept states that the most-probable conductance ratio of two molecules is equal to the square of the ratio of their magic integers corresponding to different connectivities. As this ratio does not depend on details of the electrodes or anchor groups (i.e. how the molecule is coupled to the electrodes) then the constant R is cancelled, this helps to get rid of inherent errors from the DFT calculation. Now find the Hamiltonian in a unit of γ relative to ε to demonstrate g_{ij} which the Green's function of the isolated molecule is [16].

$$g_{ij} = (EI - h)^{-1}$$

To obtain the M-table for a given lattice, first construct the connectivity table $C = -h$, which tells us how the atoms i and j are connected by placing a (1) when two sites are connected and

zero otherwise. Then the corresponding M-table can be defined to be the transpose of the cofactor matrix of C-table multiplying by the determinant d (Note that $MC = I$, where I is the unit matrix). In the case of H-L gap transport $E_F = 0$, then the magic number table for benzene is going to be $M(E_F) = (EI - h)^{-1} = C^{-1}$. For these bipartite lattices, zero-energy M-table $M(0)$ is block off-diagonal of the form

$$M = \begin{pmatrix} 0 & \bar{M}^t \\ \bar{M} & 0 \end{pmatrix}$$

where $(\bar{M} = \det(C) \times [C^t]^{-1})$ is a table of integers. The presence of the zero in the above expression means that magic number theory predicts that when odd-numbered sites are connected to odd-numbered sites or even-numbered sites are connected to even-numbered sites (ie for meta connectivities), the conductance is zero.

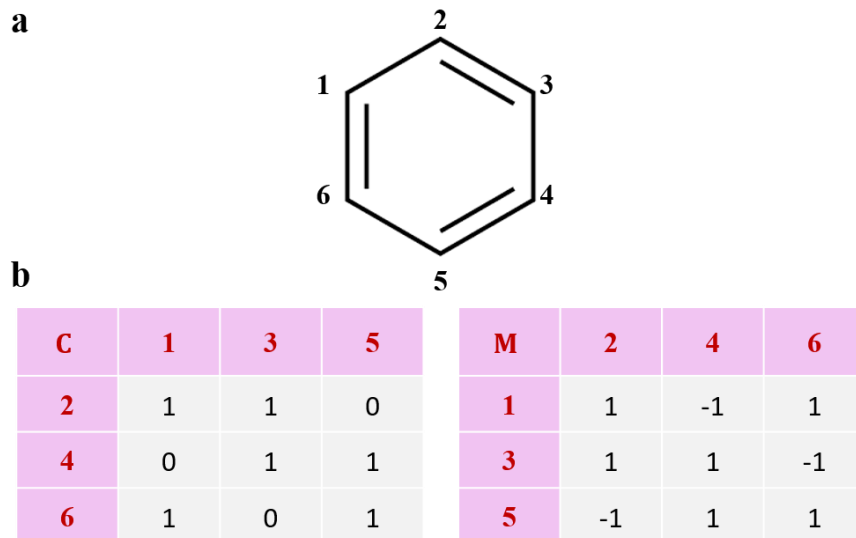


Figure 3.6.1. **Example of bipartite lattices.** (a) represents benzene; (b-c) are the C-table and the M-tables of magic integers for benzene.

In the diagram above, I consider a ring of N sites such as benzene molecule, labelled by integers, which increase sequentially in a clockwise direction, then by applying Eq. 3.6.5 the mid-gap conductance for connectivities $G_{1,2}$ and $G_{1,4}$ in Figure 3.6.1 are predicted to satisfy

$$\frac{G_{1,2}}{G_{1,4}} = \frac{1^2}{(-1)^2} = 1$$

In other words, magic ratio theory predicts that ortho and para connectivities yield the same conductances. Magic ratio theory is a theory of transport through the pi system of polyaromatic hydrocarbons and therefore deviation from the results would indicate that transport through the sigma system is non-negligible, or some other unexpected feature is present in the experiment.

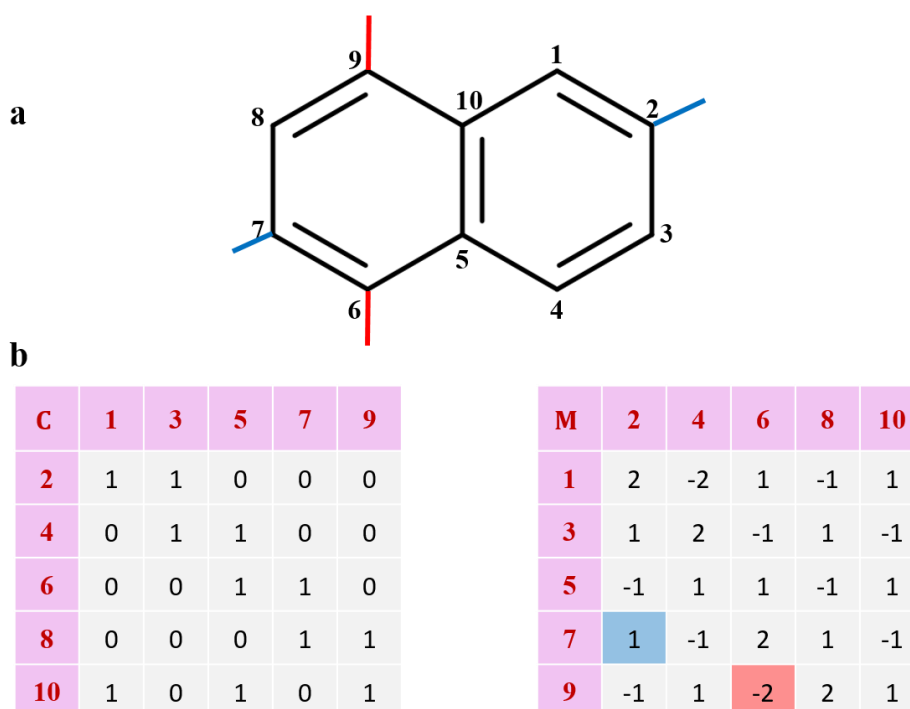


Figure 3.6.2. **Example of bipartite lattices.** (a) represents Naphthalene; (b-c) are the C-table and the M-tables of magic integers for Naphthalene.

Another example of applying the magic ratio theory to a bipartite lattice (a naphthalene core) consisting of ten atoms labelled by integers, which increase sequentially in a clockwise direction. To apply this theory, two connectivities are required, thus $G_{9,6}$ and $G_{7,2}$ are chosen as shown in Figure 3.6.2.

$$\frac{G_{9,6}}{G_{7,2}} = \frac{(-2)^2}{1^2} = 2$$

From the magic number tables above, the theory of a conductance ratio can be gained; para conductance is high (odd-numbered sites are connected to even-numbered sites), whereas meta conductance (odd-numbered sites are connected to odd-numbered sites or even-numbered sites are connected to even-numbered sites) is low (i.e. zero).

3.7. Green function and frontier molecular orbitals

Figure 3.7.1 shows the molecular orbitals (MOs) of the highest occupied molecular orbital (HOMO) and lowest unoccupied molecular orbital (LUMO) for the naphthalene molecule [16]. MOs are obtained by solving the Schrodinger equation, this basic theory method relates MOs of isolated molecules to the flow of electricity. Those orbitals create paths in different molecular orbitals, the green function from the source to the drain will be proportional to $(\Psi^H(r_i)\Psi^H(r_j))^2$ for HOMO and will be proportional to $(\Psi^H(r_i)\Psi^L(r_j))^2$ for LUMO level [16].

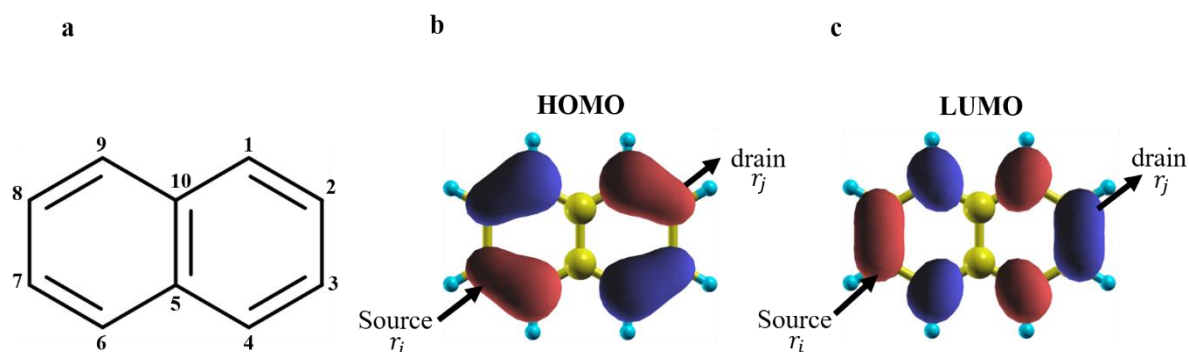


Figure 3.7.1: **Frontier molecular orbitals.** (a) A lattice representation and frontier molecular orbitals of Naphthalene; (b) HOMO wave function for Naphthalene; (c) LUMO wave function for Naphthalene.

This “intra-orbital QI” helps to understand the relationship between the molecular orbitals and quantum interference, which tells us directly the transmission properties, through the ratio of two conductances corresponding to different connectives. Figure 3.7.1 shows that there are only two possibilities: if both HOMO and LUMO have different colours, or if both HOMO and LUMO have the same colours, then it will be destructive QI (DQI). While, if one of them has a different colour, and the other in the same colours, it will be constructive QI (CQI)[16].

For example, in Figure 3.7.1, the HOMO product $\Psi^H(r_7)\Psi^H(r_2)$ (i.e. $-*-$) is positive, where the LUMO product $\Psi^L(r_7)\Psi^L(r_2)$ (i.e. $-*+$) is negative, then this connectivity is constructive QI and the electrical conductance will be high and depends on the amplitude of the wave function on the source and drain. This result was predicted by MRR theory in section 3.6. Despite the fact that these theories are simple, quantitative agreement with experiment has been obtained [18].

3.8. Thermoelectricity

Thermoelectricity is a basis of a couple of interesting devices that can be used in a very wide range of applications such as a thermoelectric cooler and energy harvesting. In particular, the creation of high-performance thermoelectric materials for the conversion of waste heat into electricity via the Seebeck effect. The high thermoelectric efficiency of these nanoelectronic devices for power generation is characterised by the dimensionless figure of merit ZT .

In this section, I will present a brief overview of the Seebeck coefficient, which can be defined as the voltage difference ΔV generated due to the temperature difference ΔT of two electrodes, where they are connected to hot and cold reservoirs respectively. This leads to an electric current I and heat current \dot{Q} passing through a device. Therefore, the linear response analytic

formula for current and heat is derived through thermoelectric coefficients such as thermopower (Seebeck coefficient (S)), electrical conductance (G), thermal conductivity due to both the electrons (k_e) and phonons (k_{ph}) and the figure of merit (ZT). These thermal properties are correlated to my calculation in the following chapters.

3.8.1. The sign of Seebeck coefficient (S)

A thermoelectric device creates a voltage when there is a different temperature between two reservoirs as shown in Figure 3.8.1. The two reservoirs are labelled L and R, with their voltages and temperatures V_L, T_L and V_R, T_R . Define as $\Delta V = V_L - V_R$ and $\Delta T = T_L - T_R$, the chemical potentials are $\mu_L = E_F + eV_L$ and $\mu_R = E_F - eV_R$, where $e = -|e|$ electronic charge and their difference is $\Delta\mu = -|e|\Delta V$. Therefore, steady-state particle current J_1 is defined as the number of electrons per unit of time leaving reservoir L and entering reservoir R through the scattering region. Where the steady-state particle current J_2 is defined as the number of electrons per unit time leaving reservoir R and entering reservoir L through the scattering region.

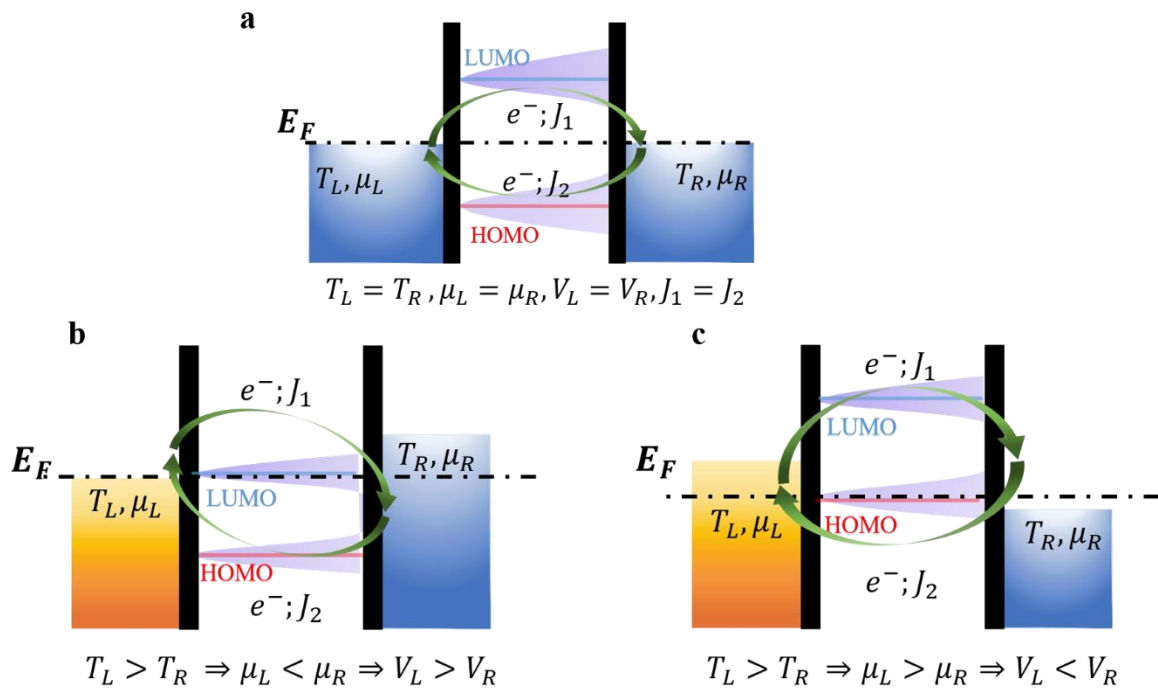


Figure 3.8.1: **A Schematic of different Seebeck signs.** (a) is the equilibrium condition case; (b) and (c) are the cases when the system is HOMO-dominated (i.e. positive Seebeck coefficient) and LUMO-dominated (i.e. negative Seebeck coefficient) transport respectively.

Practically, the net particle current in the first case will be $J = J_1 - J_2$ with an electrical current equal to $I = eJ$. Then, the Seebeck coefficient is given by $S = -\left(\frac{\Delta V}{\Delta T}\right)_{I=0}$. In order to obtain the Seebeck sign, it is easier to start from the equilibrium condition at $\Delta V = 0$ and $\Delta T = 0$ as shown in Figure 3.8.1a. Consider if the temperature T_L of the left reservoir is increased where the population of higher-energy electrons in reservoir L is higher than that of reservoir R. This means that the higher-energy electrons can be easier to pass from reservoir L to reservoir R than lower-energy electrons, thus J_1 will increase where LUMO-dominated transport happens. In addition, to achieve steady state then we should have the steady-state condition $J = 0$, where μ_R must be increased, for that J_2 increases, which demonstrates that if $T_L > T_R$ then $\mu_R > \mu_L$. Hence if $\Delta T > 0$, $\Delta\mu < 0$, $\Delta V > 0$ and $S < 0$. This occurs due to the position of the Fermi energy when it is in the HOMO-LUMO gap of a single molecule and located closer to the LUMO because the electron transmission coefficient is an increasing function of electron energy. Moreover, it can also occur when the Fermi energy is in the bandgap of a semiconductor and near to the conduction band. Conversely, higher-energy electrons find it more difficult to move from reservoir L to reservoir R than lower-energy electrons in the case where the Fermi energy is closer to the HOMO or the valence band. Thus, if T_L is increased relative to T_R , this leads to that J_1 will be decreased and $S > 0$.

3.8.2. Expressions for thermoelectric transport coefficients

This section builds on the arguments in the previous section (3.2), using the expression of the Landauer formula in Eq. 3.2.9, the electron current and heat current expression due to the electrons are expressed as

$$I = \frac{2e}{h} \int_{-\infty}^{\infty} dE T(E) [f_L(E) - f_R(E)] \quad (3.8.1)$$

Similarly, the heat energy per unit of time (i.e. the energy in excess of the fermi-energy)

$$\dot{Q} = \frac{2}{h} \int_{-\infty}^{+\infty} dE (E - E_F) [f_L(E) - f_R(E)] T(E) \quad (3.8.2)$$

As mentioned in Eq. 3.2.10, the Fermi distribution function can be considered as

$$f_L(E) = f(x_L) \quad (3.8.3)$$

Where

$$f(x_L) = \frac{1}{e^{x_L} + 1}; \quad x_L = \frac{E - E_F^L}{k_B T_L} \quad (3.8.4)$$

Similarly to the Fermi energy E_F^R and the temperature of the right reservoir. This step helps to use the Taylor expansion for an analytical function at a point as follows

$$f(x) = f(a) + \frac{df(a)}{da} (x - a) + \dots \quad (3.8.5)$$

In the case where $(x - a)$ is small, a reasonable approximation involves retaining only the first two terms. Thus, if the left and right Fermi-Dirac distribution functions do not differ too much this means $(x_R - x_L)$ is small, then employing Taylor expansion yields

$$f(x_R) \approx f(x_L) + \frac{df(x_L)}{dx_L} (x_R - x_L) \quad (3.8.6)$$

The second term in the above expression is

$$\frac{df(x_L)}{dx_L} = \frac{df_L(E)}{dE} \frac{dE}{dx_L} = k_B T_L \frac{df_L(E)}{dE} \quad (3.8.7)$$

Moreover,

$$\begin{aligned} x_R - x_L &\approx \frac{\partial x_L}{\partial T_L} (T_R - T_L) + \frac{\partial x_L}{\partial E_F^L} (E_F^R - E_F^L) \\ &= -\frac{E - E_F^L}{k_B T_L^2} (T_R - T_L) - \frac{1}{k_B T_L} (E_F^R - E_F^L) \end{aligned} \quad (3.8.8)$$

Consequently

$$f_R(E) - f_L(E) = \left[-\frac{df_L(E)}{dE} \right] \left[\frac{E - E_F^L}{T_R} (T_R - T_L) + (E_F^R - E_F^L) \right] \quad (3.8.9)$$

The last term $(E_F^R - E_F^L) = q(V_R - V_L)$ where q is $e = -|e|$, and $V_R - V_L$ is the voltage difference between the left and right reservoirs.

Combining Eq. 3.8.1 and Eq. 3.8.9, where the left and right Fermi distributions are only slightly different then the total current yields

$$I = \frac{2e}{h} \int_{-\infty}^{+\infty} dE \left[-\frac{df_L(E)}{dE} \right] T(E) \left[\frac{E - E_F^L}{T_L} (T_R - T_L) + (E_F^R - E_F^L) \right] \quad (3.8.10)$$

Similarly, from Eq. 3.8.2 and Eq. 3.8.9 the total heat energy per unit of time yields

$$\begin{aligned} \dot{Q} &= \frac{2}{h} \int_{-\infty}^{+\infty} dE \left[-\frac{df_L(E)}{dE} \right] T(E) \\ &\quad \times \left[\frac{(E - E_F^L)^2}{T_L} (T_R - T_L) + (E - E_F^L)(E_F^R - E_F^L) \right] \end{aligned} \quad (3.8.11)$$

Therefore, for the small different voltages and temperatures and to linear respond regime (i.e. first-order) Eq. 3.8.10 and 3.8.11 can be written as a matrix expression

$$\begin{pmatrix} I \\ \dot{Q} \end{pmatrix} = \frac{2}{h} \begin{pmatrix} e^2 L_0 & \frac{e}{T} L_1 \\ e L_1 & \frac{1}{T} L_2 \end{pmatrix} \begin{pmatrix} V_R - V_L \\ T_R - T_L \end{pmatrix} \quad (3.8.12)$$

where

$$L_n = \int_{-\infty}^{+\infty} dE (E - E_F)^n \left[-\frac{df(E)}{dE} \right] T(E) \quad (3.8.13)$$

In the above expression, the term E_F is the average Fermi energy of the two reservoirs, and the

function $f(E) = \left[e^{\frac{E - \mu_{L(R)}}{k_B T}} + 1 \right]^{-1}$, T is the average temperature of two reservoirs. Since

the electrical conductance is defined to be the ratio $G = I/\Delta V$, then at $\Delta T = 0$ [15]

$$G = G_0 L_0 \quad (3.8.14)$$

where G_0 is the quantum of conductance, as discussed in section 3.2 in Eq. 3.2.12.

In the case of $\Delta I = 0$, Seebeck coefficient is defined to be the ratio $S = -\left(\frac{\Delta V}{\Delta T}\right)_{I=0}$

$$S = \frac{L_1}{e T L_0} \quad (3.8.15)$$

Again $e = -|e|$.

Alternatively, matrix expression in Eq. 3.8.12 can be rearranged into

$$\begin{pmatrix} I \\ \dot{Q} \end{pmatrix} = \begin{pmatrix} G & GS \\ GST & K \end{pmatrix} \begin{pmatrix} \Delta V \\ \Delta T \end{pmatrix} \quad (3.8.16)$$

$$\begin{pmatrix} \Delta V \\ \dot{Q} \end{pmatrix} = \begin{pmatrix} 1/G & -S \\ \Pi & k_e \end{pmatrix} \begin{pmatrix} I \\ \Delta T \end{pmatrix} \quad (3.8.17)$$

Where Π is called the Peltier coefficient, which describes the heat flux from an electrical current this is important for cooling at the nanoscale. In addition, the thermal conductance due to electrons is given by

$$k_e = K_e - GS^2T \quad (3.8.18)$$

where $K_e = 2L_2/h$. Setting $\Delta T = 0$ in Eq. 3.8.17 this gives

$$\Pi = ST \quad (3.8.19)$$

Thus

$$\Pi = \frac{L_1}{eL_0} \quad (3.8.20)$$

and

$$k_e = \frac{2}{hT} \left(L_2 - \frac{(L_1)^2}{L_0} \right) \quad (3.8.21)$$

As a result of these quantities, the electric contribution to a thermoelectric figure of merit is given by[16]

$$ZT_e = \frac{S^2GT}{k_e} = \frac{(L_1)^2}{L_0L_2 - (L_1)^2} \quad (3.8.22)$$

ZT_e describes the property of electrons only. It is convenient to consider the case of low-temperature limit, then the transmission spectrum varies approximately linearly with energy (E) on the scale of $k_B T$ leads to

$$L_0 \approx T(E_F)$$

$$L_1 \approx (eT)^2 \alpha \left(\frac{dT(E)}{dE} \right)_{E=E_F} \quad (3.8.23)$$

$$L_2 \approx (eT)^2 \alpha T(E_F)$$

where α is the Lorentz number that is equal to $\alpha = 2.44 \times 10^{-8} W \cdot \Omega \cdot K^{-2}$. Therefore, from the expressions above, the electrical conductance, Seebeck coefficient, and thermal conductance due to electrons at this limit will take the following forms

$$G(E_F) \approx \left(\frac{2e^2}{h} \right) T(E_F) \quad (3.8.24)$$

$$S(E_F) \approx eT \alpha \left(\frac{d \ln [T(E)]}{dE} \right)_{E=E_F} \quad (3.8.25)$$

$$k_e \approx \alpha T G \quad (3.8.26)$$

Eq. 3.8.26 is well-known as the Wiedemann–Franz law, this indicates that thermal conductance is proportional to the electrical conductance when $T(E_F)$ varies slowly with Fermi energy on the scale of $k_B T$. Moreover, if the function $T(E)$ in Eq. 3.8.25 is an increasing function of E , then the term $\left(\frac{d \ln [T(E)]}{dE} \right)_{E=E_F} > 0$ leading to $S < 0$. This also illustrates that the Seebeck coefficient S can be enhanced by increasing the slope of transmission spectra $T(E)$. Based on the Wiedemann–Franz law, thermal conductance equation yields $ZT_e = \frac{S^2}{\alpha}$. in order to achieve $ZT_e > 1$, the Seebeck coefficient should be taken the value $S^2 > \alpha$, which is satisfy $S > 150 \mu V K^{-1}$ [16].

It is worth mentioning that, all the previous calculations are in absence of the phonon contribution to thermal transport, as in Eq. 3.8.22 ZT_e is large when k_e value is small, this means that the thermal conductance due to the phonons k_{ph} is the dominant contribution. This is another major challenge feature in designing in the thermoelectric material, which is controlled by the full figure of merit ZT ,

$$ZT = \frac{ZT_e}{1 + (k_{ph}/k_e)} \quad (3.8.27)$$

Therefore, the total ZT relies on not only the thermal conductance due to the electrons, but also on the thermal conductance due to the phonon. It is a crucial point to calculate k_{ph} through a molecular junction, which is obtained by solving the phonon transmission coefficient $T_{pk}(\omega)$, where ω is the frequency that carries an energy $\hbar\omega$. [17]

$$k_{ph}(T) = \frac{1}{2\pi} \int_0^\infty \hbar\omega T_{pk}(\omega) \frac{\partial f_{BE}(\omega, T)}{\partial T} d\omega \quad (3.8.28)$$

Since, $f_{BE}(\omega, T) = \left(e^{\frac{\hbar\omega}{k_B T}} - 1 \right)^{-1}$ is the Bose-Einstein distribution function, \hbar is reduced Plancks constant and $k_B = 8.6 \times 10^{-5} eV/K$ is Boltzmann's constant. Substituting Eq. 3.8.27 into Eq. 3.8.22, the thermoelectric figure of merit yields

$$ZT = \frac{S^2 GT}{k_e + k_{ph}} \quad (3.8.29)$$

Techniques for computing $T_{pk}(\omega)$ in nanoscale structures were developed several years ago [19] and were recently generalised to yield phonon thermal conductances in molecular-scale junctions [20][21][22].

Bibliography:

- [1] C. Joachim and M. A. Ratner, “Molecular electronics: Some views on transport junctions and beyond,” *Proc. Natl. Acad. Sci. U. S. A.*, vol. 102, no. 25, pp. 8801–8808, 2005.
- [2] S. Ahn *et al.*, “Electronic transport and mechanical stability of carboxyl linked single-molecule junctions,” *Phys. Chem. Chem. Phys.*, vol. 14, no. 40, pp. 13841–13845, 2012.
- [3] R. Landauer, “Spatial variation of currents and fields due to localized scatterers in metallic conduction,” *IBM J. Res. Dev.*, vol. 1, no. 3, pp. 223–231, 1957.
- [4] M. Büttiker, Y. Imry, R. Landauer, and S. Pinhas, “Generalized many-channel conductance formula with application to small rings,” *Phys. Rev. B*, vol. 31, no. 10, p. 6207, 1985.
- [5] S. Datta, *Electronic transport in mesoscopic systems*. Cambridge university press, 1997.
- [6] E. N. Economou, *Green’s functions in quantum physics*, vol. 7. Springer Science & Business Media, 2006.
- [7] G. Breit and E. Wigner, “Capture of slow neutrons,” *Phys. Rev.*, vol. 49, no. 7, p. 519, 1936.
- [8] S.-H. Ke, W. Yang, and H. U. Baranger, “Quantum-interference-controlled molecular electronics,” *Nano Lett.*, vol. 8, no. 10, pp. 3257–3261, 2008.
- [9] R. Stadler, “Quantum interference effects in electron transport through nitrobenzene with pyridil anchor groups,” *Phys. Rev. B*, vol. 80, no. 12, p. 125401, 2009.
- [10] T. A. Papadopoulos, I. M. Grace, and C. J. Lambert, “Control of electron transport

- through Fano resonances in molecular wires,” *Phys. Rev. b*, vol. 74, no. 19, p. 193306, 2006.
- [11] C. Lambert, “Basic concepts of quantum interference and electron transport in single-molecule electronics,” *Chem. Soc. Rev.*, vol. 44, no. 4, pp. 875–888, 2015.
- [12] J. C. Cuevas and E. Scheer, *Molecular electronics: an introduction to theory and experiment*. World Scientific, 2010.
- [13] C. A. Stafford, D. M. Cardamone, and S. Mazumdar, “The quantum interference effect transistor,” *Nanotechnology*, vol. 18, no. 42, p. 424014, 2007.
- [14] C. M. Finch, V. M. Garcia-Suarez, and C. J. Lambert, “Giant thermopower and figure of merit in single-molecule devices,” *Phys. Rev. b*, vol. 79, no. 3, p. 33405, 2009.
- [15] C. J. Lambert, H. Sadeghi, and Q. H. Al-Galiby, “Quantum-interference-enhanced thermoelectricity in single molecules and molecular films,” *Comptes Rendus Phys.*, vol. 17, no. 10, pp. 1084–1095, 2016.
- [16] C. J. Lambert, *Quantum Transport in Nanostructures and Molecules*. IOP Publishing, 2021.
- [17] H. Sadeghi, S. Sangtarash, and C. J. Lambert, “Oligoyne Molecular Junctions for Efficient Room Temperature Thermoelectric Power Generation,” *Nano Lett.*, vol. 15, no. 11, pp. 7467–7472, 2015.
- [18] S. Sangtarash *et al.*, “Searching the Hearts of Graphene-like Molecules for Simplicity, Sensitivity, and Logic,” *J. Am. Chem. Soc.*, vol. 137, no. 35, pp. 11425–11431, 2015.
- [19] A. Kambili, G. Fagas, V. I. Fal, and C. J. Lambert, “Phonon-mediated thermal conductance of mesoscopic wires with rough edges,” *Phys. Rev. B-Condensed Matter*,

- vol. 60, no. 23, pp. 593–596, 1999.
- [20] N. Mosso *et al.*, “Thermal Transport through Single-Molecule Junctions,” *Nano Lett.*, vol. 19, no. 11, pp. 7614–7622, 2019.
- [21] C. Evangelini *et al.*, “Nanoscale Thermal Transport in 2D Nanostructures from Cryogenic to Room Temperature,” *Adv. Electron. Mater.*, vol. 5, no. 10, p. 1900331, 2019.
- [22] M. Famili, I. Grace, H. Sadeghi, and C. J. Lambert, “Suppression of Phonon Transport in Molecular Christmas Trees,” *ChemPhysChem*, vol. 18, no. 10, pp. 1234–1241, 2017.

4. Conformation and Quantum-Interference-Enhanced Thermoelectric Properties of Diphenyl Diketopyrrolopyrrole Derivatives.

In this chapter, I study the connectivity dependence of the thermoelectric properties of a series of thiophenediketopyrrolopyrrole (DPP) derivative molecules using density functional theory and tight-binding modelling, combined with quantum transport theory. I find a significant dependence of electrical conductance on the connectivity of the two thiophene rings attached to the DPP core. Furthermore, I find that DQI connectivity leads to enhanced Seebeck coefficients, which can reach 500~700 $\mu\text{V}/\text{K}$. After including the contribution to the thermal conductance from phonons, the full figure of merit ZT for the CQI molecules could reach 1.5 at room temperature.

The results presented in this chapter were published in R. Almughathawi, S. Hou, Q. Wu, Z. Liu, W. Hong, and C. Lambert, “Conformation and Quantum-Interference-Enhanced Thermoelectric Properties of Diphenyl Diketopyrrolopyrrole Derivatives,” *ACS Sensors*, vol. 6, no. 2, pp. 470–476, 2021

4.1. Introduction

The foundational experiments of Nongjian Tao[1] and subsequent work exploring charge transport through single molecules connected to two metallic electrodes[2][3][4] have led to the design of molecular-scale components such as switches[4][5][6], rectifiers[7] and highly conjugated molecular wires[8]. A more recent goal of this research is the design of thermoelectric materials[9] or devices[10] based on single molecules or self-assembled monolayers[11], which can convert heat into electricity and contribute to the global challenge of green energy harvesting. Such organic materials and devices are potentially lightweight, flexible, environmentally friendly and cost-effective[12][13]. Diphenyl diketopyrrolopyrrole discovered by Farnum et al. in 1974[14] has unique properties, such as good conjugation, strong electron-withdrawing ability, thermal stability and photostability, and high-fluorescence quantum efficiency[15][16]. It is widely used as a building block for organic molecules, both for fundamental studies of electronic properties and for industrial applications as dyes and pigments[15][17]. Furthermore, the diketopyrrolopyrrole (DPP)-based molecule could be placed between aromatic rings such as the five-membered heterocycle thiophene,[18] which creates the possibility of tuning their transport properties. In this work, stimulated by measurements of thermoelectricity in bulk DPP-based films, which show that a thermoelectric figure of merit of $ZT = 0.25$ could be achieved,[19] we examine how room-temperature quantum interference in DPP cores influences their charge and heat transport properties and assess whether or not DPP derivatives are potential thermoelectric materials at the nanoscale.

Figure 4.1a shows the series of molecules of interest. DPP1, DPP2 and DPP3 contain thiophene rings with different connectivities, corresponding to inequivalent positions of the sulphur atoms of the thiophenes. Furthermore, each molecule is found to have two stable geometries labelled a or b, corresponding to different orientations of the thiophene rings relative to the DPP core.

In what follows, we shall show that the Seebeck coefficients of DPP2 and DPP3 could reach $500 - 700 \mu\text{V/K}$. After including the contribution of phonons to the thermal conductance, the full ZT s for molecules DPP1-a and -b reach 1.5 at room temperature and could increase to 2 when the temperature increases to 400K. By exploring the effect of charge-transfer doping using tetracyanoquinodimethane (TCNQ), which is a well-known electron acceptor[20][21], we found that TCNQ can be used to change the signs of the Seebeck coefficients.

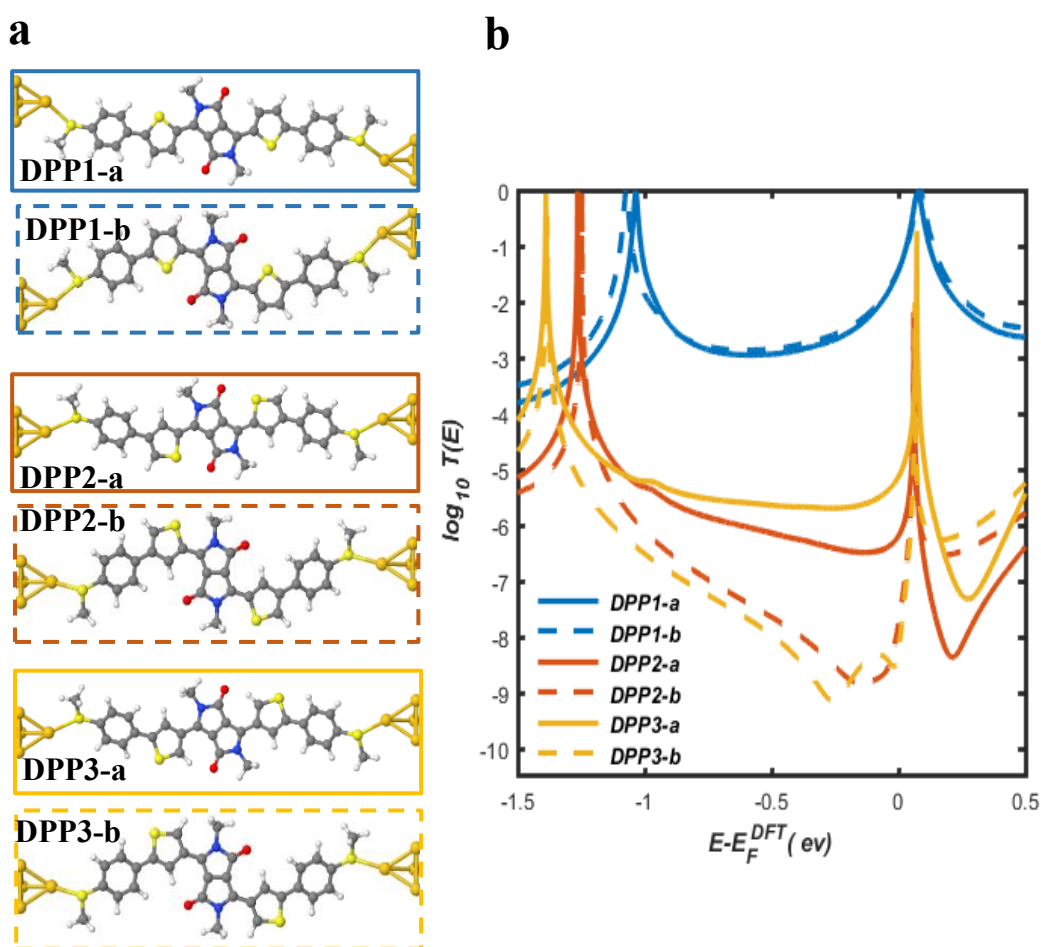


Figure 4.1. **Charge transport properties of diketopyrrolopyrrole (DPP) derivative isomers attached to gold electrodes via -SMe anchor groups.** (a) Models of the gold/molecule/gold sandwich junctions. The colours assigned to the atoms are as follows: grey for carbon, yellow for sulphur, red for oxygen, blue for nitrogen, white for hydrogen, and orange for gold electrode atoms. (b) DFT-based transmission spectra against Fermi energy (E_F). DPP1-a, -b (blue solid and dashed curves) exhibit constructive quantum interference (CQI) while DPP2-a, -b (red

solid and dashed curves) and DPP3-a, -b (yellow solid and dashed curves) display destructive quantum interference (DQI).

4.2. Results and Discussion

We systematically investigated the electrical and thermoelectrical properties of gold/thiophene-diketopyrrolopyrrole (DPP) /gold hybrid junctions (Figure 4.1a) using quantum transport theory combined with the mean-field Hamiltonian of each geometry obtained from tight-binding models of each molecule. The optimized geometry and ground-state Hamiltonian and overlap matrix elements of each structure were self-consistently obtained using the SIESTA[22] implementation of density functional theory (DFT). SIESTA employs norm-conserving pseudopotentials to account for the core electrons and linear combinations of atomic orbitals to construct the valence states. The generalized gradient approximation (GGA) of the exchange and correlation functional is used with the Perdew–Burke–Ernzerhof parametrization (PBE)[23] a double- ζ polarized (DZP) basis set, a real-space grid defined with an equivalent energy cutoff of 200 Ry. The geometry optimization for each structure is performed to the forces smaller than 10 meV/Å. After that, the mean-field Hamiltonian obtained from the converged DFT calculation or a tight-binding Hamiltonian (using single orbital energy site per atom with Hückel parameterization) was combined with our homemade implementation Gollum[24] to calculate the phase-coherent, elastic scattering properties of each system consisting of left gold (source) and right gold (drain) leads and the scattering region (molecules DPP1, DPP2, and DPP3). The transmission coefficient $T(E)$ for electrons of energy E (passing from the source to the drain) is calculated via the following relation:

$$T(E) = \text{Trace} (\Gamma_R(E)G^R(E)\Gamma_L(E)G^{R\dagger}(E)) \quad (4.20)$$

In this expression, $\Gamma_{L,R}(E) = i (\Sigma_{L,R}(E) - \Sigma_{L,R}^\dagger(E))$ describes the level broadening due to the coupling between left (L) and right (R) electrodes and the central scattering region, $\Sigma_{L,R}(E)$ are the retarded self-energies associated with this coupling and $G^R(E) = (ES - H - \Sigma_L - \Sigma_R)^{-1}$ is the retarded Green's function, where H is the Hamiltonian and S is overlap matrix. As discussed in chapter 3, using the transmission coefficient $T(E)$, the electrical conductance G , the Seebeck coefficient S , and electronic thermal conductance κ_e and the electronic figure of merit ZT_e can be calculated through the following formula:

$$G = G_0 L_0 \quad (4.2)$$

$$S = -\frac{L_1}{|e|TL_0} \quad (4.3)$$

$$\kappa_e = -2\frac{L_0L_2 - L_1^2}{hTL_0} \quad (4.4)$$

$$ZT_e = \frac{L_1^2}{L_0L_2 - L_1^2} \quad (4.5)$$

In the linear response limit the quantity $L_n(T, E_F)$ is given by

$$L_n(T, E_F) = \int_{-\infty}^{+\infty} dE (E - E_F)^n T(E) \left(-\frac{\partial f(E)}{\partial E} \right) \quad (4.6)$$

where $G_0 = 2e^2/h$ is conductance quantum, e is the charge of an electron; h is the Planck's constant; E_F is the Fermi energy; $f(E) = (1 + \exp((E - E_F)/k_B T))^{-1}$ is the Fermi-Dirac distribution function, T is the temperature, and $k_B = 8.6 \times 10^{-5}$ eV/K is Boltzmann's constant. The electronic figure of merit ignores k_{ph} due to phonons, whereas the figure of merit ZT experimentally is defined by $ZT = S^2 GT / (k_e + k_{ph})$, which includes the thermal conductance due to both phonons and electrons in the denominator. In order to calculate the vibrational modes of a system, I use the harmonic approximation method to construct the $3n \times 3n$ dynamical matrix D . From the ground state of the relaxed x, y, z coordinates of the

system, each atom will be moved in six-direction from the equilibrium position to calculate the energy difference and the forces as the following.

To calculate the thermal conductance k_{ph} due to phonons, the force constant matrix, K , is obtained by finite differences:

$$K_{i\alpha,j\beta} = \frac{\partial^2 E}{\partial r_{i\alpha} \partial r_{j\beta}} = -\frac{F_{j\beta}(Q_{i\alpha}) - F_{j\beta}(-Q_{i\alpha})}{2Q_{i\alpha}} \quad (4.7)$$

where E is the total energy and $r_{i\alpha}(r_{j\beta})$ is the displacement of atom $i(j)$ in the coordinate direction $\alpha(\beta)$. The geometry is relaxed until the force of each atom is equal to 0.01 eV \AA^{-1} . By shifting each atom (i) with $Q_{i\alpha} = 0.01 \text{ \AA}^\circ$ in the direction $\alpha = x, y, z$ the forces on atom along $\beta = x, y, z$ direction, where $F_{j\beta}(Q_{i\alpha})$ is calculated. Thus, the dynamical matrix D can be obtained by $K_{i\alpha,j\beta}/\sqrt{m_i m_j}$, where m_i m_j are the masses of atom i and atom j . Then the dynamical matrix is used to compute the transmission probability of phonons using the Gollum transport code with Eq.1. The corresponding phonon thermal conductance is given by

$$k_{ph}(T) = \int_0^\infty \frac{\hbar\omega}{2\pi} T_{ph}(\omega) \frac{\partial f_{BE}(\omega, T)}{\partial T} d\omega \quad (4.8)$$

The variable $\partial f_{BE}(\omega, T) = 1/[e^{\left(\frac{\hbar\omega}{k_B T}\right)} - 1]$ is the Bose–Einstein distribution.

The DPP derivative isomers are defined through their connectivity and orientation of the thiophene rings shown in Figure 4.1a. Figure 4.1b displays that both DPP1-a and DPP1-b exhibit constructive quantum interference (CQI) signalled by the absence of a dip in their transmission functions $T(E)$ within the HOMO–LUMO gap resulting in high electrical conductance, whereas both isomers of DPP2 and DPP3 exhibit destructive quantum interference (DQI) signalled by the presence of such a dip leading to lower electrical conductance. In all cases, charge transport is mainly LUMO-dominated. More specifically, the transmission functions of molecules DPP1-a and DPP1-b shown by the blue solid and dashed

curves are rather similar. In contrast, the different isomers of molecules possess significantly different transmission functions. Near their transmission minima, the transmission coefficients of DPP2-a and DPP3-a (red and orange solid curves) are 2 to 3 orders of magnitude higher than those of DPP2-b and DPP3-b (red and orange dashed curves).

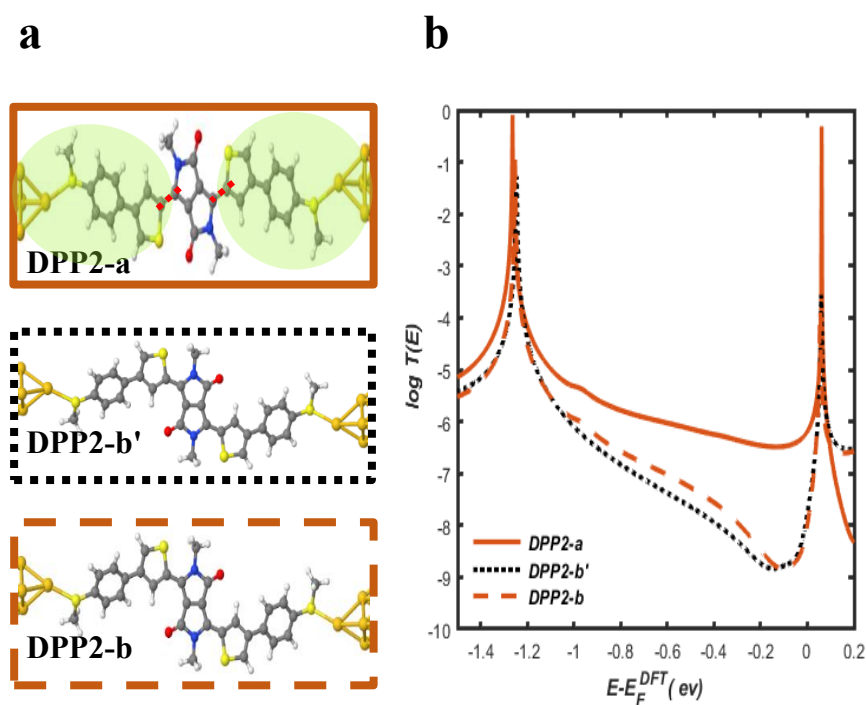


Figure 4.2.1. **DFT-based transmission functions for DPP2-a and DPP2-b connected to the gold via SMe-anchor groups.** (a) DPP2-based molecular structures; (b) Transmission coefficients as a function of Fermi-energy for DPP2-a (red solid curve), DPP2-b' (black dotted curve), which is the rotated geometry obtained from DPP2-a and DPP2-b (red dashed curve).

To understand the conductance difference between DPP2/3-a and DPP2/3-b, we further checked the geometries. More specifically, the result in Figure 4.2.1 shows that after relaxation, the geometries of DPP2-a and DPP2-b have different angles contact between the linker and the electrode. (Note: Initial structure of b is obtained by rotating linker and electrode (indicated by the green shaded regions) relative to the DPP-core through 180° around the axis based on a geometry) Therefore, to test if this could cause the difference in their transmission coefficients

(shown as red solid and dashed curves respectively), the transmission coefficient of geometry DPP2-b' (black dotted curve) is shown. DPP2-b' is the initial structure of and DPP2-b without further relaxation. Since DPP2-b' and DPP2-b possess similar transmission coefficients, this shows that the 180° rotation is the main difference between DPP2-a and DPP2-b. Other geometry changes due to further relaxation, which lead to slight differences between DPP2-b and DPP2-b' have a negligible effect. The corresponding frontier orbitals of the individual gas-phase molecules are shown in table 4.2.1. Similar to the result in Figure 4.2.1, we tested the geometries of DPP3- a and DPP3-b in the same way which are displayed in Figure 4.2.2.

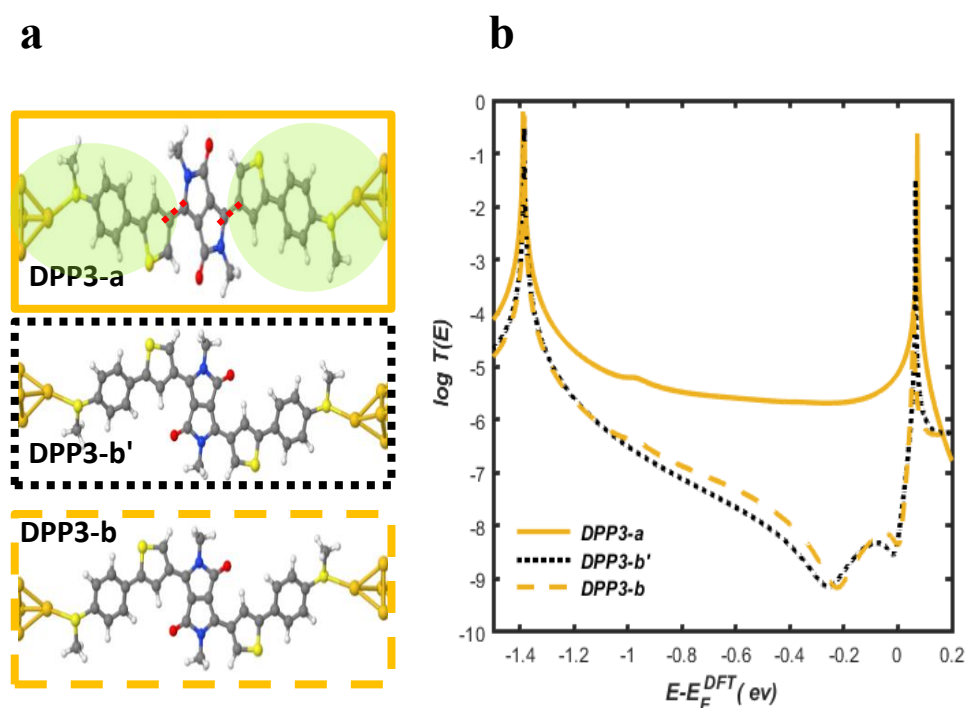
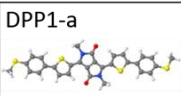
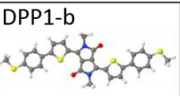
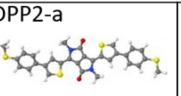
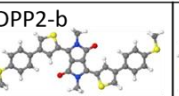
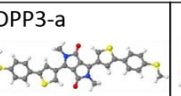
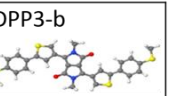
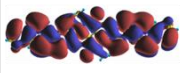
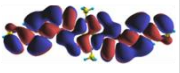
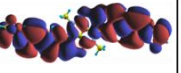
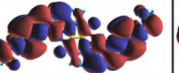
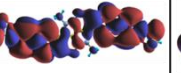
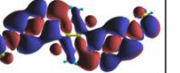
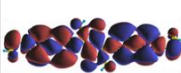
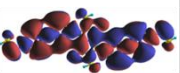
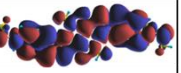
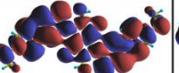
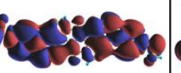
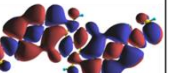
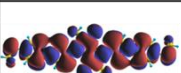
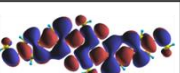
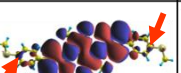
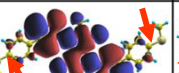

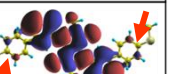
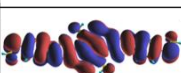
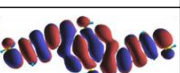
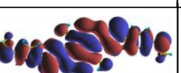
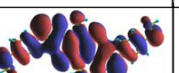
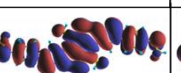
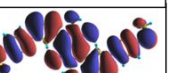
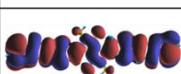
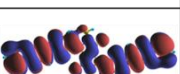
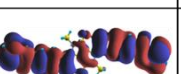
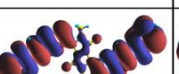
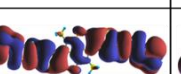
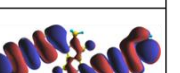



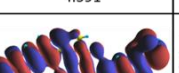
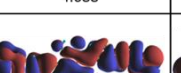
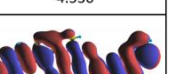


Figure 4.2.2. **DFT-based transmission functions for DPP3-a, b connected to the gold via SMe-anchor.** (a) DPP3 based molecular structures; (b) Transmission coefficients as a function of Fermi-energy for DPP3-a (solid curve), DPP3-b' (black dotted curve) and DPP3-b (dashed curve).

These features in transmission functions could be further interpreted from the perspective of the quantum interference between the molecular orbitals. From the molecular orbitals (MOs) of the gas-phase molecules DPP1, -2, and -3, Table 4.2.1 shows that the frontier molecular

orbitals of DPP1-a, -b are delocalized across the molecule, while for DPP2-a, -b and DPP3-a, -b, the LUMO is localized on the DPP core. Consequently, the LUMO of these molecules will not contribute significantly to the transmission function. Furthermore, from the phases of the MOs on the terminal groups, it is clear that the LUMO+1 and HOMO will interfere destructively according to orbital product rule[27][28]. In contrast, the delocalized LUMO of DPP1 interferes constructively with the HOMO, which leads to the higher transmission around Fermi energy. As indicated by the arrows in Tables 4.2.2 and 4.2.3, the LUMOs of DPP2-a and DPP3-a have a larger weight on the terminal groups than those of DPP2-b and DPP3-b, which contributes to the higher transmission coefficient within the HOMO–LUMO gap of DPP2-a, 3-a compared with DPP2-b, 3-b, shown in Figure 4.1.

Table 4.2.1. Molecular orbitals of DPP-isomers with different connectivities, along with their MO energies

	DPP1-a	DPP1-b	DPP2-a	DPP2-b	DPP3-a	DPP3-b
						
E_F (eV)	-3.418	-3.439	-3.555	-3.577	-3.472	-3.476
LUMO+2						
E (eV)	-1.391	-1.418	-1.445	-1.453	-1.766	-1.688
LUMO+1						
E (eV)	-1.921	-1.949	-1.700	-1.727	-1.826	-1.782
LUMO						
E (eV)	-2.850	-2.859	-2.866	-2.890	-2.731	-2.846
HOMO						
E (eV)	-3.981	-4.020	-4.197	-4.206	-4.173	-4.277
HOMO-1						
E (eV)	-4.774	-4.754	-4.695	-4.591	-4.688	-4.530
HOMO-2						
E (eV)	-4.867	-4.858	-4.729	-4.622	-4.739	-4.579

The red arrows in tables 4.2.1 show that the LUMO of DPP2-a and DPP3-a have a significant weight on the carbon atoms of the terminal phenyl ring, which bond to the SMe anchor groups, whereas the corresponding weights of the LUMOs of DPP2-b and DPP3-b on these atoms are negligible. Consequently the LUMOs of DPP2-a and DPP3-a contribute to transport, whereas the LUMOs of DPP2-b and DPP3-b do not. Furthermore, this delocalization means there is a π -conjugated pathway between the rings.

It is interesting to note that quantum interference is sensitive to the dihedral angle between the central core and the neighbouring thiophenes. To demonstrate this effect, we performed calculations, in which the two electrode–anchor–phenyl–thiophene substructures are rotated through a dihedral angle, θ , as indicated in the Figure 4.2.3. Taking DPP2 as an example, panels b and c of Figures 4.2.3 show the total energy against θ and the corresponding transmission spectra arising for different values of θ . The two configurations (0° (DPP2-b) and 180° (DPP2-a)) have lower energies. The former is a global minimum, and the latter is a local minimum. By increasing θ from 0° (DPP2-b) to 180° (DPP2-a), the destructive quantum interference dip first moves to the right and then moves back. Therefore, the quantum interference pattern is indeed sensitive to rotations, with the mid-gap transmission decreasing by almost 4 orders of magnitude at the most energetically unfavorable angles. Rotation-angle sensitivities of this kind have been reported for other molecules in the literature, examples of which can be found in refs [25] and [26].

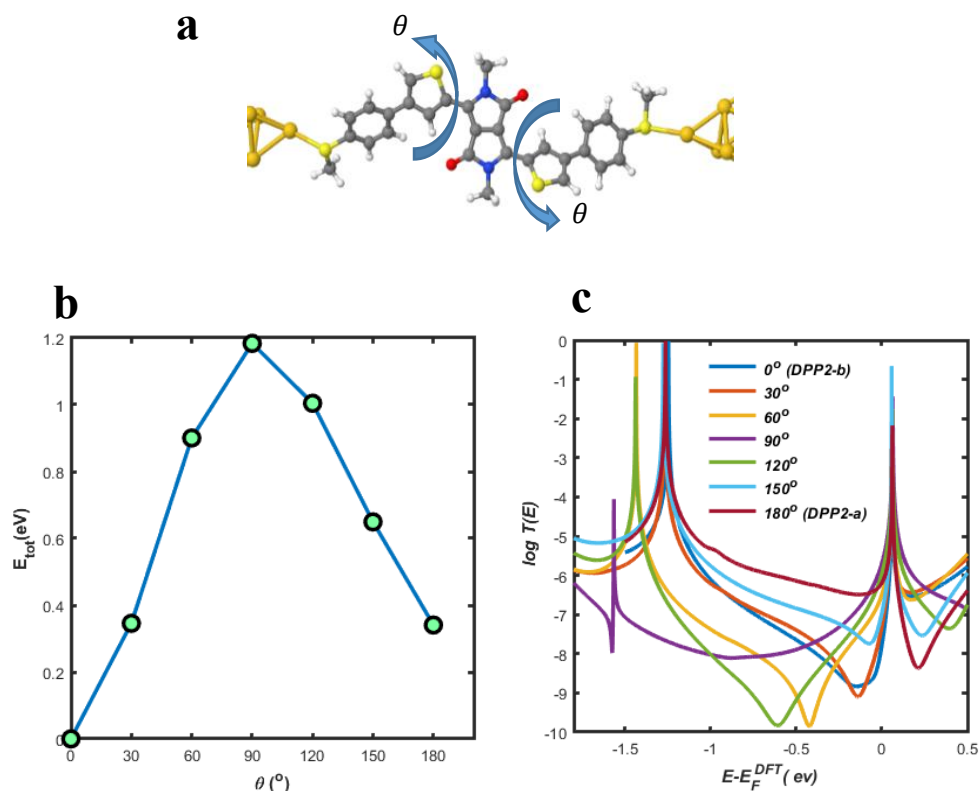


Figure 4.2.3: DFT-based transmission functions for DPP2-a, b connected to the gold via SMe-anchor at different dihedral angles. (a) For DPP-2, this shows the dihedral angle θ , which is varied from 0° to 180° ; (b) Total energy versus θ ; (c) Transmission coefficients as a function of energy for DPP2-b molecule at various dihedral angles θ , which is rotated from both left and right at the same time.

The difference between transmission functions of molecules exhibiting CQI or DQI is mainly attributed to the connectivity of the thiophene rings. In order to illustrate the dependence of the connectivity on transmission coefficients, it is helpful to understand the properties of central cores formed from thiophene rings alone. Panels a and c of Figures 4.2.4 show the transmission functions of cores formed from thiophene monomers and thiophene dimers with different connectivities. The transmission functions of molecules S2, S2', S3, S3' in Figure 4.2.4 b,d (red and yellow curves) exhibit DQI signalled by the presence of a dip in the $T(E)$ within the HOMO-LUMO gap, whereas those of molecules S1 and S' in Figure 4.2.4 b,d (blue curves) exhibit CQI, signalled by the absence of such a dip. The qualitative features of this connectivity

dependence is captured by a simple tight-binding models (TBM), in which the π orbitals are assigned nearest-neighbour couplings only. The Hamiltonian of the simple tight-binding model describes a single orbital per atom with nearest-neighbour couplings $\gamma = -1$. All site energies are set to zero, except the site energies of sulphurs.

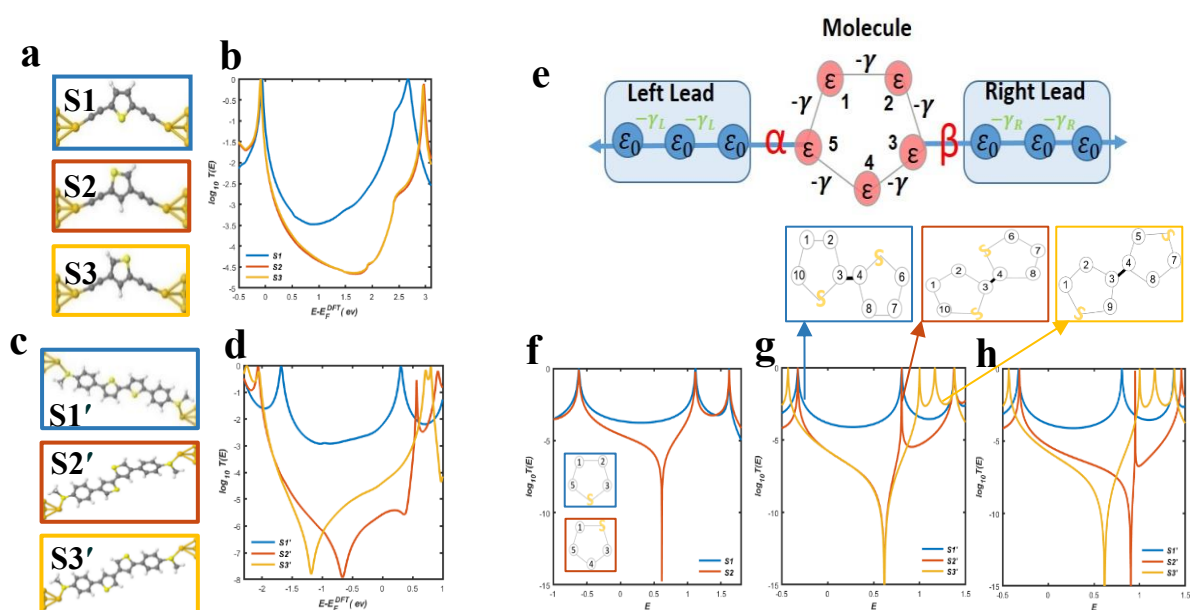


Figure 4.2.4. Comparison of DFT and tight-binding model-based transmission functions for three different connectivities of monomer and dimer thiophene rings. (a) Junctions formed from thiophene monomers S1, S2, and S3 with different connectivities. (b) Corresponding DFT-based transmission coefficients. (c) Junctions formed from thiophene dimers S1', S2', and S3' with the connectivities corresponding to those of molecules DPP1-a, DPP2-a, and DPP3-a in Figure 4.1a. (d) The corresponding DFT-based transmission coefficients. (e) Tight-binding model (TBM) consisting of a five-membered ring attached to two semi-infinite one-dimensional chains through weak couplings $\alpha = \beta = 0.1$. The on-site energies of the molecule (red dots) and the leads (blue dots) are ϵ and ϵ_0 , respectively. In the simplest model considered here, these are all set to zero except for those sites occupied by sulphur, which are assigned an on-site energy ϵ_s . For S1, S2, and S3, the sulphur sites are 4, 1, and 2, respectively, and the leads are connected to sites 3 and 5. The hopping integrals between nearest neighbour atoms are set to $-\gamma = -\gamma_L = -\gamma_R = -1$. (f) TBM transmission functions for S1 and S2, obtained with a sulphur on-site energy of $\epsilon_s = -2$. By symmetry, the transmission function of S3 is identical to that of S2. (g) TBM transmission functions for two

thiophene rings with sites (10, 6) and (1, 7) connected to one-dimensional leads, respectively. The TB lattices associated with each curve are indicated by blue red and yellow arrows and correspond to the connections to the cores of S1' to S3' shown in panel c. For each connectivity, the on-site energies of both sulphurs have the same value ($\epsilon_s = -2$). (h) As for panel g, except the on-site energies of both sulphurs of S2' are changed to $\epsilon_s = -1.2$, to account for the fact that their environments differ from those of S1'. This moves the curves closer to DFT results shown in panel d.

The values used for the site energies of the sulphurs in the tight-binding model of Figure 4.2.4 f,h are guided by our DFT calculations. Comparisons between the two approaches show that a TBM with only a single free parameter (i.e. the sulphur site energy, ϵ_s) can capture the main qualitative features of the much more demanding DFT simulations. To illustrate the role of this parameter, Figure 4.2.5 shows how the TBM transmission coefficients would change if other nonoptimal values of ϵ_s are chosen. Results are shown for a series of on-site energies of the sulphurs, ranging from $\epsilon_s = -0.4$ to $\epsilon_s = -2$ and reveal that the transmission dip moves to lower energies as ϵ_s becomes more negative.

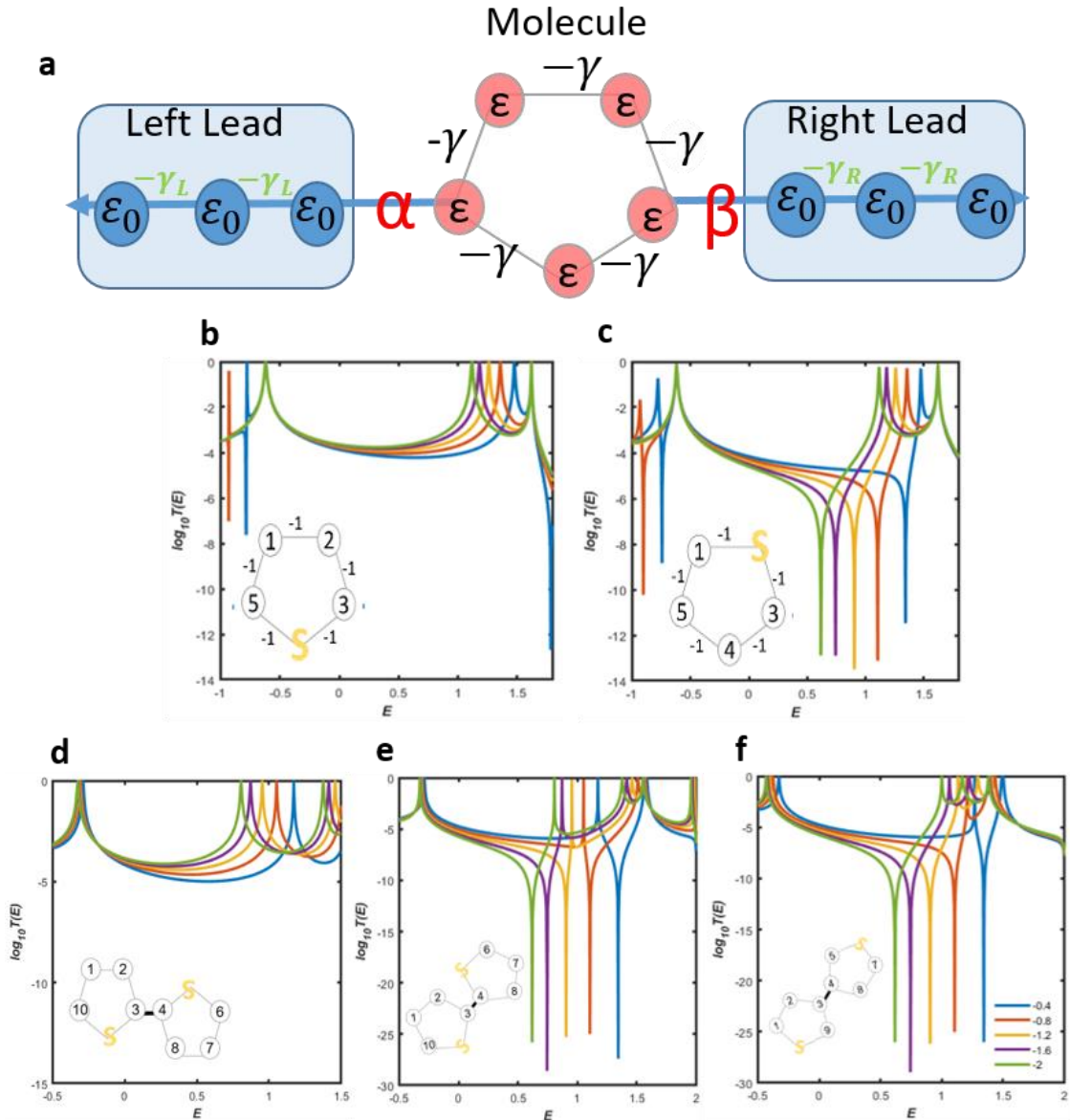


Figure 4.2.5. **Tight-binding model-based transmission functions for different connectivities.** (a) A tight binding model consisting of a five-membered ring attached to two semi-infinite one-dimensional chains through weak couplings $\alpha = \beta = 0.1$. All on-site energies of the molecule (red dots) and the leads (blue dots) are set to zero, except those for sulphurs. The hopping integrals between two nearest-neighbour atoms are set to $-\gamma = -\gamma_L = -\gamma_R = -1$. (b, c) Transmission functions for one thiophene ring with sites 3 and 5 are connected to leads. For each connectivity, several on-site energy values (-0.4, -0.8, -1.2, -1.6, -2) are chosen for the sulphurs in the thiophene rings and the corresponding transmission curves are plotted. (d-f) Transmission functions for two thiophene rings when sites (10, 6) and (1, 7) are connected to leads respectively.

Starting from the DFT-based transmission functions, we evaluated thermoelectric properties of the above molecules according to Eq. 4.2 - 4.5, including their electrical conductances, G ; their Seebeck coefficients, S ; electronic thermal conductances, κ_e , and electronic figure of merit, ZT_e . These are shown in Figure 4.2.7 The Mott formula $S \propto -\frac{\partial \ln T(E)}{\partial E} \Big|_{E=E_F}$ indicates that a large Seebeck coefficient can be obtained if the Fermi energy (E_F) happens to coincide with a steep slope of electron transmission coefficient, $T(E)$ [29][30]. As a consequence, the Seebeck coefficient is higher for molecules exhibiting DQI (red yellow curves) as shown in Figure 4.2.7b. We find that the Seebeck coefficients for DQI molecules DPP2-a,-b and DPP3-a,-b could reach 400 – 700 $\mu V/K$. Figure 4.2.7c shows κ_e due to the electrons obtained from the electron transmission functions. The heat transport due to electrons for the CQI in Figure 4.2.7c (blue curve) has a shape similar to CQI of the electrical conductance in Figure 4.2.7a, reflecting the Wiedemann–Franz law. The thermal conductance due to electrons for DPP1-a,-b is in the range between 1 and 40 pW/K , which is comparable with typical thermal conductances due to phonons, $\sim 10 pW/K$. The molecules exhibiting DQI possess substantially lower values of κ_e . Consequently, their high ZT_e do not lead to high values of the full ZT .

In comparison, Figure 4.2.8 shows the effect of temperature (T) on the thermoelectric performance of thiophene-DPP derivatives and reveals that $ZT_e(T)$ increases with temperature up to a maximum value, before decreasing at higher temperatures. As mentioned above, $ZT_e(T)$ only includes the thermal conductance κ_e .

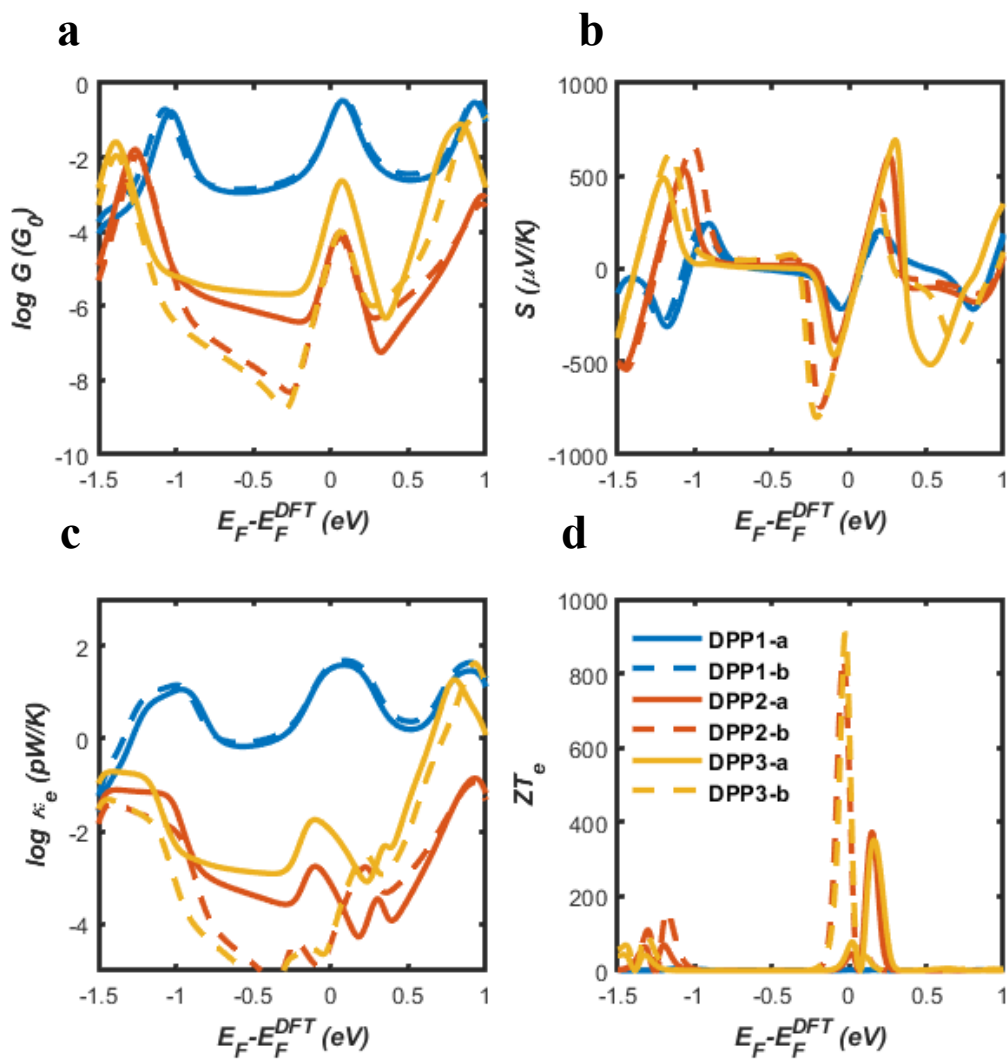


Figure 4.2.7. Thermoelectric properties of the thiophene-DPP isomers as the function of the Fermi energy at room temperature 300 K. (a) Electrical conductance $G(E_F)$; (b) Seebeck coefficients $S(E_F)$; (c) Thermal conductance $\kappa_e(E_F)$; (d) Electronic figure of merit $ZT_e(E_F)$.

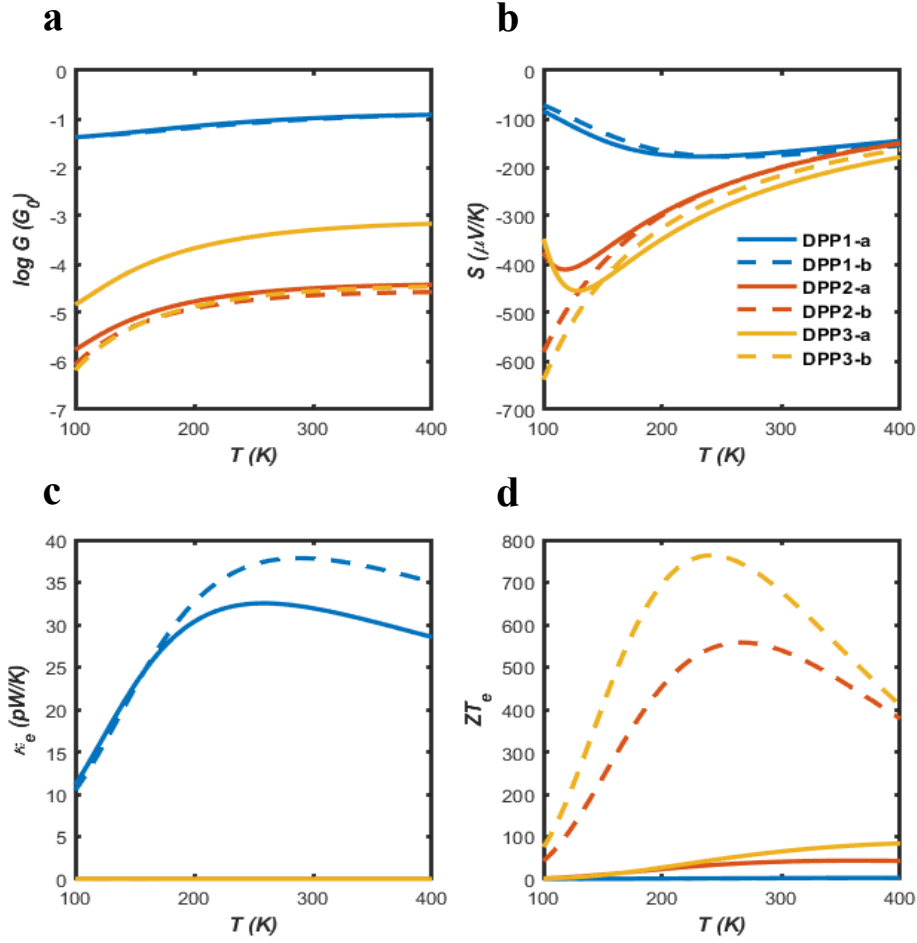


Figure 4.2.8. **Thermoelectric properties of the molecules as a function of temperature at $E_F = 0$ eV.** (a) Electrical conductance, $G(T)$; (b) Seebeck coefficient, $S(T)$; (c) thermal conductance, κ_e ; (d) electronic figure of merit, $ZT_e(T)$.

When the thermal conductance due to the phonons κ_{ph} is included[31], the full $ZT = S^2GT/(\kappa_e + \kappa_{ph})$ [32] and only this is physically relevant. In order to compute κ_{ph} to the thermal conductance, we calculate the transmission coefficient of phonon $T_{ph}(\hbar\omega)$ as a function of their frequency ω , according to Eq. 4.7-4.8. Since the highest ZT occurs when κ_{ph} is less than or comparable with κ_e , we focus initially on the highest conductance molecule DPP1-a, with its phonon transmission coefficient and thermal conductance due to the phonons being presented in Figures 4.2.9a,b. The phononic thermal conductances are found to be 16.9

and 8 pW/K for DPP2-a and DPP2-b, respectively in Figure 4.2.10. For DPP1-a Figure 4.2.9c shows the room-temperature full ZT versus the Fermi energy and demonstrates a high room-temperature $ZT \sim 1.5$ is achievable. Figure 4.2.9d shows the temperature dependence of ZT for all molecules and reveals that the ZT of DPP1 can reach ~ 2 when the temperature increases to 400K.

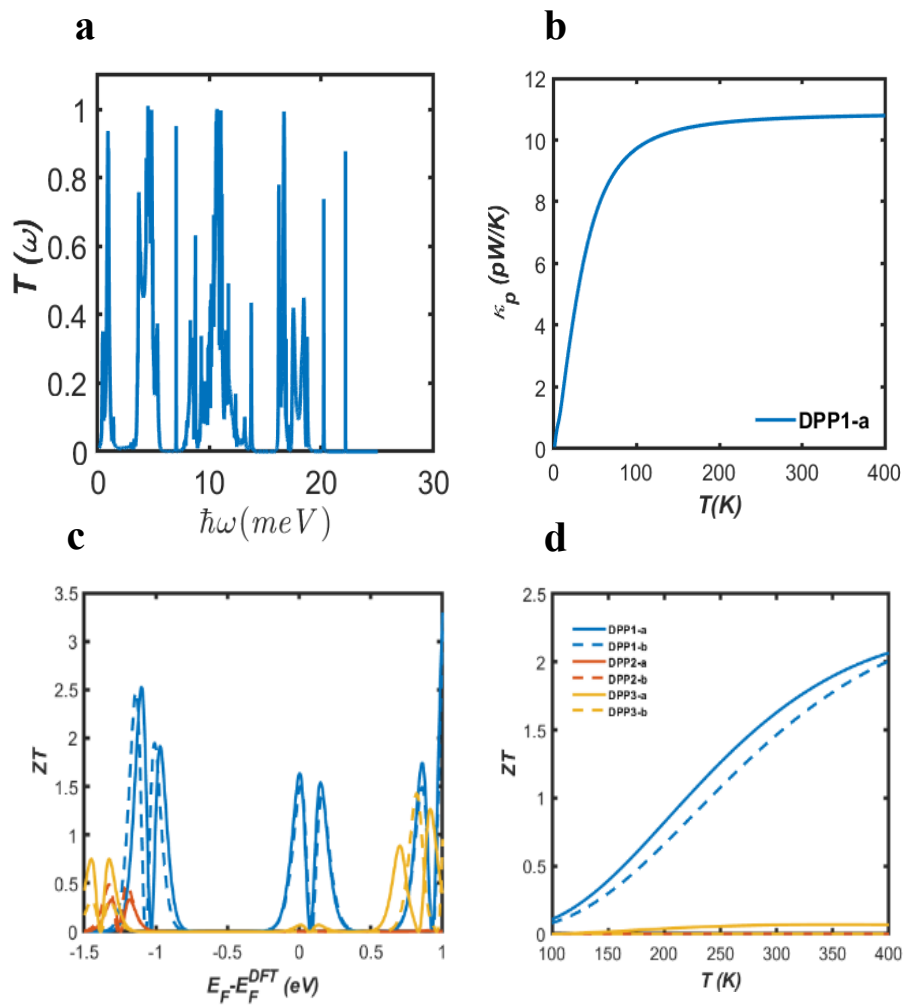


Figure 4.2.9. **Thermoelectric properties of the molecules.** (a) Phonon transmission function for DPP1-a; (b) phononic contribution to the thermal conductance for DPP1-a; (c) full ZT as a function of Fermi energy at room temperature 300 K for molecules shown in Figure 1a; (d) full ZT as a function of temperature for molecules shown in Figure 4.1a.

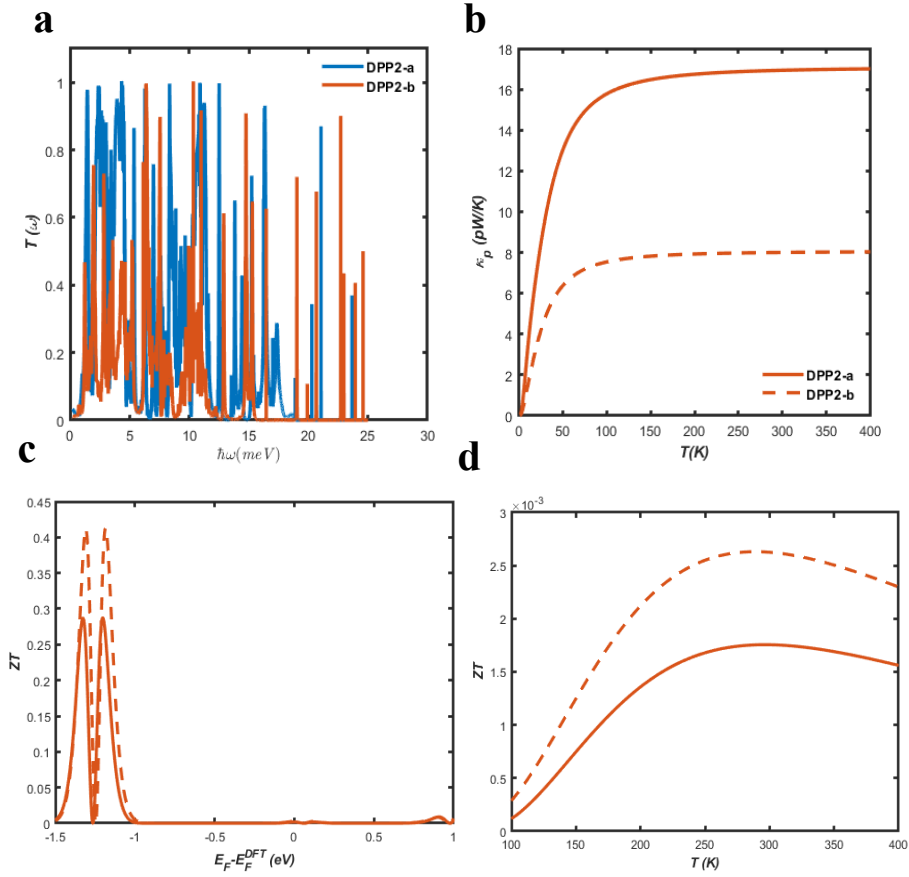


Figure 4.2.10. **Thermoelectric properties of the molecules DPP2-a,b.** (a) Phonon transmission function; (b) phononic contribution to the thermal conductance; (c) full ZT as a function of Fermi energy at room temperature 300 K; (d) full ZT as a function of temperature.

However, the molecules exhibiting DQI show quite low values of the full ZT , because k_{ph} dominates the electronic contribution. DPP2-/3-b have the lowest electrical conductances and the highest Seebeck coefficients. The electronic figure of merit is $ZT_e = GS^2T/\kappa_e$, and therefore, if phonons are neglected and provided the Wiedemann–Franz law is valid (i.e., $\frac{G}{\kappa_e} =$ constant), the molecules with the highest S will have the highest ZT_e . However, this means

that the low- G molecules have low values of κ_e and therefore after including the phonons the percentage increase in thermal conductance is greatest for low- G molecules. This is why molecules with high ZT_e have a low ZT . More quantitatively, the thermal conductance due to phonons is of order $\kappa_{ph} = 8pW/K$, whereas for the low- G molecules DPP2-b and DPP3-b, $\kappa_e \approx 10^{-4}pW/K$. Consequently, phonons dominate their thermal conductance and their full ZT is low. For the CQI molecules DPP1-a/-b where $\kappa_{ph} = 11pW/K$ and $\kappa_e = 32pW/K$, the full ZT is higher, because phonons have a much smaller effect on the thermal conductance. Figure 4.2.11 shows that a similar temperature dependence is obtained if the Fermi energy deviates from the DFT-predicted value by -0.1 eV.

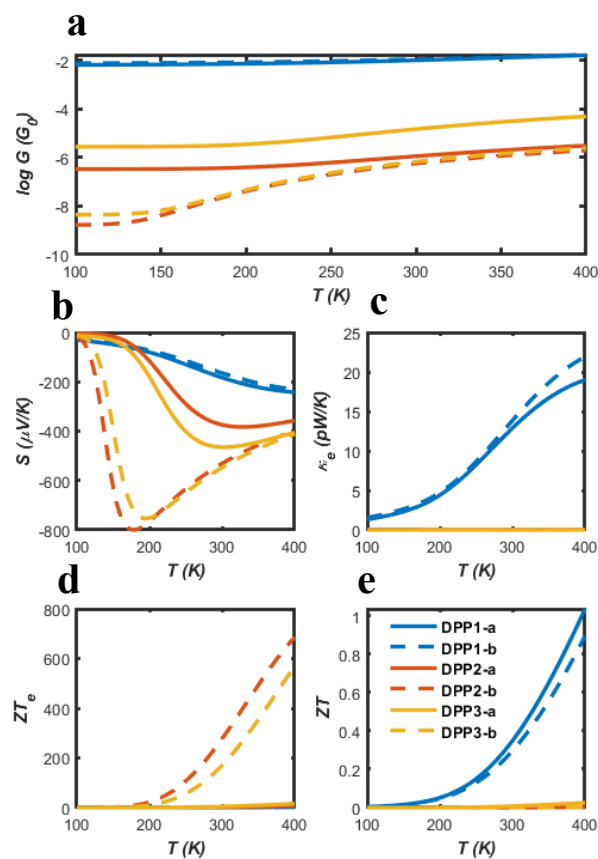


Figure 4.2.11. **Thermoelectric properties of the molecules as a function of temperature for DPP- derivatives.** (a-e) the electrical conductance G , Seebeck coefficients $S(T)$, thermal

conductance κ_e , electronic figure of merit $ZT_e(T)$ and full ZT as a function of temperature at Fermi-energy $E_F = -0.1$ respectively.

Starting from the above molecular junctions, we consider the possibility of tuning their electrical and thermoelectrical properties, by doping with TCNQ[21][33] to form charge-transfer complexes. Our aim is to investigate the influence of the presence of TCNQ acceptor molecule on the transmission coefficient of the DPP derivatives in Figure 4.1a. As an example, we chose DPP1, because the undoped molecule has the highest T . Starting from this high value, the aim is to determine if it is possible to increase ZT even further. DPP1-a and DPP1-b have the same central core and will bind to TCNQ in the manner. The results in Figure 4.2.12b show that TCNQ gains electrons from the backbone, which induces negative gating on the backbone DPP1-b. Consequently, spin polarized transport is observed due to the charge transfer from the DPP1-b to TCNQ. In addition, the two Fano-resonances are generated due to the weak coupling between the acceptor and donor, so that the acceptor behaves like a pendant group[34][35]. Then, if we replaced sulphur atom with oxygen, there is no significant difference in the behaviour of the transmission coefficient as shown in Figure 4.2.13. For the DPP1-b+TCNQ complex, we computed the thermoelectric properties, the electrical conductance, the Seebeck coefficient and the full ZT by using an estimated k_{ph} value equal to 10 pW K^{-1} . In the range between the two vertical dashed lines in Figure 4.2.12d, the Seebeck coefficients are positive, which indicates that the sign is tuned by TCNQ doping. The full ZT is around 0.1 which is suppressed compared to the undoped junction.

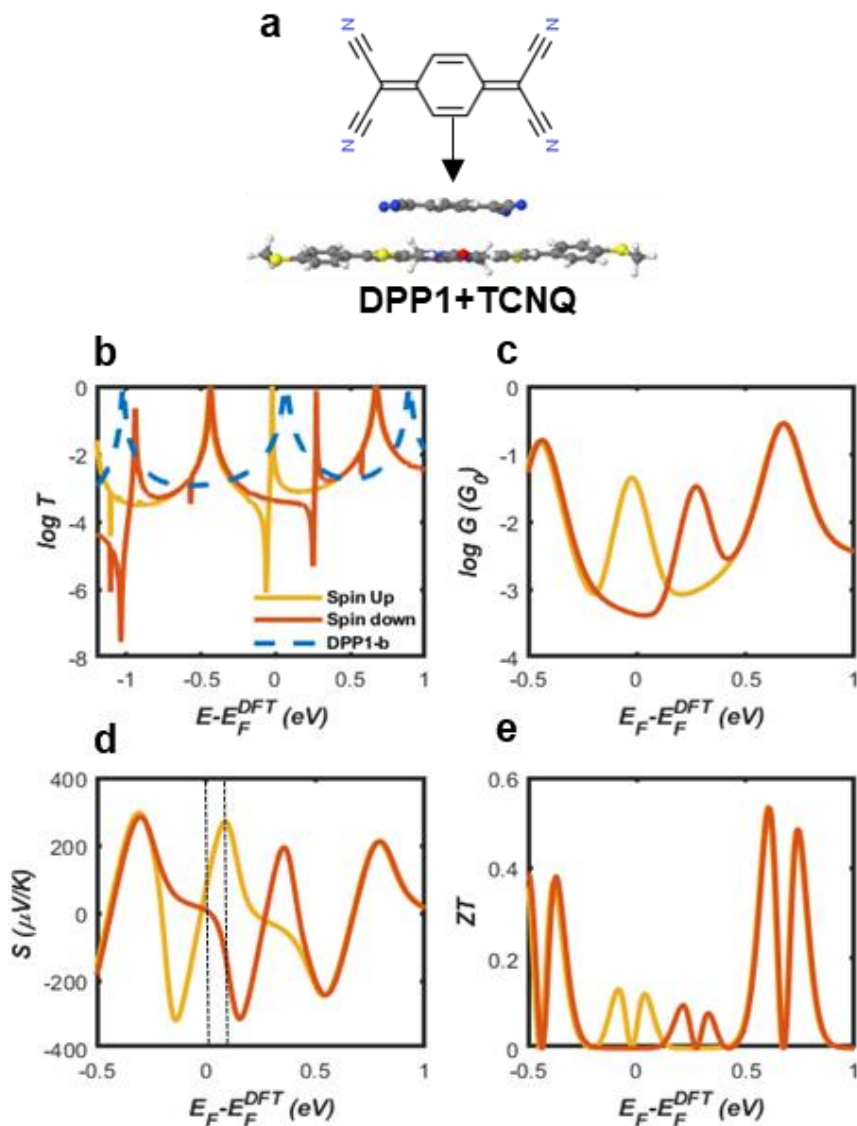


Figure 4.2.12. **DFT-based transmission functions for DPP1-b+TCNQ.** (a) Configuration of the system containing a single molecule DPP1 with TCNQ; (b) transmission coefficients against Fermi energy, E_F (blue curve, the transmission functions of DPP1-b; red and yellow curves, spin up and spin down transmission functions of the donor-acceptor charge-transfer complex, respectively); (c) Electrical conductance G ; (d) Seebeck coefficients, S ; (e) room-temperature ZT versus Fermi energy.

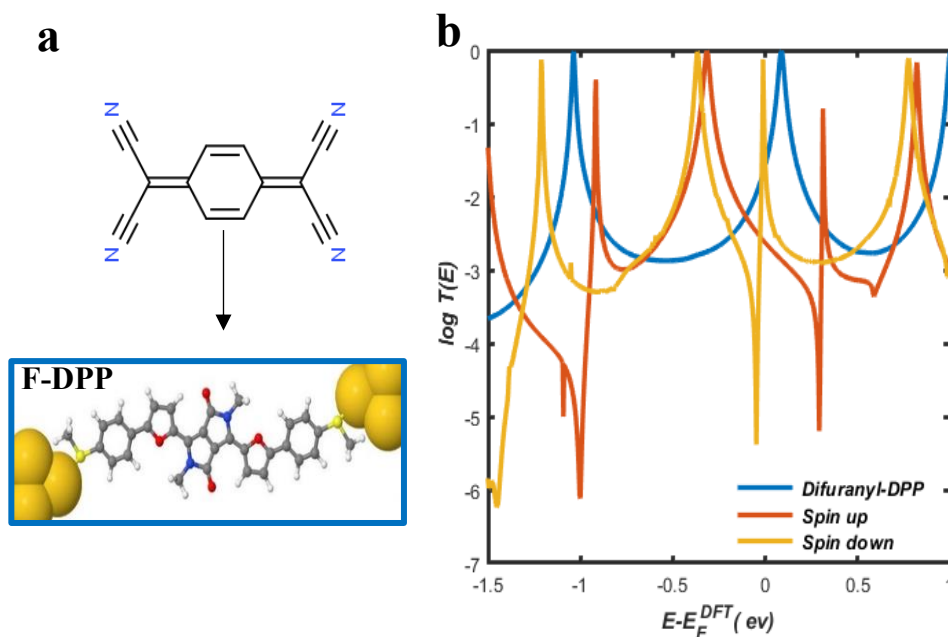


Figure 4.2.13. **DFT-based transmission functions of Difuranyl-DPP with TCNQ.** (a,b) an example of an optimized configuration of the system containing a single molecule Difuranyl-DPP (F-DPP) with TCNQ; (b) transmission coefficients against Fermi energy, E_F (blue curve, the transmission functions of F-DPP, red and yellow curves, spin up and spin down transmission functions of the donor-acceptor charge-transfer complex, respectively).

4.3. Conclusion

On the basis of density functional theory and the quantum transport theory, the electron transport properties have been investigated for thiophene-DPP derivatives (DPP1, DPP2, and DPP3). This work illustrates that varying the position of the sulphur atom in thiophene rings has a significant influence on their electrical and thermoelectric properties. It is further verified by studying the connectivity of the two-thiophene-ring systems in the absence of DPP core. In addition, the rotation of the flanked rings could cause huge variations in the conductance when inserting the DPP core into the two-thiophene system. Furthermore, DQI molecules 2 and 3 systems show high Seebeck coefficients, which could reach 500 – 700 $\mu\text{V}/\text{K}$. After including the contribution from phonons to the thermal conductance, we found that, due to the presence of CQI, the full ZT of DPP1 reaches 1.5 at room temperature and could increase to 2 when

temperature elevates to 400 K. Finally, we demonstrated that the Seebeck could be further tuned by introducing a TCNQ dopant which could gain electrons from DPP, leading to the sign change for the Seebeck coefficients even though DPP is a stronger acceptor. These results suggest that DPP derivatives are versatile materials for thermoelectric functions, whose performance can be tuned by varying their connectivity to electrodes, changing the positions of sulphur atoms and varying the orientation of their thiophene rings to obtain different isomers.

4.4. Appendix: Supplementary calculations based on thiophene monomers and thiophene dimers

Based on the relaxed thiophene monomer and thiophene dimers shown in Figure 4.2.4a-c, I perform molecular orbitals plots of the HOMOs and LUMOs as shown in table 4.4.1 and table 4.4.2 to further investigate their details in single molecule junction. Then, I will present theoretical calculation using DFT to compute the ground-state energy to calculate the optimum binding distance in section 4.4.2.

4.4.1. Molecular orbitals of thiophene monomer

Table 4.4.1. Molecular orbitals of thiophene monomer, along with their MO energies

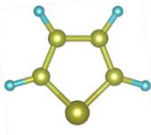
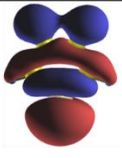
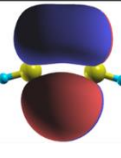
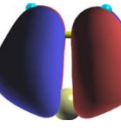
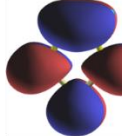
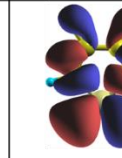
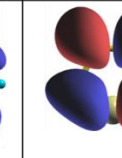
Structure	HOMO-2	HOMO-1	HOMO	LUMO	LUMO+1	LUMO+2
						
$E_F(\text{eV}) = -3.82$	-8.01(eV)	-5.75(eV)	-5.38(eV)	-0.94(eV)	0.46(eV)	0.78(eV)

Table 4.4.1. Shows the frontier orbital of thiophene monomer, where are delocalized on the structure. Based on the discussion in chapter 3 for the Green's function and frontier molecular orbitals, from the HOMO and LUMO orbitals it is clear that para connection to the thiophene ring leads to CQI. Therefore, DPP1-a,b have the higher electrical conductance than others.

4.4.2. Binding energy of thiophenes

The next step is to understand how the thiophene monomer and thiophene dimer attach to the surface of the gold electrodes by modelling STM-Break junction measurements. This allows to calculate the optimum binding distance for geometries S1 and S1' as shown in Figure 4.2.4a and 4.2.4c between two gold surfaces, which is forming a 'pyramidal' tip (111), in this calculation the gold leads consist of 3 layers of 25 atoms. I used SIESTA and the counterpoise method, which removes basis set superposition errors (BSSE) as it discussed in chapter 2. Therefore, I evaluate the binding distance d where d is defined as the distance between the gold surface and carbon atom (Au-C) and between the gold surface and sulphur atom (Au-SMe) at the closest point. Thiophene-molecule is defined as monomer **A** and the gold electrodes as monomer **B**. The energy of individual molecule is then calculated in a fixed basis, which is achieved through the use of ghost atoms in SIESTA. Thus, the binding energy is then calculated using Eq. 2.18, where the minimum binding energy for (Au-C) occurs at distance d is 2\AA with a binding energy of approximately -3.1 eV and the minimum binding energy for (Au-SMe) occurs at distance d is 2.6\AA with a binding energy of approximately -0.41 eV as shown in Figure 4.4.1 -4.4.2 respectively.

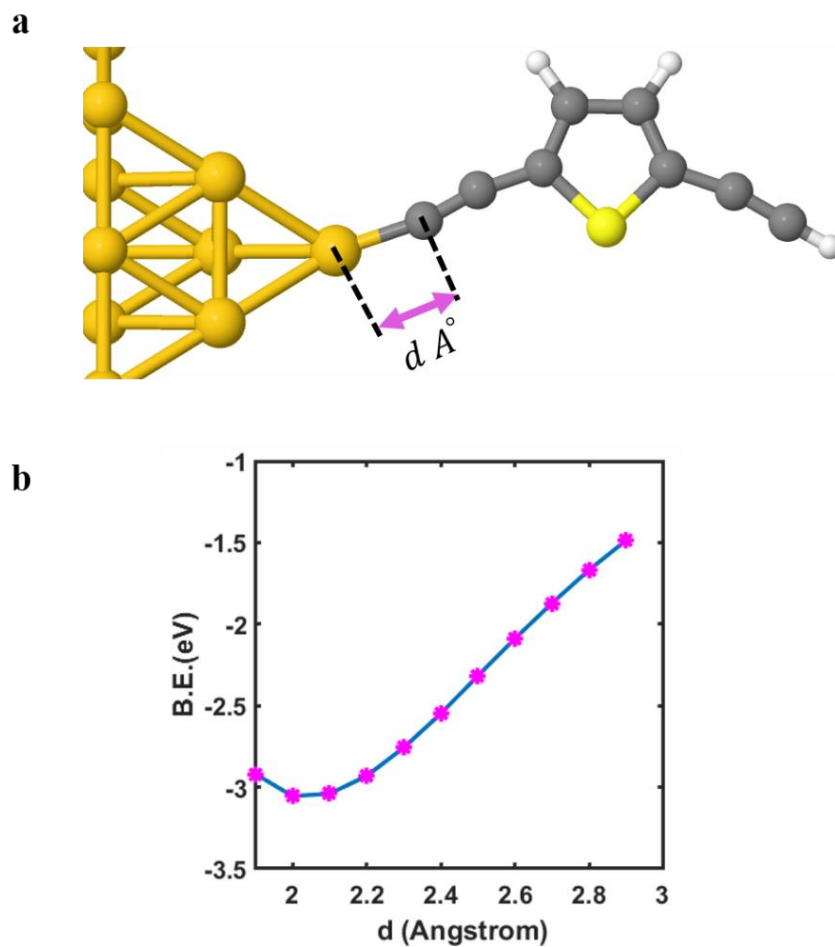


Figure 4.4.1. **DFT-based binding energies as a function of the distance A° .** (a) Orientation of the molecular with respect to the gold lead; (b) Binding energies as a function of the distance d .

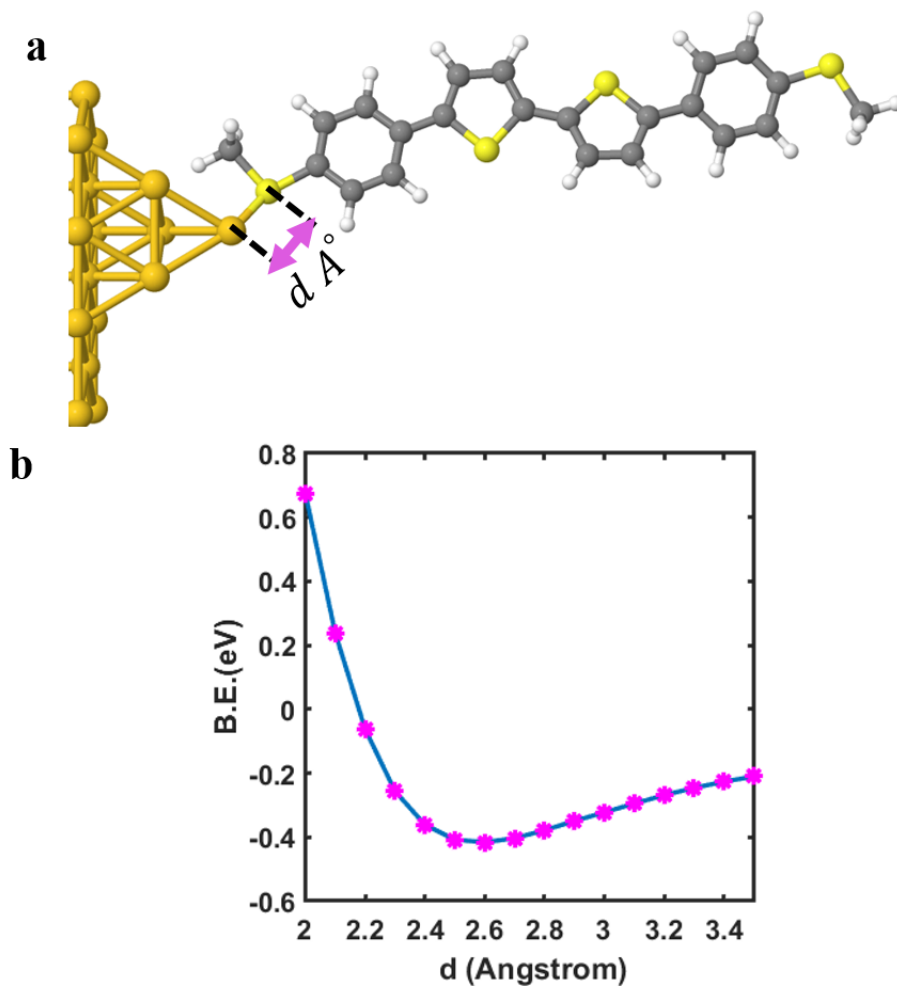
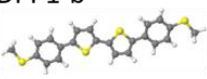
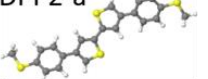
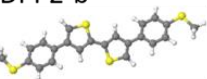
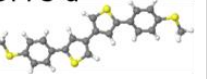
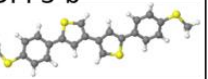
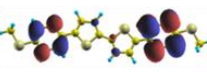
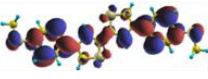
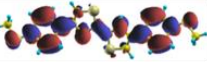
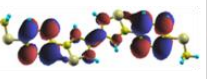
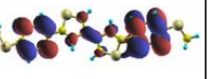
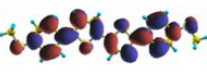
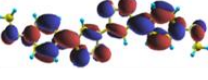
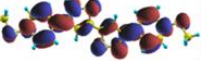
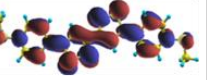
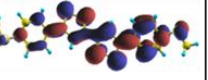
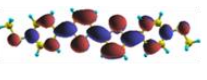
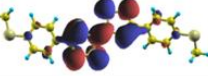
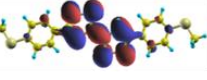
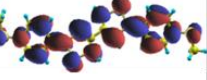
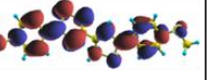
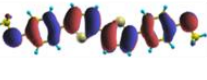
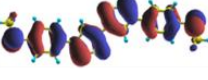
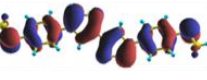
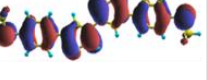
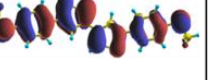
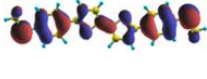

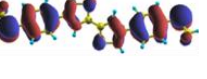
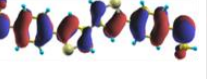
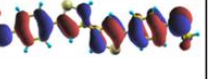
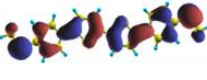
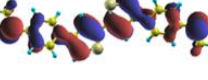
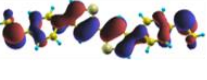
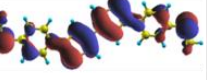
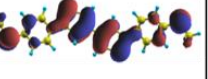


Figure 4.4.2. **DFT-based binding energies as a function of the distance A° .** (a) Orientation of the molecular with respect to the gold lead; (b) Binding energies as a function of the distance d .

4.4.3. Molecular orbitals of thiophene dimers with different connectivities

Table 4.4.2. Molecular orbitals of thiophene dimers with different connectivities, along with their MO energies

	DPP1-b 	DPP2-a 	DPP2-b 	DPP3-a 	DPP3-b 
E_F (eV)	-3.16	-3.041	-3.044	-2.88	-2.77
LUMO+2 					
E (eV)	-1.04	-1.13	-1.08	-1.08	-1.06
LUMO+1 					
E (eV)	-1.36	-1.34	-1.33	-1.56	-1.63
LUMO 					
E (eV)	-2.16	-1.80	-1.82	-1.65	-1.69
HOMO 					
E (eV)	-4.06	-4.358	-4.352	-4.36	-4.33
HOMO-1 					
E (eV)	-4.66	-4.545	-4.547	-4.49	-4.46
HOMO-2 					
E (eV)	-5.18	-4.892	-4.875	-5.02	-5.07

Bibliography

- [1] N. T. Xu, Bingqian, “Single-Molecule Resistance Measured by Repeated Formation of Molecular Junctions,” *Science* (80-.), vol. 301, pp. 1221–1223, 2003.
- [2] T. Sendler *et al.*, “Light-Induced Switching of Tunable Single-Molecule Junctions,” *Adv. Sci.*, vol. 2, pp. 1500017, 2015.
- [3] C. Lambert, “Basic concepts of quantum interference and electron transport in single-molecule electronics,” *Chem. Soc. Rev.*, vol. 44, no. 4, pp. 875–888, 2015.
- [4] Q. Wu, S. Hou, H. Sadeghi, and C. Lambert, “A single-molecule porphyrin-based switch for graphene nano-gaps,” *Nanoscale*, vol. 10, pp. 6524–6530, 2018.
- [5] F. Moresco, G. Meyer, K.-H. Rieder, H. Tang, A. Gourdon, and C. Joachim, “Conformational changes of single molecules induced by scanning tunneling microscopy manipulation: A route to molecular switching,” *Phys. Rev. Lett.*, vol. 86, no. 4, pp. 672–675, 2001.
- [6] A. J. Kronemeijer *et al.*, “Reversible conductance switching in molecular devices,” *Adv. Mater.*, vol. 20, no. 8, pp. 1467–1473, 2008.
- [7] A. Aviram and M. A. Ratner, “Molecular rectifiers,” *Chem. Phys. Lett.*, vol. 29, no. 2, pp. 277–283, 1974.
- [8] W. Xu *et al.*, “Unusual Length Dependence of the Conductance in Cumulene Molecular Wires,” *Angew. Chemie*, vol. 58, pp. 8378–8382, 2019.
- [9] S. Hou, Q. Wu, H. Sadeghi, and C. J. Lambert, “Thermoelectric properties of oligoglycine molecular wires,” *Nanoscale*, vol. 11, no. 8, pp. 3567–3573, 2019.
- [10] Q. Wu, H. Sadeghi, V. M. García-Suárez, J. Ferrer, and C. J. Lambert,

- “Thermoelectricity in vertical graphene-C60-graphene architectures,” *Sci. Rep.*, vol. 7, p. 11680, 2017.
- [11] A. Ismael *et al.*, “Tuning the thermoelectrical properties of anthracene-based self-assembled monolayers,” *Chem. Sci.*, vol. 11, no. 26, pp. 6836–6841, 2020.
- [12] Q. Zhang, Y. Sun, W. Xu, and D. Zhu, “Organic Thermoelectric Materials: Emerging Green Energy Materials Converting Heat to Electricity Directly and Efficiently,” *Adv. Mater.*, vol. 26, no. 40, pp. 6829–6851, 2014.
- [13] J. A. Malen, S. K. Yee, A. Majumdar, and R. A. Segalman, “Fundamentals of energy transport, energy conversion, and thermal properties in organic-inorganic heterojunctions,” *Chem. Phys. Lett.*, vol. 491, no. 4–6, pp. 109–122, 2010.
- [14] D. G. Farnum, G. Mehta, G. G. I. Moore, and F. P. Siegal, “Attempted reformatskii reaction of benzonitrile, 1,4-diketo-3,6-diphenylpyrrolo[3,4-C]pyrrole. A lactam analogue of pentalene,” *Tetrahedron Lett.*, vol. 15, no. 29, pp. 2549–2552, 1974.
- [15] M. Grzybowski and D. T. Gryko, “Diketopyrrolopyrroles: synthesis, reactivity, and optical properties,” *Adv. Opt. Mater.*, vol. 3, no. 3, pp. 280–320, 2015.
- [16] X. Wang, B. Jiang, C. Du, X. Ren, Z. Duan, and H. Wang, “Fluorinated dithienyl-diketopyrrolopyrrole: a new building block for organic optoelectronic materials,” *New J. Chem.*, vol. 43, no. 41, pp. 16411–16420, 2019.
- [17] Q. Liu, S. E. Bottle, and P. Sonar, “Developments of Diketopyrrolopyrrole-Dye-Based Organic Semiconductors for a Wide Range of Applications in Electronics,” *Advanced Materials*. vol. 32, p. 1903882, 2020.
- [18] Z. Wang *et al.*, “Charge Mobility Enhancement for Conjugated DPP-Selenophene Polymer by Simply Replacing One Bulky Branching Alkyl Chain with Linear One at

- Each DPP Unit,” *Chem. Mater.*, vol. 30, no. 9, pp. 3090–3100, 2018.
- [19] J. Ding *et al.*, “Selenium-Substituted Diketopyrrolopyrrole Polymer for High-Performance p-Type Organic Thermoelectric Materials,” *Angew. Chemie - Int. Ed.*, vol. 58, no. 52, pp. 18994–18999, 2019.
- [20] D. S. Acker *et al.*, “7,7,8,8-Tetracyanoquinodimethane and its electrically conducting anion-radical derivatives,” *J. Am. Chem Soc.*, vol. 82, no. 24, pp. 6408–6409, 1960.
- [21] F. Herman and I. P. Batra, “Electronic structure of the tetracyanoquinodimethane (TCNQ) molecule,” *Phys. Rev. Lett.*, vol. 33, no. 2, pp. 94–97, 1974.
- [22] J. M. Soler *et al.*, “The SIESTA method for ab initio order-N materials simulation,” *J. Phys. Condens. Matter*, vol. 14, no. 11, pp. 2745–2779, 2002.
- [23] J. P. Perdew, K. Burke, and M. Ernzerhof, “Generalized gradient approximation made simple,” *Phys. Rev. Lett.*, vol. 77, no. 18, pp. 3865–3868, 1996.
- [24] J. Ferrer *et al.*, “L A GOLLUM: A Next-Generation Simulation Tool for Electron, Thermal and Spin Transport,” *New J. Phys*, vol. 16, p. 93029, 2014.
- [25] L. Venkataraman, J. E. Klare, C. Nuckolls, M. S. Hybertsen, and M. L. Steigerwald, “Dependence of single-molecule junction conductance on molecular conformation,” *Nature*, vol. 442, no. 7105, pp. 904–907, 2006.
- [26] C. M. Finch, S. Sirichantaropass, S. W. Bailey, I. M. Grace, V. M. García-Suárez, and C. J. Lambert, “Conformation dependence of molecular conductance: Chemistry versus geometry,” *J. Phys. Condens. Matter*, vol. 20, no. 2, p. 022203, 2008.
- [27] C. J. Lambert and S. X. Liu, “A Magic Ratio Rule for Beginners: A Chemist’s Guide to Quantum Interference in Molecules,” *Chem. - A Eur. J.*, vol. 24, pp. 4193–4201, 2018.

- [28] K. Yoshizawa, T. Tada, and A. Staykov, "Orbital views of the electron transport in molecular devices," *J. Am. Chem. Soc.*, vol. 130, no. 29, pp. 9406–9413, 2008.
- [29] J. P. Small, K. M. Perez, and P. Kim, "Modulation of thermoelectric power of individual carbon nanotubes," *Phys. Rev. Lett.*, vol. 91, no. 25, p. 256801, 2003.
- [30] A. M. Lunde and K. Flensberg, "On the Mott formula for the thermopower of non-interacting electrons in quantum point contacts," *J. Phys. Condens. Matter*, vol. 17, no. 25, pp. 3879–3884, 2005.
- [31] O. Bubnova and X. Crispin, "Towards polymer-based organic thermoelectric generators," *Energy Environ. Sci.*, vol. 5, pp. 9345–9362, 2012.
- [32] H. Karamitaheri, M. Pourfath, R. Faez, and H. Kosina, "Geometrical effects on the thermoelectric properties of ballistic graphene antidot lattices," *J. Appl. Phys.*, vol. 110, no. 5, p. 054506, 2011.
- [33] M. Rudloff *et al.*, "Charge transfer tuning by chemical substitution and uniaxial pressure in the organic complex tetramethoxypyrene-tetracyanoquinodimethane," *Phys. Chem. Chem. Phys.*, vol. 17, no. 6, pp. 4118–4126, 2015.
- [34] K. Wang *et al.*, "Charge transfer complexation boosts molecular conductance through Fermi level pinning," *Chem. Sci.*, vol. 10, no. 8, pp. 2396–2403, 2019.
- [35] M. Famili, I. M. Grace, Q. Al-Galiby, H. Sadeghi, and C. J. Lambert, "Toward High Thermoelectric Performance of Thiophene and Ethylenedioxythiophene (EDOT) Molecular Wires," *Adv. Funct. Mater.*, vol. 28, no. 15, p. 1703135, 2018.

5. Single-Molecule Charge Transport Modulation Induced by Steric Effects of Side Alkyl Chains

In this chapter, the dependence of intra-molecular conductance on the nature of branching alkyl chains is investigated, through a combination of the scanning tunneling microscope break junction (STM-BJ) technique carried out by collaborators in Xiamen university and density functional theory. Three thiophene-flanked diketopyrrolopyrrole (DPP) derivatives with different branching alkyl chains (isopentane, 3-methylheptane, and 9-methylnonadecane) are used with phenylthiomethyl groups as anchor. This chapter shows that as the alkyl chain becomes longer, the DPP molecular conductance is decreased. Both theoretical simulations and ^1H NMR spectra at the single-molecule level demonstrate that the planarity of the DPPs is directly reduced after introducing longer branching alkyl chains, which leads to the reduced conductance. This chapter indicates that the insulating side chain could be used as gate controls of single-molecule conductance, which is of significance for the design of future organic semiconducting molecules. The results presented in this chapter were published in W. Jiang *et al.*, “Single-Molecule Charge Transport Modulation Induced by Steric Effects of Side Alkyl Chains,” *ChemPhysChem*, 2021.

This work is a collaborative study between (Chinese Academy of Sciences, Lancaster University, and Xiamen University).

5.1. Introduction

The electronic properties of the conjugated molecules play an essential role for organic electronics, which are governed by the electronic structures of the conjugated frameworks and the intermolecular interactions[1][2][3]. It is known that the pendant alkyl chains attached to the conjugated backbone not only improve the solubility, but also influence the intermolecular/inter-chain orderly packing,[4][5][6][7][8] and may also lead to the changes of electronic structure of the conjugated backbone[9][10]. However, it remains challenging to distinguish the contribution of the side-chain on the intramolecular charge transport and the intermolecular packing. For that, the charge transport through the single-molecule diketopyrrolopyrrole (DPP) junctions[11][12][13][14] provides a unique opportunity to study the role of the side-chain on the intramolecular charge transport from the single-molecule level.

In the charge transport investigations through the single-molecule junctions, the conjugated molecules typically possess alkyl chains as soluble groups attached to the periphery of conjugated cores to have solubility for the processing and characterization [15][16][17][18][19][18][20][21][22][23] In some cases, studies suggested that the side-chains attached to the rigid oligo-phenylene-ethynylene (OPE) building blocks lead to no significant changes in the electronic structure of the conjugated backbone, and thus alkyl chains are replaced by methyl groups in most of the combined theoretical investigations[24][25]. However, the role of the side-chains on the conformation control of the conjugated frameworks remained unexplored. Our previous studies had suggested that the backbone planarity and rigidity were improved when we replaced one bulky branching alkyl chain in the diketopyrrolopyrrole (DPP)-based polymers with one linear alkyl chain in each DPP unit[9].

Thus the experimental investigations of DPP-based conjugated molecules may offer new insight into the side chain effects on intramolecular charge transport in π -conjugated molecules.

This chapter aims to show single-molecule conductance studies of three diketopyrrolopyrrole (DPP)-based conjugated molecules **DPP-1/4**, **DPP-2/6**, and **DPP-8/12** with the STM-BJ technique[26], and investigate the side chain effects on their intramolecular charge transport (**Figure 5.2.1**). Compounds **DPP-1/4**, **DPP-2/6**, and **DPP-8/12** possess the same conjugated skeleton and the same anchoring groups (-SCH₃), but they bear different side alkyl chains, with isopentane (1/4), 3-methylheptane (2/6) and 9-methylnonadecane (8/12) linked to the DPP units in **DPP-1/4**, **DPP-2/6**, and **DPP-8/12**, respectively. It is noted that these alkyl chains are widely utilized in the construction of DPP-based organic and polymeric semiconductors[27][28][29]. The results reveal that the single-molecule conductance of **DPP-1/4**, **DPP-2/6**, and **DPP-8/12** decreases in the following order: **DPP-1/4** > **DPP-2/6** > **DPP-8/12**, by increasing the length and bulkiness of alkyl chains. Theoretical studies in combination with ¹H NMR data reveal that the effect of pendant alkyl chains on the conjugated backbone conformation (and planarity), and thus the single-molecule conductance of **DPP-1/4**, **DPP-2/6**, and **DPP-8/12** cannot be neglected. The calculations show that the torsional angles among the conjugated units of **DPP-1/4**, **DPP-2/6**, and **DPP-8/12**, and the respective transmission spectra are varied by changing the side alkyl chains, which correlates with the single-molecule conductance studies. Therefore, the insulating side alkyl chains can be used to manipulate the single-molecule conductance, offering potential applications in single molecular electronic devices.

5.2. Molecular structures:

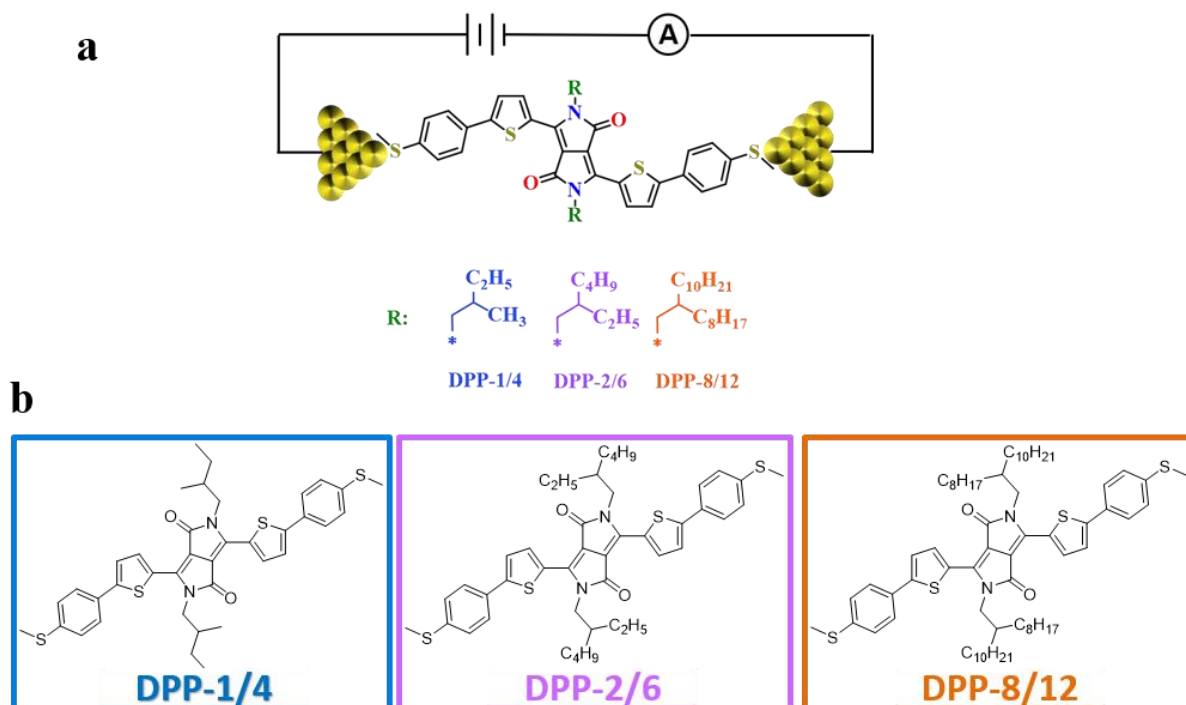


Figure 5.2.1. **Molecular structures.** (a) Schematic of STM-BJ junction; (b) chemical structures of **DPP-1/4**, **DPP-2/6**, and **DPP-8/12** respectively.

5.3. Results and Discussion

In this study, single molecule charge transport in a series of the three DPP molecules, **DPP-1/4**, **DPP-2/6**, and **DPP-8/12**. The two phenylthiomethyl groups in **DPP-1/4**, **DPP-2/6**, and **DPP-8/12** were used as the anchoring groups to connect the respective molecules with the gold electrodes to form single-molecule junctions. The only difference between these molecules is the side alkyl chains. The STM-BJ experimental measurement shows the conductance-displacement curves were recorded shown in Figure 5.3.1a, it can be seen that an obvious plateau appears ranging from $10^{-3} G_0$ to $10^{-5} G_0$ for **DPP-1/4**, **DPP-2/6**, and **DPP-8/12**. The

molecular conductances were obtained by constructed 1D conductance histograms as shown Figure 5.3.1b of **DPP-1/4**, **DPP-2/6** and **DPP-8/12**, which are estimated to be $10^{-3.55} G_0$, $10^{-3.96} G_0$, and $10^{-4.33} G_0$ respectively.

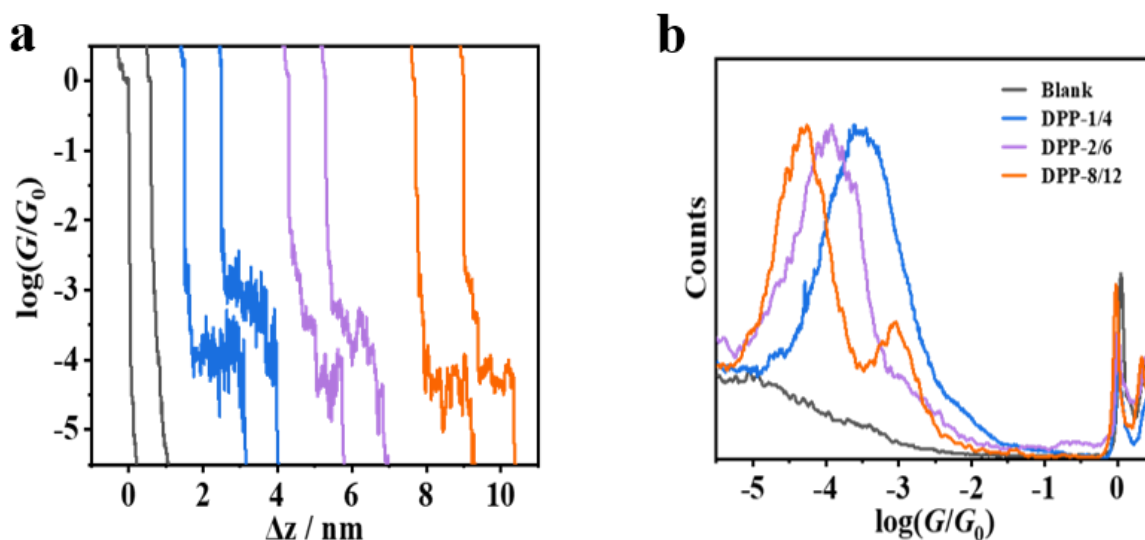


Figure 5.3.1. **The comparison of the conductance of DPP-1/4 (blue), DPP-2/6 (purple) and DPP-8/12 (orange).** (a) Typical individual conductance-displacement curves; (b) 1-D conductance histograms.

Figure 5.3.1 shows that the molecular conductances of **DPP-1/4**, **DPP-2/6** and **DPP-8/12** are dependent on the structures of the side alkyl chains; the molecular conductance decreases gradually by increasing the lengths of alkyl chains. We assume that the different alkyl chains in **DPP-1/4**, **DPP-2/6** and **DPP-8/12** may affect the conformations of the conjugated backbones. Theoretical calculations were carried out at the level of density functional theory in order to understand the effect of side alkyl chains on molecular conductance. We first obtained the fully optimized gas-phase molecules and then built the junctions with molecules attached to two pyramidal-shaped electrodes via SMe anchor groups. In common with calculations presented in chapter 4, the optimized geometry and ground-state Hamiltonian and overlap matrix elements of each structure was self-consistently obtained using SIESTA[30].

The generalized gradient approximation (GGA) of the exchange and correlation functional is used with the Perdew-Burke-Ernzerhof parameterization (PBE)[31] a double- ζ polarized (DZP) basis set, a real-space grid defined with an equivalent energy cut-off of 200 Ry. The geometry optimization for each structure is performed to the forces smaller than 10 meV/Ang. We know the solvent effect would be an important factor which could induce the geometrical changes of the backbone in realistic single-molecule conductance measurements. However, considering the heavy computational expenses, we carried out the investigation in the energetics and the effect of series of manual torsion angles in the backbone for the gas-phase molecules[32].

After the re-optimization of junctions, The mean-field Hamiltonian obtained from the converged DFT calculation or a tight-binding Hamiltonian (using single orbital energy site per atom with Hückel parameterisation) was combined with our home-made implementation of the non-equilibrium Green's function method, GOLLUM[33] to calculate the phase-coherent, elastic scattering properties of the each system consisting of left gold (source) and right gold (drain) leads and the scattering region (molecule **DPP**, **DPP-1/4**, **DPP-2/6**, **DPP-8** and **DPP-8/12**). The transmission coefficient $T(E)$ for electrons of energy E (passing from the source to the drain) is calculated via Eq. 4.1 in chapter 4.

With **DPP-8/12** as an example, the theoretical calculations afforded two stable conformers *A* and *B* (in which the intramolecular S---O interactions are observable where the left and the right sulphur-oxygen distances are 3.2\AA and 2.9\AA respectively, see Figure 5.3.2a) in terms of the positions of the side alkyl chains relative to the conjugated backbone. Between the two conformers, which show different dihedral angles between the conjugated units, conformer *B* is most stable. In conformer *B*, the dihedral angles between the central DPP core

and the left flanking thiophene is 37.3° , and that between the central DPP core and the right flanking thiophene is 23.1° . It is obvious that the conjugated backbone of **DPP-8/12** is twisted.

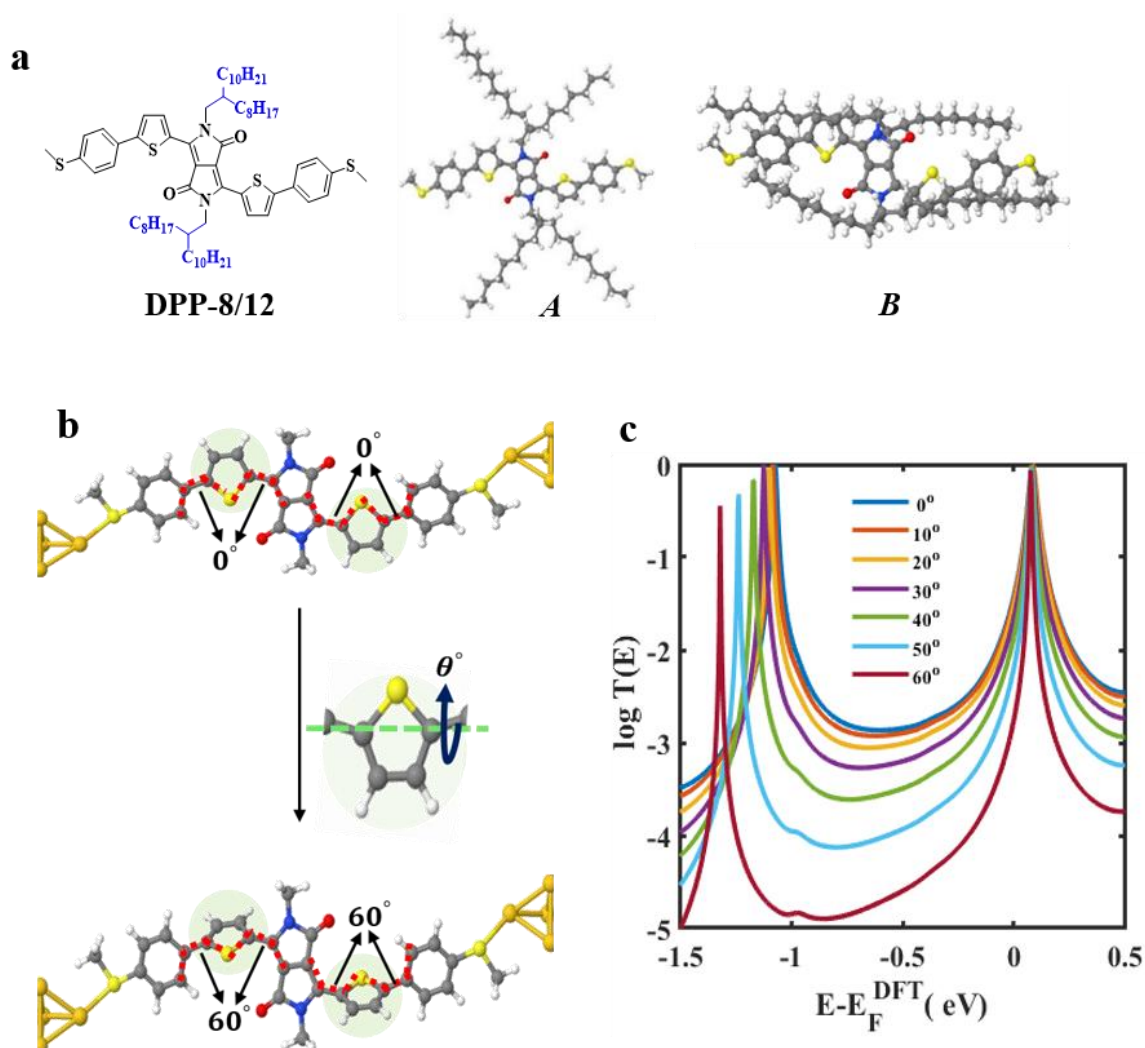


Figure 5.3.2 (a) Conformations of **DPP-8/12** (S---O) in terms of the positions of the alkyl side chains relative to the backbone. Conformer *A* expanded into the nearby space. The dihedral angle between the left thiophene and DPP-core is 25° and between the right thiophene and the core is 18° . *B* is more compact and more energetically stable compared to conformer *A* by 0.62 eV. In this case, the dihedral angles between the left and right thiophenes and the DPP-backbone are 37.3° and 23.1° respectively. (b) Junction formation of the thiophene-DPP core connected to the gold via -SMe with various torsional angles from 0° to 60° between the two planes of left/right flanking thiophene and the rest part of molecule (more conformations shown in Figure 5.3.4). (c) The corresponding transmission functions for molecule DPP-CH₃ displayed in panel b. The blue curve stands for transmission function of the coplanar

conformation (0° dihedral angle, top panel of 5.3.2b), while the other coloured curves represent those of the conformations with torsional angles up to angle 60° (bottom panel of 5.3.2b, see more conformations in Figure 5.3.4).

From the respective transmission coefficients, conformer *A* of **DPP-8/12**, which is more planar than conformer *B*, is predicted to possess a higher molecular conductance than conformer *B* shown in Figure 5.3.3. Moreover, further calculations were performed with conformer *B* in which the two branching alkyl chains were replaced by two methyl groups and the dihedral angles between the central DPP core and flanking thiophenes were manually changed as shown in Figure 5.3.2 b-c. The results show that the molecular conductance decreased gradually by increasing the dihedral angles. The Fermi energy of the system is difficult to be predicted due to the complicated experimental environment, such as the shape of the electrodes and the effect of solvents. However, it is believed that the Fermi energy is located somewhere in the HOMO-LUMO gap. The transmission functions in the whole HOMO-LUMO gap show a decreasing trend. The relationship between the transmission function around middle point of HOMO-LUMO gap and the torsion angle θ follows approximately $T(E, \theta) \propto \cos^6 \theta$ which is not the expected $\cos^8 \theta$ due to several other effects present in the system, e.g. the electrostatic effects between S of thiophene, O of DPP core and H of phenyl ring in ref [19][34]. (see more details in Figure 5.3.5)

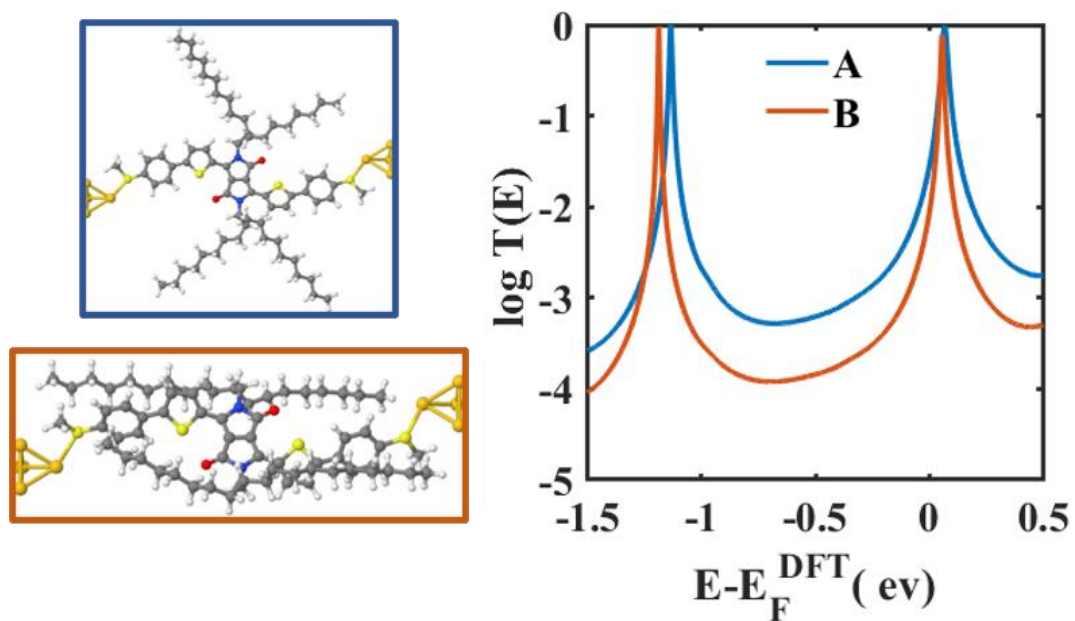


Figure 5.3.3. **DFT-based transmission functions for A and B conformers of DPP-8/12.** Corresponding transmission coefficients against energy relative to the Fermi energy E_F predicted by DFT.

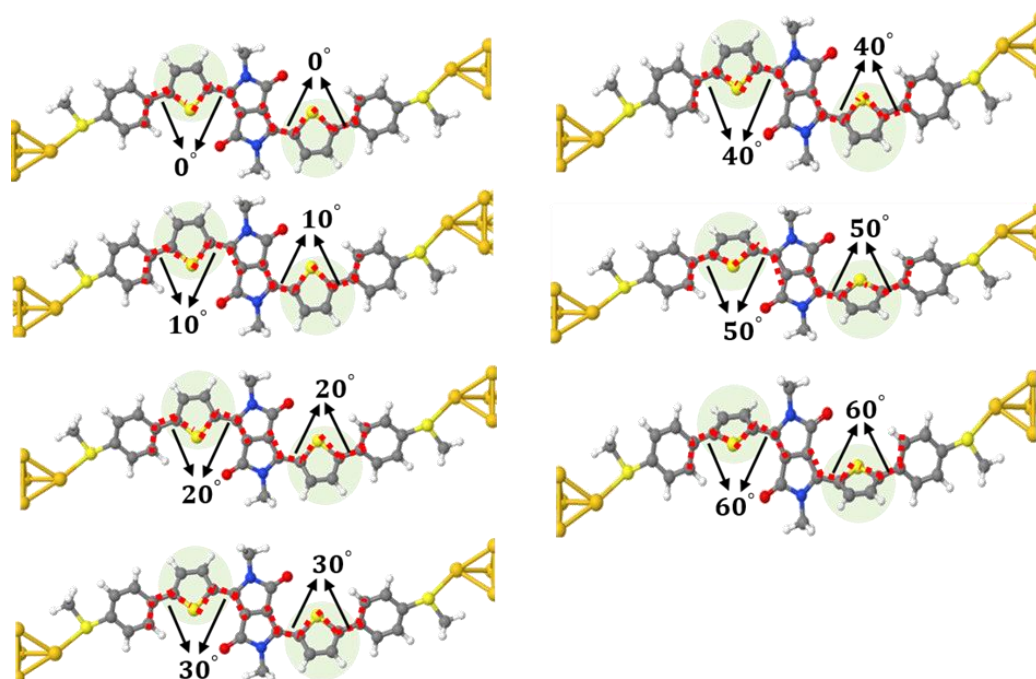


Figure 5.3.4. **Models of single-molecule junctions with various thiophene-ring rotation,** this rotation (indicated by the green shaded regions) angles relative to the rest part of the whole molecule from 10° to 60° (indicated by the dashed red line).

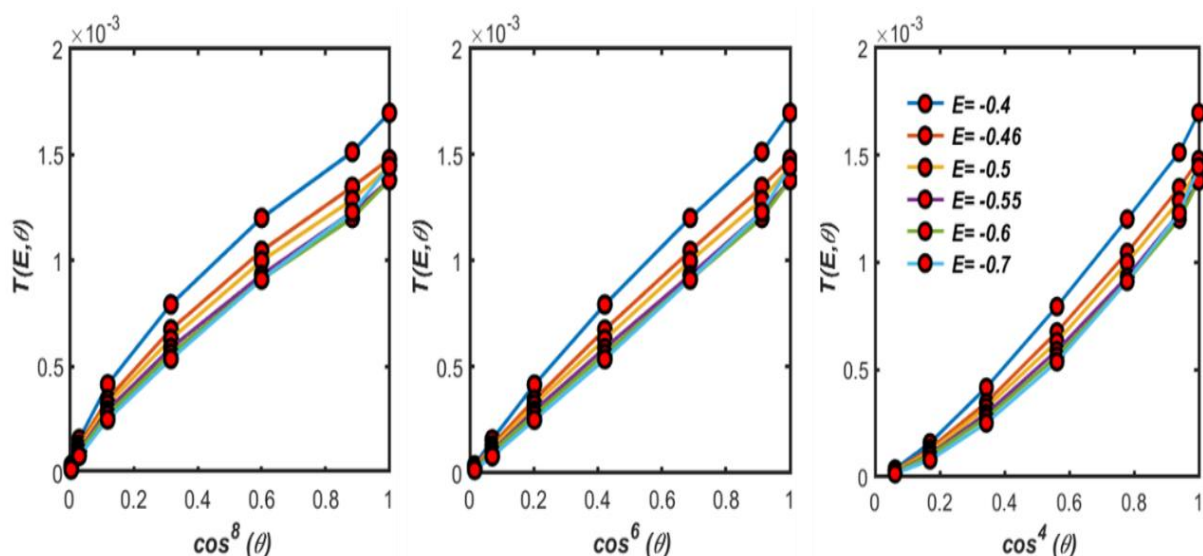


Figure 5.3.5. **Transmission functions of molecular junctions with various thiophene-ring rotation angles θ** (shown in Figure 5.3.4) against $\cos^8 \theta$, $\cos^6 \theta$ and $\cos^4 \theta$ at energy points around the middle of HOMO-LUMO gap, e.g. -0.4, -0.46, -0.5, -0.55, -0.6, -0.7. E is the energy relative to the Fermi energy predicted by DFT. θ is the dihedral angle of the flanking thiophenes relative to the rest part of the whole molecule (indicated by the dashed red lines in Figure 5.3.4).

Similarly, theoretical calculations were performed for **DPP-1/4** and **DPP-2/6**, and for comparison, the calculation was also extended to **DPP-CH₃** in which the alkyl chains are replaced by $-\text{CH}_3$ groups. Table 5.3.1 lists the dihedral angles between the central DPP core and the left/right flanking thiophenes. For **DPP-1/4** and **DPP-CH₃** in which the alkyl chains are short, the conjugated units are almost coplanar. By elongating the alkyl chains as in **DPP-2/6** and **PP-8/12** the dihedral angles become large and thus the conjugated backbones are nonplanar.

Table 5.3.1. The calculated dihedral angles of DPP and flanked thiophenes caused by the presence of alkyl side chains.

Compounds	Torsional angle (°)	
	Left flanking thiophene/DPP	Right flanking thiophene/DPP
DPP-1/4	0.5	4.2
DPP-2/6	19.7	32.9
DPP-8/12	37.3	23.1
DPP-CH₃	3.2	1.1

Therefore, it is expected that **DPP-1/4**, **DPP-2/6** and **DPP-8/12** show different molecular conductances because of the different conformations of their conjugated backbones. Based on their most stable conformers, the respective transmission coefficients were calculated for **DPP-1/4**, **DPP-2/6** and **DPP-8/12** as well as **DPP-CH₃**. The calculation results were shown in Figure 5.3.6, the molecular conductances of **DPP-CH₃**, **DPP-1/4**, **DPP-2/6** and **DPP-8/12** increase in the following order: **DPP-8/12** < **DPP-2/6** < **DPP-1/4** < **DPP-CH₃**. The calculations agree well with the molecular conductances measured experimentally as mentioned above. In short, as the lengths of side alkyl chains increase, the conjugated backbones become nonplanar with enlarging the dihedral angles, leading to the dropping of molecular conductance.

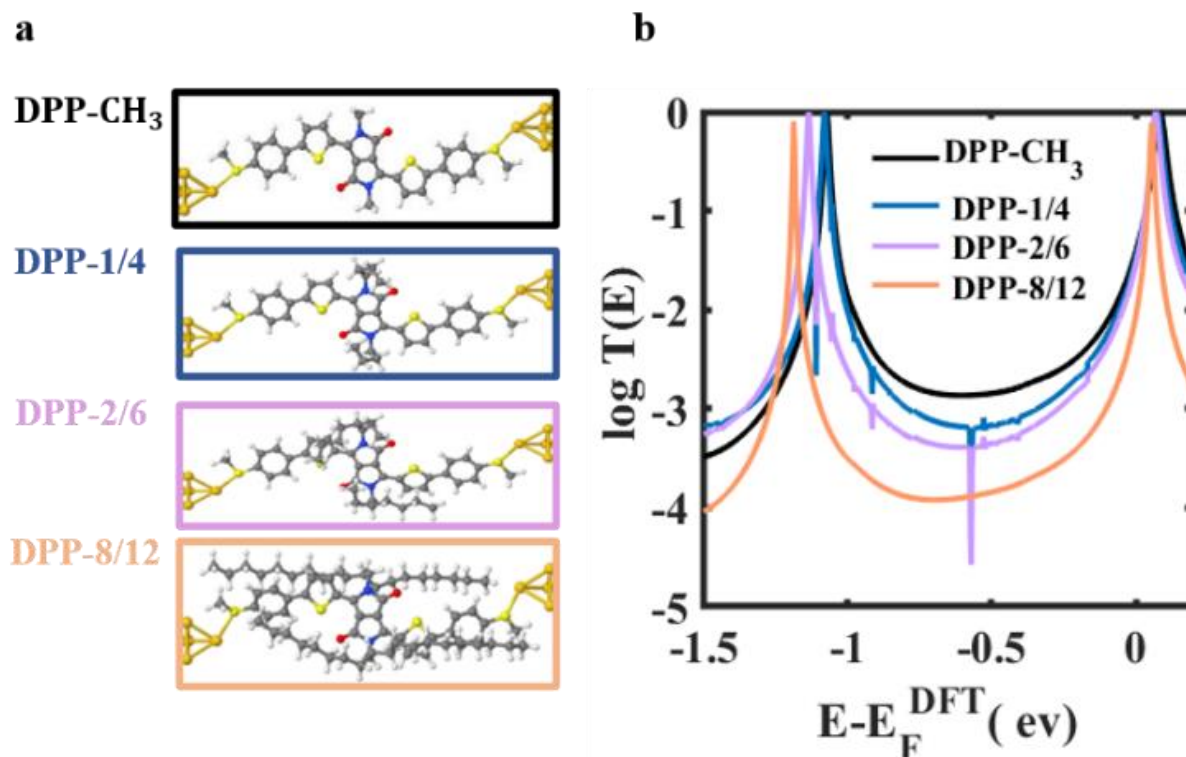


Figure 5.3.6. **DFT-based transmission functions for DPPs (S---O) with three different alkyl side chains.** (a) Optimised junction of the single molecules named as **DPP-CH₃**, **DPP-1/4**, **DPP-2/6** and **DPP-8/12**, respectively; (b) Corresponding transmission coefficients against Fermi energy E_F .

The behaviour in Figure 5.3.6 is confirmed by STM-BJ technique measurements which has been carried out in Xiaman University. The molecular conductances of **DPP-1/4**, **DPP-2/6** and **DPP-8/12** are estimated to be $10^{-3.55} G_0$, $10^{-3.96} G_0$, and $10^{-4.33} G_0$ respectively.

Alternatively, **DPP-8/12** can also adopt stable conformers such as *A'* and *B'* shown in Figure 5.3.8 in which short interatomic contact exists between the oxygen atoms of the central DPP core and the hydrogen atoms of the flanking thiophenes (i.e. intramolecular H---O interactions are observable)[35][36][37]. Conformer *B'* in which the alkyl chains are close to the conjugated backbone is more stable in energy than *A'*, but its backbone becomes more twisted.

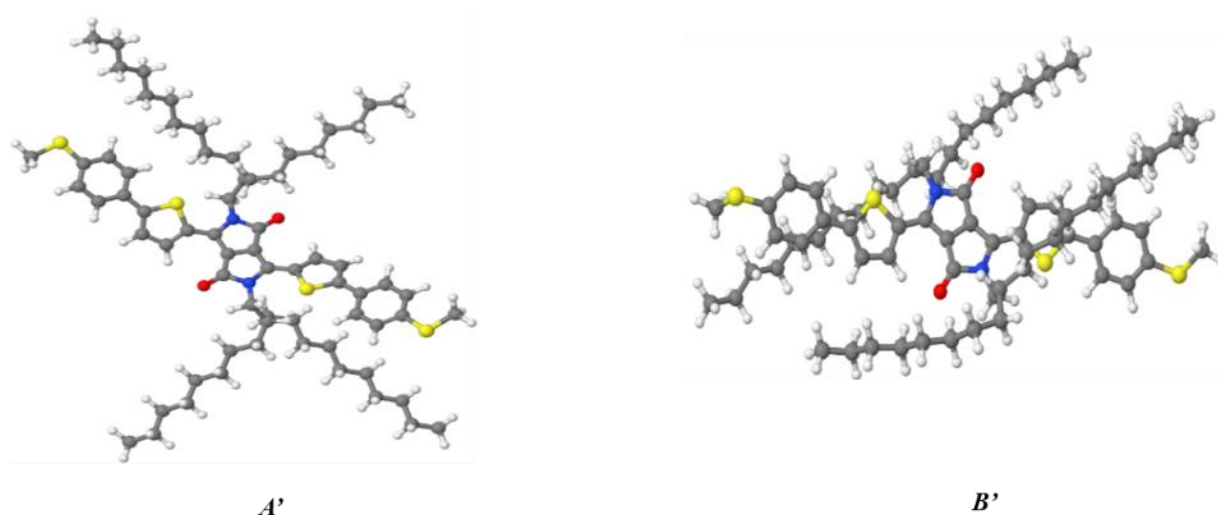


Figure 5.3.8. Conformations of DPP-8/12 in terms of different positions alkyl side chains relative to the DPP core where *A'* is sticking out into space with the left side of dihedral angle between the thiophenes and DPP-core is 8° and the right side is 8.9° , *B'* is stacked with the DPP-backbone of the molecule space and more energetically stable compared to conformer *A'* by 0.55 eV with the left side of dihedral angle between the thiophenes and DPP-core is 19.7° and the right side is 12.1° .

In comparison, the optimized geometry of the analogue molecule in which the alkyl chains are replaced by the methyl groups is more planar. Further calculations of transmission coefficients show that conformer *B'* has a low molecular conductance as shown in Figure 5.3.9. Subsequently, we performed calculations by keeping the backbone conformation of *B'* and substituting the long alkyl chains with $-\text{CH}_3$ groups.

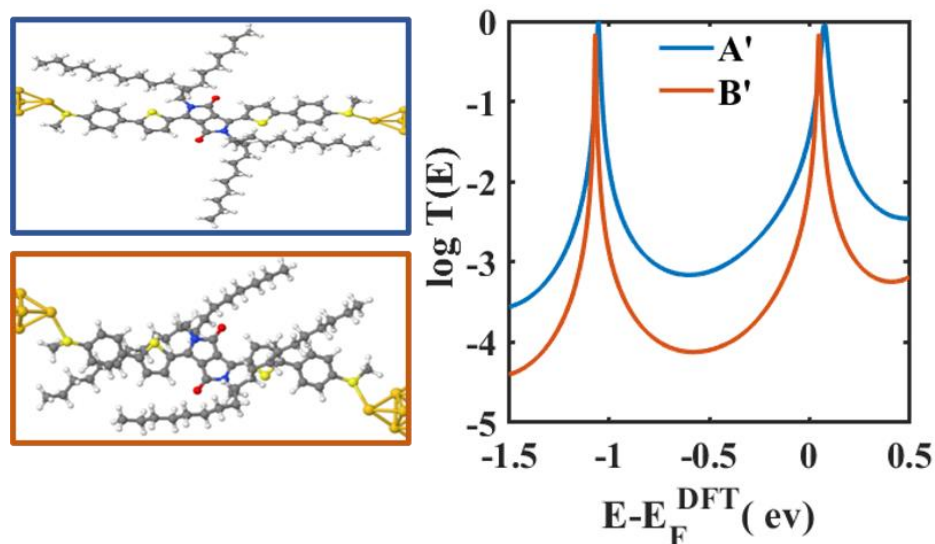


Figure 5.3.9. **DFT-based transmission functions for A' and B' conformers of DPP-8/12. Corresponding transmission coefficients against energy relative to the Fermi energy E_F predicted by DFT.**

It is clear when the long alkyl chains are removed, while retaining the same conformation, the electrical conductance does not change (red and yellow curves in Figure 5.3.10), which reveals that the alkyl chains make no direct contribution to molecular conductance.

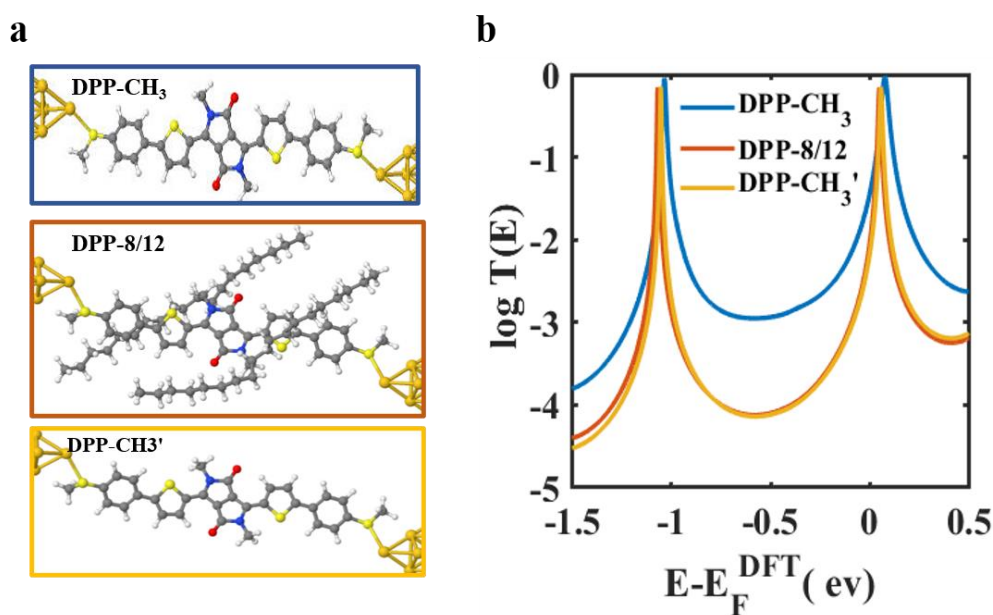


Figure 5.3.10. (a) Models of single-molecule junctions with DPP molecules (O-H) in different geometrical changes, (Top panel: rather planar **DPP-CH₃** molecule after geometrical

optimization. Middle panel: molecule with a twisted backbone induced by the alkyl side chains (**DPP-8/12**), Bottom panel: molecule **DPP-CH₃'** with replaced methyl group for the long alkyl chains and the backbone unchanged based on the structure in Middle panel. (b) Transmission spectra in units of quantum conductance $G_0 = 77 \mu\text{s}$ against Fermi energy E_F relative to the predicted value E_F^{DFT} by DFT.

These calculations show i) the conformation of conjugated backbones of these DPP molecules is affected by the structures of side alkyl chains, and the dihedral angles among the conjugated units are enlarged by elongating the alkyl chains, and ii) consequently the effect of alkyl chains on the molecular conductance cannot be neglected for these DPP molecules and the molecular conductance becomes low by increasing the lengths of side alkyl chains. Mayor and their coworkers previously reported single-molecule junction towards biphenyl systems with controlled torsion angles[38]. But, the alkyl chains were used as the bridging chains to connect biphenyl molecules at 2,2'-positions, which are different from the side alkyl chains discussed in this work.

5.4. Conclusion

In this chapter, with colleagues from Xiamen University, I investigated the changes in intramolecular conductance induced by varying the branching alkyl chains through a combination of the STM-BJ technique and DFT simulations. Three thiophene-flanked DPP derivatives with different branching alkyl chains of isopentane, 3-methylheptane, and 9-methylnonadecane were used, and phenylthiomethyl groups were used as anchors. The STM-BJ results show that as the alkyl chain becomes larger, the resulting molecular conductance is decreased. Both theoretical simulations and ^1H NMR spectra demonstrate that the planarity of the DPPs is directly reduced after introducing longer branching alkyl chains, causing reduced conductance. This work demonstrates that insulating side chains' effect on single-molecule conductance cannot be neglected, and should be considered for the design of future organic semiconducting

materials. The calculated torsional angles increase in the following order: **DPP-1/4** < **DPP-2/6**
< **DPP-8/12**

Bibliography

- [1] V. Coropceanu, J. Cornil, D. A. da Silva Filho, Y. Olivier, R. Silbey, and J.-L. Brédas, “Charge transport in organic semiconductors,” *Chem. Rev.*, vol. 107, no. 4, pp. 926–952, 2007.
- [2] Z. Shuai, H. Geng, W. Xu, Y. Liao, and J.-M. André, “From charge transport parameters to charge mobility in organic semiconductors through multiscale simulation,” *Chem. Soc. Rev.*, vol. 43, no. 8, pp. 2662–2679, 2014.
- [3] R. Noriega *et al.*, “A general relationship between disorder, aggregation and charge transport in conjugated polymers,” *Nat. Mater.*, vol. 12, no. 11, pp. 1038–1044, 2013.
- [4] Y. Yang, Z. Liu, G. Zhang, X. Zhang, and D. Zhang, “The Effects of Side Chains on the Charge Mobilities and Functionalities of Semiconducting Conjugated Polymers beyond Solubilities,” *Adv. Mater.*, vol. 31, no. 46, pp. 1903104, 2019.
- [5] T. Lei, J.-Y. Wang, and J. Pei, “Roles of flexible chains in organic semiconducting materials,” *Chem. Mater.*, vol. 26, no. 1, pp. 594–603, 2014.
- [6] J. Mei and Z. Bao, “Side chain engineering in solution-processable conjugated polymers,” *Chem. Mater.*, vol. 26, no. 1, pp. 604–615, 2014.
- [7] P. Zhan *et al.*, “Side chain length affects backbone dynamics in poly (3-alkylthiophene)s,” *J. Polym. Sci. Part B Polym. Phys.*, vol. 56, no. 17, pp. 1193–1202, 2018.
- [8] Z. Liu, G. Zhang, and D. Zhang, “Modification of side chains of conjugated molecules and polymers for charge mobility enhancement and sensing functionality,” *Acc. Chem. Res.*, vol. 51, no. 6, pp. 1422–1432, 2018.
- [9] Z. Wang *et al.*, “Charge mobility enhancement for conjugated DPP-selenophene

- polymer by simply replacing one bulky branching alkyl chain with linear one at each DPP unit,” *Chem. Mater.*, vol. 30, no. 9, pp. 3090–3100, 2018.
- [10] J. Tian *et al.*, “Optically tunable field effect transistors with conjugated polymer entailing azobenzene groups in the side chains,” *Adv. Funct. Mater.*, vol. 29, no. 12, p. 1807176, 2019.
- [11] Y.-P. Zhang *et al.*, “Distinguishing diketopyrrolopyrrole isomers in single-molecule junctions via reversible stimuli-responsive quantum interference,” *J. Am. Chem. Soc.*, vol. 140, no. 21, pp. 6531–6535, 2018.
- [12] Y. Zang *et al.*, “Resonant transport in single diketopyrrolopyrrole junctions,” *J. Am. Chem. Soc.*, vol. 140, no. 41, pp. 13167–13170, 2018.
- [13] Y. Zang *et al.*, “Voltage-induced single-molecule junction planarization,” *Nano Lett.*, vol. 21, no. 1, pp. 673–679, 2020.
- [14] Z. Tan *et al.*, “The Control of Intramolecular Through-Bond and Through-Space Coupling in Single-Molecule Junctions,” *CCS Chem.*, vol. 3, pp. 929–937, 2021.
- [15] X. Guo, D. Xiang, and Y. Li, *Molecular-scale Electronics: Concept, Fabrication and Applications*. John Wiley & Sons, 2020.
- [16] Z. Cai, N. Zhang, M. A. Awais, A. S. Filatov, and L. Yu, “Synthesis of Alternating Donor–Acceptor Ladder-Type Molecules and Investigation of Their Multiple Charge-Transfer Pathways,” *Angew. Chemie*, vol. 130, no. 22, pp. 6552–6558, 2018.
- [17] L. Venkataraman, J. E. Klare, C. Nuckolls, M. S. Hybertsen, and M. L. Steigerwald, “Dependence of single-molecule junction conductance on molecular conformation,” *Nature*, vol. 442, no. 7105, pp. 904–907, 2006.

- [18] A. Mishchenko *et al.*, “Single-molecule junctions based on nitrile-terminated biphenyls: a promising new anchoring group,” *J. Am. Chem. Soc.*, vol. 133, no. 2, pp. 184–187, 2011.
- [19] C. M. Finch, S. Sirichantaropass, S. W. Bailey, I. M. Grace, V. M. García-Suárez, and C. J. Lambert, “Conformation dependence of molecular conductance: Chemistry versus geometry,” *J. Phys. Condens. Matter*, vol. 20, no. 2, 2008.
- [20] S. Soni *et al.*, “Understanding the Role of Parallel Pathways via In-Situ Switching of Quantum Interference in Molecular Tunneling Junctions,” *Angew. Chemie Int. Ed.*, vol. 59, no. 34, pp. 14308–14312, 2020.
- [21] M. Carlotti, A. Kovalchuk, T. Wächter, X. Qiu, M. Zharnikov, and R. C. Chiechi, “Conformation-driven quantum interference effects mediated by through-space conjugation in self-assembled monolayers,” *Nat. Commun.*, vol. 7, no. 1, pp. 1–7, 2016.
- [22] D. Kos *et al.*, “Optical probes of molecules as nano-mechanical switches,” *Nat. Commun.*, vol. 11, no. 1, pp. 1–8, 2020.
- [23] Y. Zang *et al.*, “Cumulene wires display increasing conductance with increasing length,” *Nano Lett.*, vol. 20, no. 11, pp. 8415–8419, 2020.
- [24] S. Martín *et al.*, “Identifying diversity in nanoscale electrical break junctions,” *J. Am. Chem. Soc.*, vol. 132, no. 26, pp. 9157–9164, 2010.
- [25] R. Frisenda, V. A. E. C. Janssen, F. C. Grozema, H. S. J. Van Der Zant, and N. Renaud, “Mechanically controlled quantum interference in individual π -stacked dimers,” *Nat. Chem.*, vol. 8, no. 12, pp. 1099–1104, 2016.
- [26] C. Tang *et al.*, “Multicenter-Bond-Based Quantum Interference in Charge Transport

- Through Single-Molecule Carborane Junctions,” *Angew. Chemie*, vol. 131, no. 31, pp. 10711–10715, 2019.
- [27] Q. Liu, S. E. Bottle, and P. Sonar, “Developments of Diketopyrrolopyrrole-Dye-Based Organic Semiconductors for a Wide Range of Applications in Electronics,” *Adv. Mater.*, vol. 32, no. 4, p. 1903882, 2020.
- [28] M. Grzybowski and D. T. Gryko, “Diketopyrrolopyrroles: synthesis, reactivity, and optical properties,” *Adv. Opt. Mater.*, vol. 3, no. 3, pp. 280–320, 2015.
- [29] Z. Yi, S. Wang, and Y. Liu, “Design of High-Mobility Diketopyrrolopyrrole-Based π -Conjugated Copolymers for Organic Thin-Film Transistors,” *Adv. Mater.*, vol. 27, no. 24, pp. 3589–3606, 2015.
- [30] J. M. Soler *et al.*, “The SIESTA method for ab initio order-N materials simulation,” *J. Phys. Condens. Matter*, vol. 14, no. 11, pp. 2745–2779, 2002.
- [31] J. P. Perdew, K. Burke, and M. Ernzerhof, “Physical Review Letters,” *Physical Review Letters*. 1998.
- [32] Z. Tang *et al.*, “Solvent-molecule interaction induced gating of charge transport through single-molecule junctions,” *Sci. Bull.*, vol. 65, no. 11, pp. 944–950, 2020.
- [33] J. Ferrer, C. J. Lambert, V. M. Garcia-Suárez, D. Z. Manrique, D. Visontai, and L. Oroszlany, “R. Rodriguez-Ferradá s, I. Grace, S. Bailey, and K. Gillemot,” *New J. Phys.*, vol. 16, p. 93029, 2014.
- [34] Q. Wu, S. Hou, H. Sadeghi, and C. Lambert, “A single-molecule porphyrin-based switch for graphene nano-gaps,” *Nanoscale*, vol. 10, pp. 6524–6530, 2018.
- [35] M. A. Naik, N. Venkatramiah, C. Kanimozhi, and S. Patil, “Influence of side-chain on

- structural order and photophysical properties in thiophene based diketopyrrolopyrroles: A systematic study,” *J. Phys. Chem. C*, vol. 116, no. 50, pp. 26128–26137, 2012.
- [36] C. Fu, F. Bélanger-Gariépy, and D. F. Perepichka, “Supramolecular ordering of difuryldiketopyrrolopyrrole: The effect of alkyl chains and inter-ring twisting,” *CrystEngComm*, vol. 18, no. 23, pp. 4285–4289, 2016.
- [37] Y. Qiao *et al.*, “Diketopyrrolopyrrole-containing quinoidal small molecules for high-performance, air-stable, and solution-processable n-channel organic field-effect transistors,” *J. Am. Chem. Soc.*, vol. 134, no. 9, pp. 4084–4087, 2012.
- [38] D. Vonlanthen, A. Mishchenko, M. Elbing, M. Neuburger, T. Wandlowski, and M. Mayor, “Chemically controlled conductivity: torsion-angle dependence in a single-molecule biphenyldithiol junction,” *Angew. Chemie Int. Ed.*, vol. 48, no. 47, pp. 8886–8890, 2009.

6. Conclusions and Future works

6.1. Conclusions

The electric properties of different molecular devices have been studied in this thesis using density functional theory and the Green's function scattering formalism as well as a simple tight binding methods (TBMs), which are presented in chapter 2 and 3 respectively.

In chapter 4, I demonstrated that manipulating the connectivity of external electrodes to central rings of carbon-based molecules in single molecule junctions is an effective route to tune their electrical and thermoelectrical properties based on a series of thiophenediketopyrrolopyrrole (DPP) derivative molecules. I found that for connectivities corresponding to constructive quantum interference (CQI), different isomers obtained by rotating the thiophene rings possess the same electrical conductance, while those corresponding to destructive quantum interference (DQI) show huge conductance variations upon ring rotations. Furthermore, this DQI connectivity leads to enhanced Seebeck coefficients, which can reach 500–700 $\mu\text{V/K}$. For the CQI, it is found that after including the contribution to the thermal conductance from phonons, the full figure of merit (ZT) could reach 1.5 at room temperature. In additions, as the thiophene rings are widely used in molecular electronics, I presented the electrical conductance tuning of thiophene monomer and thiophene dimer attached to gold electrodes to further understand the DPP series, and showed some theoretical analysis methods adopted in this project such as magic number theory and tight-binding method.

In the chapter 5, I focused on the side-chain effects on intramolecular charge transport in π -conjugated DPP-molecule. The possibility of tuning the electrical conductance within branching alkyl chains, it was investigated by placing with different branching alkyl chains called **DPP-1/4**, **DPP-2/6**, and **DPP-8/12**. I showed that as the alkyl chain becomes longer the

electrical conductance decreased due to the torsional angles between the aromatic rings increased. Furthermore, the relationship between the transmission function around middle point of HOMO-LUMO gap and the torsion angle θ was calculated, which follows approximately $T(E, \theta) \propto \cos^6 \theta$ which is not the expected $\cos^8 \theta$ due to several other effects present in the system, e.g. the electrostatic effects between S of thiophene, O of DPP core and H of phenyl ring.

6.2. Future works

In this thesis, I investigated the electrical conductance of different kinds of molecules attached to gold electrodes. For future studies, there are some aspects deserve further attention, including the connectivity dependence of quantum transport through Diphenyl-DPP molecule with different aromatic rings [1]. In particular, I would be interest to examine how results change when SMe is replaced by other anchor groups such as amino (NH₂), direct carbon-gold (C), and thiol (S)[2][3] bonds to electrodes.

The electron-transport characteristics of single-molecular junctions can be strongly influenced by intermolecular gating due to the presence of neighbouring molecules and the corresponding packing density. In recent years, progress in self-assembly techniques has made it possible to design molecular devices. To develop advanced molecular thermoelectric device, it is of great importance to explore heat transport by intermolecular gating on the self-assembled monolayer (SAM). To develop advanced organic molecular thermoelectric devices, intermolecular gating is one of the major factors to affect the charge transport between adjacent molecules. It worth to investigate how Seebeck coefficient of single-molecule junction could be covered by a self-assembled monolayers (SAMs) of diketopyrrolopyrrole (DPP) derivatives and study the

influence of interactions with neighbouring molecules, which depend on the packing density of the SAMs. It would also be interesting to examine the effect of more heterocycle thiophene rings in the molecular core. In practice, different alkyl chains could also be introduced to investigate their effect.

One aspect would be of interest to study the non-classical behaviour of cycloparaphenylene (CPP), which consists of several 6-membered phenyl rings linked by covalent bonds, it is denoted CPP_n, n is the number of phenyl rings. Currently, the calculation of the electrical conductance of CPP₆ is ongoing and should deliver a complete theory based on DFT, TBM and the magic-number theory. For future calculations, it is worth investigating several macrocycles with increasing the number of phenyl rings (CPP_n) and making them more practical by introducing an anchor group.

Looking forward, the field of molecular electronics still leaves important questions unanswered. One such question is how chemical modifications of molecules and electrodes can lead to huge changes in their electrical properties. Additionally, it would be useful to study the effect of alternative electrode materials for molecular electronics, such as graphene[4], silicene[5][6], platinum, palladium[7], or even superconducting electrodes[8][9], which introduce their own novel interference effects. These would be of great value for future research and the development of exotic and unprecedented molecular-scale devices. For example, Graphene provides remarkable properties and numerous potential applications Such as sensing application[10]. It avoids the complexity of metal molecule interfaces, and has a wide electrochemical potential window, low electrical resistance, and well-defined redox peaks, which can lead to increased sensitivity[11]. Furthermore, the high thermal conductivity of graphene makes this material very attractive to manage heat and dissipate it in high density devices. Other recent topics of interest in nanoelectronics include the study of hybrid systems

containing superconducting (S) and ferromagnetic (F) materials of their relevance for spintronics applications. Spintronic devices incorporate spin-polarized currents and magnetic fields, both of which act to inhibit superconducting transport[9].

Bibliography

- [1] C. J. Lambert, *Quantum Transport in Nanostructures and Molecules*. IOP Publishing, 2021.
- [2] F. Chen, X. Li, J. Hihath, Z. Huang, and N. Tao, “Effect of anchoring groups on single-molecule conductance: Comparative study of thiol-, amine-, and carboxylic-acid-terminated molecules,” *J. Am. Chem. Soc.*, vol. 128, no. 49, pp. 15874–15881, 2006.
- [3] R. Frisenda *et al.*, “Electrical properties and mechanical stability of anchoring groups for single-molecule electronics,” *Beilstein J. Nanotechnol.*, vol. 6, no. 1, pp. 1558–1567, 2015.
- [4] S. Bailey, D. Visontai, C. J. Lambert, M. R. Bryce, H. Frampton, and D. Chappell, “A study of planar anchor groups for graphene-based single-molecule electronics,” *J. Chem. Phys.*, vol. 140, no. 5, 2014.
- [5] J. P. Small, K. M. Perez, and P. Kim, “Modulation of thermoelectric power of individual carbon nanotubes,” *Phys. Rev. Lett.*, vol. 91, no. 25, pp. 256801, 2003.
- [6] Q. Wu, H. Sadeghi, V. M. García-Suárez, J. Ferrer, and C. J. Lambert, “Thermoelectricity in vertical graphene-C60-graphene architectures,” *Sci. Rep.*, vol. 7, pp. 11680, 2017.
- [7] V. M. García-Suárez, A. R. Rocha, S. W. Bailey, C. J. Lambert, S. Sanvito, and J. Ferrer, “Single-channel conductance of H₂ molecules attached to platinum or palladium electrodes,” *Phys. Rev. B*, vol. 72, no. 4, pp. 45437, 2005.
- [8] C. J. Lambert, R. Raimondi, V. Sweeney, A. F. Volkov, “Boundary conditions for

- quasiclassical equations in the theory of superconductivity,” *Phys. Rev. B* 55 (9), 6015, 1997.
- [9] M. Eschrig, A. Cottet, W. Belzig, and J. Linder, “General boundary conditions for quasiclassical theory of superconductivity in the diffusive limit: Application to strongly spin-polarized systems,” *New J. Phys.*, vol. 17, no. 8, 2015.
- [10] M. Pykal, P. Jurečka, F. Karlický, and M. Otyepka, “Modelling of graphene functionalization,” *Phys. Chem. Chem. Phys.*, vol. 18, no. 9, pp. 6351–6372, 2016.
- [11] M. S. Artiles, C. S. Rout, and T. S. Fisher, “Graphene-based hybrid materials and devices for biosensing,” *Advanced Drug Delivery Reviews.*, vol. 63, no. 14-15, pp. 1352-1360, 2011.